STUDIES INTO THE INITIAL CONDITIONS, FLOW RATE, AND CONTAINMENT SYSTEM OF OIL FIELD LEAKS IN DEEP WATER

A Thesis

by

RACHEL LEE HOLDER

Submitted to the Office of Graduate Studies of
Texas A&M University
in partial fulfillment of the requirements for the degree of

MASTER OF SCIENCE

Chair of Committee,	Scott Socolofsky
Committee Members,	Alejandro Orsi
	Richard Mercier
Head of Department,	Robin Authenrieth

August 2013

Major Subject: Ocean Engineering

ABSTRACT

Oil well blow outs are investigated to determine methods to quickly and accurately respond to an emergency situation. Flow rate is needed to guide containment and dispersal operations. The Stratified Integral Multiphase Plume, SIMP, model was used to investigate the range of initial conditions available to integral modeling. Sensitivity to initial conditions is modest, but without experimental data at the appropriate scale the most accurate condition is unable to be determined. Flow rates are difficult to directly measure in blow out situations, so another method must be determined; therefore, sensitivity of several parameters to flow rate was also evaluated. Methane concentration in the first intrusion can be used in conjunction with velocity and trap height measurements to determine flow rate using an integral model. Plume width and temperature were determined to have little sensitivity. Separately, a containment dome was tested in the laboratory to determine if a full scale dome can be used to contain an oil leak in the field. The dome was found to have satisfactory entrapment in the designed position.

ACKNOWLEDGMENTS

I would like to thank Shell for funding this research, for building the experimental model, and being available for questions.

TABLE OF CONTENTS

Page

LIST OF FIGURES

Page

Page

Page

Page

LIST OF TABLES

Page

1. INTRODUCTION

Oil well blowouts are accidents resulting in uncontrolled flow in an oil recovery well. When multiple layers of redundancy fail, these accidents may result in uncontrolled discharge of oil and gas to the water column, as occurred in 2010 from the Deepwater Horizon MC252 disaster. The key to recovering from these accidents is a thorough understanding of the physics that occur in multiphase oil and gas plumes. Several recovery techniques are used in blowout situations including, but not limited to, chemical dispersants, burning of surface oil, and containment domes (EPA, 1999). Containment domes are beneficial in that the oil is contained near the source. However, containment domes require knowledge of the flow rate from the system to be properly implemented. Flow rate remains difficult to determine during these emergencies due to the difficulty of directly measuring the flow rate with an ROV or other submersible instrument. This thesis comprises of methods to estimate the flow rate of oil, gas, and water into a containment dome system using simple measurements combined with integral modeling and tests the range of operating conditions in which a particular dome can operate in the laboratory.

Integral modeling is used to determine characteristics of multi-phase plumes using a self-similarity assumption, the assumption that profiles retain the same shape at every level in the plume. To generate an integral model, initial conditions must be found such

that the model can begin calculations, and the self-similarity assumption is used to continue the calculations through the entire length of the plume. Basic initial conditions include the initial velocity profiles and magnitudes, plume width, and plume constituents as shown in Figure 1.1.

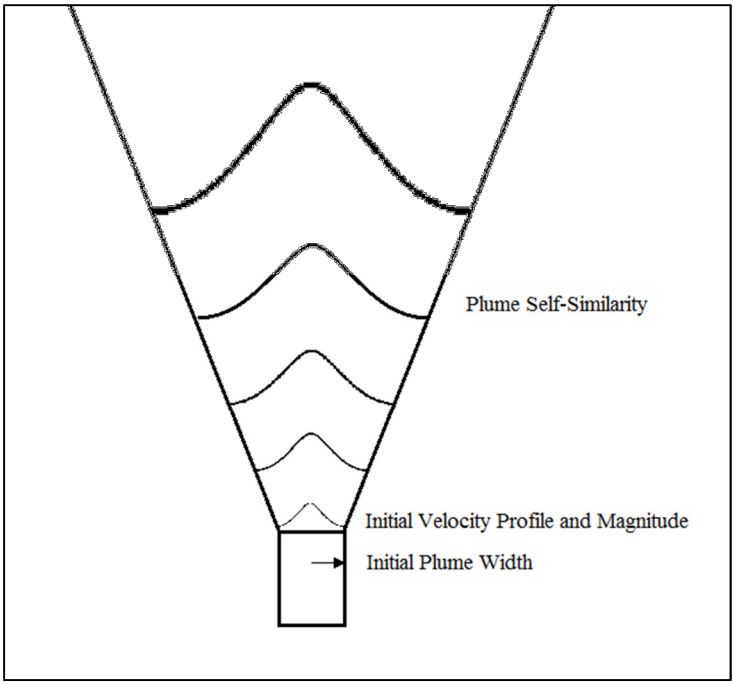

Figure 1.1: Visual description of initial conditions and self-similarity.

One of the most difficult areas of plume dynamics is the zone of flow establishment (ZFE) due to the invalid assumptions of self-similarity in integral plume models in this area. The ZFE is the region of flow in which the velocity develops from a top-hat distribution to a Gaussian distribution inside the plume. Containment domes operate in the ZFE and are therefore difficult to operate with the current methods of determining flow rate in the zone of operation. Several initial conditions have been proposed, e.g.

(Morton, Taylor, & Turner, 1956), (Wüest, Brooks, & Imboden, 1992), and (Asaeda & Imberger, 1993), to determine the plume characteristics after the ZFE, and it is beneficial to see the relationship between these initial conditions and the behavior of the integral model following each choice.

This research also addresses limitations in field-scale measurements; flow rate is a difficult parameter to directly measure. The general flow rate of a field-scale accident may be determined by measuring certain parameters in the plume itself using an ROV and constraining integral models to reproduce the measurements. This allows integral models to determine flow rate without measuring it directly. Several parameters are investigated in this report, namely, plume temperature, width, point velocity in the inner plume, trap height, as well as methane concentration in the outer plume. All of these parameters can be measured using an ROV in an emergency situation and may aid to quickly and accurately determining the likely flow rate of oil and gas at the source.

This report also examines the operating conditions of a particular containment dome designed by Shell. The containment dome is a scaled model and was tested in the Texas A&M University hydromechanics laboratory.

This research is an important step in the containment of accidental blow out situations. It will allow for quicker and more accurate modeling of the situation, which will provide for faster response times and more successful endeavors to contain the situation.

2. LITERATURE REVIEW

2.1. Introduction to Plumes and Non-Dimensional Parameterizations

McDougall developed one of the first integral models for buoyant plumes in stratified environments. This model included the use of double plumes which entailed the separation of the inner bubble plume and a second annular plume of entrained water which contained no bubbles, as shown in Figure 2.1 (McDougall, 1977). The model assumes a Gaussian velocity distribution.

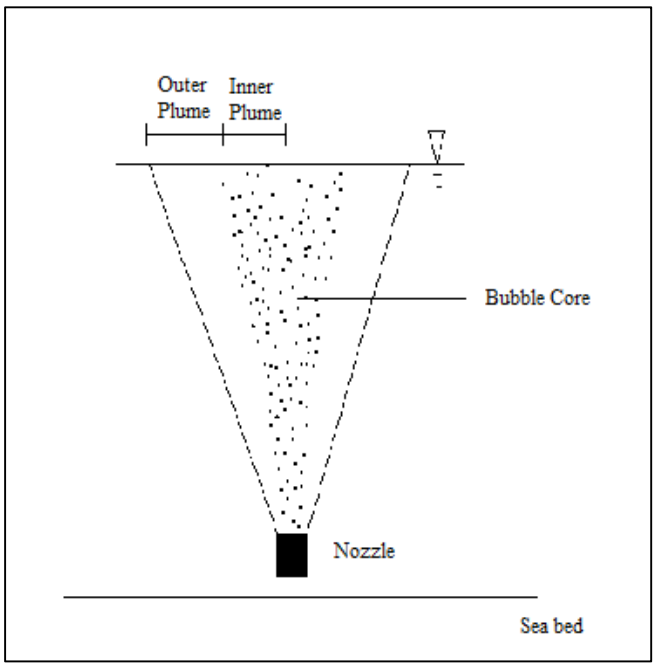

Figure 2.1: Position of the inner and outer plume for McDougall's double plume model.

Asaeda and Imberger altered this model, defining double plumes as the combination of the rising inner plume and the falling outer plume including intrusions, shown in Figure 2.2 (Asaeda & Imberger, 1993). This differed from the McDougall model by including all upward-flowing water and bubbles in the inner plume.

They observed three types of plumes based on laboratory experiments shown in Figure 2.3. Type 1 is a plume that intrudes upon the surface, Type 2 is a plume that intrudes in distinct layers below the surface, and Type 3 is a plume that continuously intrudes. Type 1* is defined as a plume in which the slip velocity is relatively low and some of the smaller bubbles will intrude (Socolofsky & Adams, "Role of Slip Velocity in the Behavior of Stratified Multiphase Plumes", 2005). Asaeda and Imberger also developed two non-dimensional parameters to describe plume types 1, 2, and 3:

$$P_N = \frac{N^3 H^4}{Q_0 g} \tag{1.1}$$

$$M_H = \frac{Q_0 g}{4\pi\alpha^3 H u_s^3} \tag{1.2}$$

where P_N is the non-dimensional plume number, u_s is the slip velocity, z is the distance above the source, and N is the buoyancy frequency defined as

$$N^2 = -\frac{g}{\rho_r}\frac{\partial \rho_a}{\partial z}, \tag{1.3}$$

g is the acceleration of gravity, ρ_a is the ambient density, α is the entrainment coefficient, H is the water depth, Q_0 is the bottom volume flux of gas, and M_H is the velocity ratio of plume fluid and dispersant bubbles. The non-dimensional plume number represents the

ratio of water depth to trap height, and the velocity ratio represents the ratio of the velocities of the water in the plume to the bubbles in the plume. These non-dimensional numbers were shown to reliably predict the plume type in a given situation (Asaeda & Imberger, 1993).

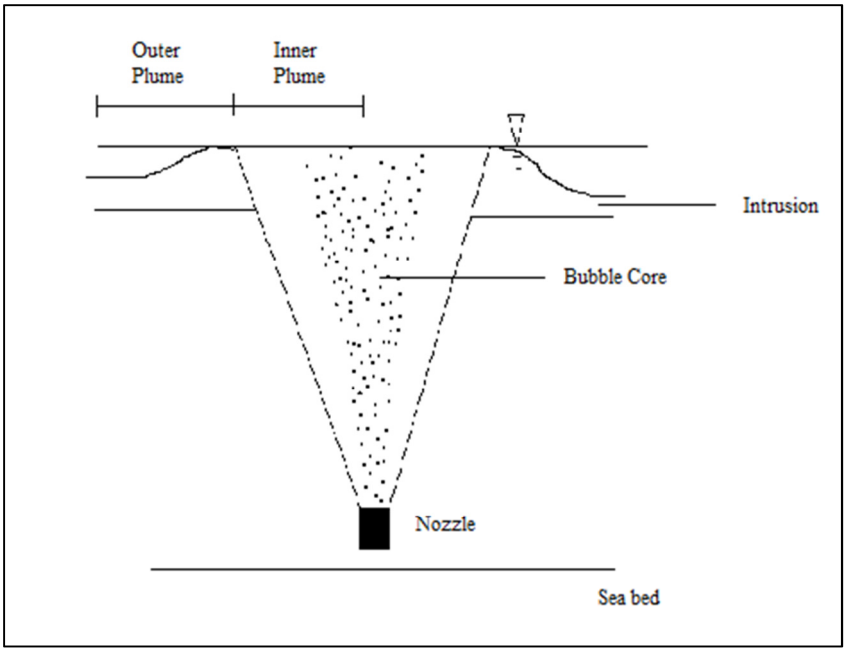

Figure 2.2: Positioning of Asaeda and Imberger's definition of double plume.

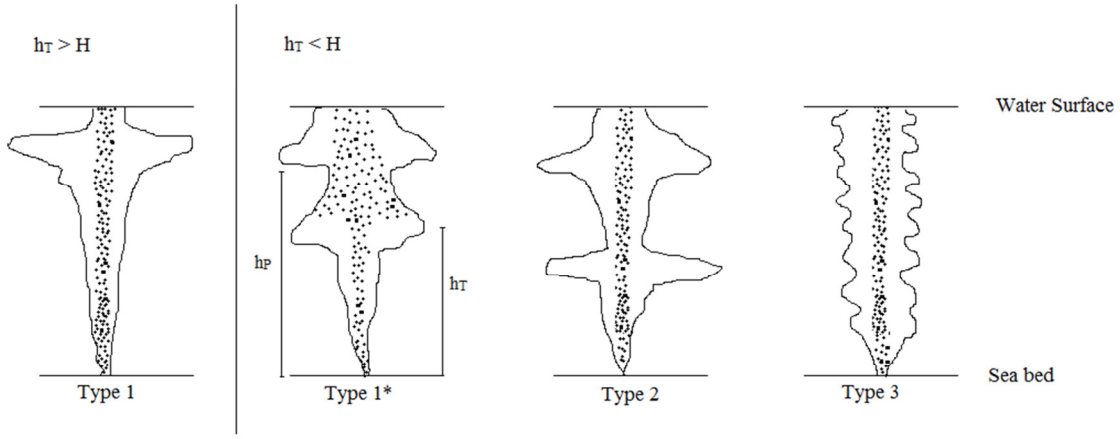

Figure 2.3: Definition of plume types where H is water depth (Socolofsky & Adams, "Role of Slip Velocity in the Behavior of Stratified Multiphase Plumes", 2005).

The Asaeda and Imberger paper shows the characteristic velocity scale as the single-phase plume rise velocity in stratified fluid and derived it as

$$u_c = (BN)^{1/4} \tag{1.4}$$

where B is the kinematic buoyancy flux given by

$$B = gQ_0 \frac{\rho_a - \rho_b}{\rho_r} \tag{1.5}$$

such that ρ_b is the density of the dispersed phase, and Q_0 is the volume flux at the bottom (Asaeda & Imberger, 1993). Socolofsky and Adams developed a new non-dimensional coefficient, the non-dimensional slip velocity, U_N , to predict plume types 1^*, 2, and 3 described in Figure 2.3 (Socolofsky & Adams, "Role of Slip Velocity in the Behavior of Stratified Multiphase Plumes", 2005). U_N is the ratio of the slip velocity and the characteristic fluid velocity, shown in equation (1.4), and is given by

$$U_N = \frac{u_s}{(BN)^{1/4}} \tag{1.6}$$

This parameter allows for a more simplistic determination of plume type than the combination of two terms used by Asaeda and Imberger. This parameter is also independent of water depth; hence, it can be used in deep water more confidently than those derived by Asaeda and Imberger. The characteristic height can be used for comparisons in trap height and is defined as

$$l_c = \left(\frac{B}{N^3} \right)^{1/4} . \tag{1.7}$$

Figure 2.3 also includes h_T, trap height, given as the height at which the peeling fluid becomes trapped in the stratification and intrudes, and h_P, peeling height, defined as the height at which the first peeling event occurs.

2.2. Initial Conditions

This section is intended as a brief overview of the various initial conditions used in this research. Initial condition equations try to predict behavior to match plume properties at the top of the ZFE. A more in depth discussion will occur in Section 0.

The zone of flow establishment is also a source of research to increase accuracy of currently used models. Henderson-Sellers determined an estimate for the length of the zone of flow establishment for buoyant plumes

$$z_e = \begin{cases} 4d & F_d^2 < 8 \\ 3.27 + 0.26\sqrt{F_d^2})d & 8 \le F_d^2 \le 128 \\ 6.2d & F_d^2 > 128 \end{cases} \tag{1.8}$$

where d is the source diameter and

$$F_D^2 = \frac{u^2}{b\Delta} \tag{1.9}$$

where u is the centerline velocity, b is the radius of the plume, and

$$\Delta = g\frac{(T_p - T_a)}{T_a} \tag{1.10}$$

where T_p is the plume temperature and T_a is the ambient temperature (Henderson-Sellers, 1983). These temperatures may be converted to densities using the saltwater equation of state, and the densities and void ratios of the plume components. These equations are linear fits to the numerical data obtained by Chen and Nikitopoulos (Chen & Nikitopoulos, 1979) who developed a numerical model to investigate plume behavior that is accurate in the zone of flow establishment for a single phase plume. These non-dimensional parameters will be used to validate portions of the analysis performed in this study.

Since the ZFE is not self-similar, initial conditions are developed so the model returns accurate results above the ZFE. McDougall developed a set of initial conditions that begin at a virtual point source below the actual source of the plume. The initial conditions for non-dimensional velocity and plume width are a function of the following:

$$M = \frac{Q_S p_a(\lambda^2 + 1)}{4\pi\alpha^2 \rho_r H^2 u_B^2} \tag{1.11}$$

$$x = \frac{z}{H} \tag{1.12}$$

where M is the relative importance of the volume flux of gas at the source and the total water depth in the non-dimensional solutions, Q_S is the volume flux at the surface, p_a is the pressure at the surface, λ is the ratio of plume width to density deficiency, α is the entrainment coefficient, ρ_r is the reference density, H is the static pressure head at the nozzle, $u_B = u_s(\lambda^2+1)$, u_s is the slip velocity, x is the non-dimensional height above the plume source, and z is the dimensional height above the plume source. It should be noted that M is a function of the volume flux at the surface, which is not a trivial solution in a plume that intrudes, and that x is a function of the water depth, which is not an appropriate non-dimensionalization when $H \rightarrow \infty$ in deep water.

Asaeda and Imberger altered McDougall's initial conditions to include the bottom volume flux instead of the volume flux at the surface as shown in equations (1.2) and (1.11); this eliminates any ambiguity existing due to intrusions. However these initial conditions still include non-dimensionalization using water depth.

Wüest, Brooks, and Imboden also developed a set of initial conditions that can be used at the source of the plume (Wüest, Brooks, & Imboden, 1992). The initial radius is taken as the radius of the source. Wüest defines a dimensionless Froude number to determine the initial velocity,

$$Fr = \frac{u_0}{\left[2\lambda bg(\rho_a - \rho)/\rho\right]^{1/2}} \tag{1.13}$$

where u_0 is the initial vertical velocity, λb is the initial plume radius, ρ_a is the ambient density, and ρ is the plume density, which includes both entrained water and the dispersed phase. Wüest explains how the dimensionless Froude number at the source varies around several factors, but as depth increases the initial Froude number tends to a nearly constant value of 1.6. Wüest goes on to show sensitivity analyses on the initial Froude number values to show that 1.6 is a reasonable assumption for most plumes. The initial vertical velocity can be determined by solving the dimensionless Froude number equation.

Morton, Taylor, and Turner developed a set of initial conditions that begin at a virtual point below the source of a single-phase plume (Morton, Taylor, & Turner, 1956). Originally this initial condition was used for smoke stacks, but it can be adapted to deep water, single-phase plumes. Like Asaeda and Imberger, this initial condition is a series expansion containing a variable that represents the distance from the virtual point source to the actual source in the case of a non-point source scenario.

Neto developed a set of initial conditions for plumes that contain momentum at the source exit (Neto, 2012). This is the only set of initial conditions studied that does not assume momentum at the source has a value of zero. These initial conditions use only the volume flow rates of liquid and gas at the source exit, and the diameter of the source to find the initial velocity. The initial plume width is taken as the diameter of the source. This initial condition is valid at the orifice and does not require a virtual point source.

Also, in beginning the model, initial values must be studied to determine the accuracy needed for initial values to produce reliable results. Bombardelli, et.al. studied the effects of changing initial values input into unstratified bubble plume models (Bombardelli, Buscaglia, Rehmann, Rincon, & Garcia, 2007). It is found that the results converge regardless of the initial diameter and Froude number at a height of $z/D = 5$ where z is the height above the plume and D is defined as

$$D = \frac{gQ_0}{4\pi\alpha^2 u_s^3} \tag{1.14}$$

where Q_0 is the flow rate at the bottom, and u_s is the slip velocity.

This research will use the initial conditions developed by the authors described above to determine model sensitivity to initial condition selection.

2.3. Building Blocks of the SIMP Model

This section will describe the basis of the integral model used in this research. Many of the pieces of this model were taken from various theories and combined to create a more robust model. The model used includes the ability to add stratification, constituents in the bubble plume including multiple gasses, gas expansion, dissolution, and multiple bubble sizes therefore increasing the accuracy of integral modeling.

Wüest developed the discrete bubble model for use in the integral model's inner plume (Wüest, Brooks, & Imboden, 1992). The discreet bubble model follows the development

of one bubble through the extent of the plume, and assumes that all bubbles develop similarly.

Crounse, et al. developed an integral model that included the ability to track dispersed phase dissolution for CO_2 in deep water (Crounse, Wannamaker, & Adams, 2007). This allows the ability for the inner plume density to change due to dissolution. This model also allows for a wide range of plume behavior due to the added peeling parameter.

Crounse included many similar equations utilized in the SIMP integral model used in this research (Crounse B. C., 2000). The equations used to take into account the dissolution of CO_2 are altered to determine methane dissolution in the SIMP model (Socolofsky, Bhaumik, & Seol, "Double-Plume Integral Models for Near-Field Mixing in Multiphase Plumes", 2008). Both models track the heat and salinity flux inside the plume to determine a reliable plume density and conservation of mass, momentum, heat, and salinity are used as the steady state governing equations.

Socolofsky, Bhaumik, and Seol developed a consistent set of initial conditions for the subsequent inner and outer plume structures in multiphase plumes allowing the model to run smoothly from one intrusion to the next (Socolofsky, Bhaumik, & Seol, "Double-Plume Integral Models for Near-Field Mixing in Multiphase Plumes", 2008). Current literature was used to calibrate and validate the model. These results were implemented in the SIMP model.

The model used in this research has been verified and used in other research. The current modeling techniques were used in the analysis by (Anderson, et al., 2012). The research was used to determine the likelihood of methane hydrates forming under several test cases. These results were used in conjunction with high pressure experiments conducted by Shell to help interpret results of SIMP simulations. These test cases, similar to those discussed in this paper, were evaluated using the same model used in this research.

The same model was also used in (Socolofsky, Bhaumik, & Seol, "Double-Plume Integral Models for Near-Field Mixing in Multiphase Plumes", 2008). This paper compared several integral models to existing experimental data. This research also determines that most applications of this model can use a constant momentum amplification factor and constant entrainment coefficients, among other parameters.

(Socolofsky & Bhaumik, "Dissolution of Direct Ocean Carbon Sequestration Plumes Using an Integral Model Approach", 2008) use this model to study the unsteady intrusion layers due to large amounts of dissolved carbon dioxide over the plume heights. They determine that in spite of the complexity of the plume itself, it has a steady maximum rise height.

3. SENSITIVITY OF RESULTS TO INITIAL CONDITIONS

3.1. Initial Conditions

A series of initial condition equations were used to determine the sensitivity of results to different approaches to solutions inside the ZFE. Two categories of initial conditions exist: those that find the starting value at a virtual point source below the real source and those that find the starting value at the source itself. Figure 3.1illustrates the difference between the position of the actual source and the virtual point source.

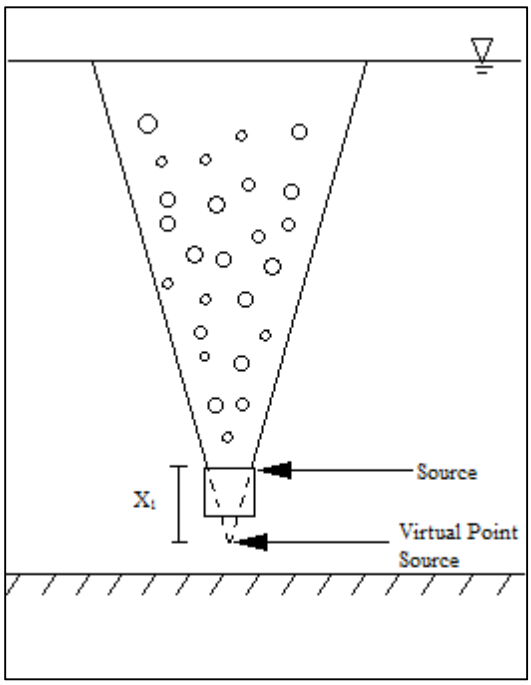

Figure 3.1: Difference between a virtual point source and the actual source.

The purpose of this section is to determine at what height the initial conditions converge for different cases and the sensitivity of model results below the convergence height. The cases investigated are listed in Table 3.1. All cases use the same conditions to allow comparison of results. Three flow rates and three bubble diameters are investigated to determine the effect of both on initial conditions. Cases were determined using typical ranges of flow rates and bubble diameters for depths of 1829 m, 3000 m, and 914.4 m for cases 1, 2, and 3 respectively.

Table 3.1: Cases studied in the initial condition analysis.

Case 1		**Case 2**		**Case 3**	
Flow Rate (BPD)	Bubble Diameter (mm)	Flow Rate (BPD)	Bubble Diameter (mm)	Flow Rate (BPD)	Bubble Diameter (mm)
50,000	2	50,000	2	50,000	2
100,000	2	100,000	2	100,000	2
250,000	0.4	250,000	0.4	250,000	0.4
250,000	2	250,000	2	250,000	2
250,000	4	250,000	4	250,000	4

3.1.1. Wüest et.al.

Wüest developed an initial condition to determine the starting velocity at a plume source. It was assumed that the starting plume radius would be equivalent to the source radius. Matlab's zeroing function (*fzero*) was used to determine the starting velocity, *u*, based on the equation

$$Fr = \frac{u}{\left[2\lambda b g(\rho_a - \rho)/\rho\right]^{1/2}} = 1.6 \qquad (2.1)$$

first described in Section 2.2. The zeroing function is used because of the implicit nature of the equation. Velocity is needed to determine the density of the inner plume.

3.1.2. Asaeda & Imberger

Asaeda and Imberger altered the non-dimensional variables given by McDougall (1977) to incorporate the initial flow rate as opposed to the flow rate at the surface. Equation (1.2) gives the value for M_H used in the Asaeda and Imberger paper; whereas, the following equation defines the corresponding value found in the McDougall paper:

$$M = \frac{Q_0 p_a (\lambda^2 + 1)}{4\pi\alpha^2 \rho_r H^2 u_b^2} \tag{2.2}$$

where Q_x is the volume flux at the surface, λ represents the spreading ratio, and u_b is the bubble velocity. Q_s is related to Q_0 through the following equation:

$$Q_s = \frac{Q_0 p_a}{H \rho_r g} \tag{2.3}$$

where p_a is atmospheric pressure. It can be shown that both M and M_H are proportional to Q_0/H, so both initial conditions can be used interchangeably, varying only by a constant. The variables from Asaeda and Imberger were non-dimensionalized by the following:

$$B = \frac{b}{2\alpha H} \tag{2.4}$$

$$U = \frac{u}{u_s M_H^{1/3}} \tag{2.5}$$

$$x = \frac{z}{H} \tag{2.6}$$

where b is the dimensional plume width and is non-dimensionalized by the entrainment coefficient, α, and the water depth, H; u is the dimensional velocity non-dimensionalized by the slip velocity, u_s, and M_H.; and z is the dimensional height above the diffuser non-dimensionalized by the water depth, H. The non-dimensional initial plume width and velocity were taken from McDougall and are given by

$$B = x[0.6 + 0.01719M_H^{-2/3}x^{1/3} - 0.002527M_H^{-2/3}x^{2/3} + x(-0.04609 + 0.000031M_H^{-1}) + ...] \quad (2.7)$$

$$U = x^{-1/3}[1.609 - 0.3195M_H^{-1/3}x^{1/3} + 0.06693M_H^{-2/3}x^{2/3} + x(0.4536 - 0.0105M_H^{-1}) + ...] \quad (2.8)$$

where M_H is defined in equation (1.2). These equations for plume width and velocity are evaluated at the point where the plume width is equal to the source radius, some $x > 0$, shown in Figure 3.1, and then used as the starting values for the integral model. These initial conditions are proportional to those proposed by McDougall et al.; therefore, these conditions are used to demonstrate the effects of both interchangeably.

3.1.3. Morton, Taylor, & Turner

Morton, Taylor, and Turner developed a set of initial conditions that begin at a virtual point source. The following parameters were non-dimensionalized:

$$x = \frac{z}{2^{-7/8}\pi^{-1/4}\alpha^{-1/2}F_0^{1/4}G^{-3/8}} \quad (2.9)$$

$$v = \frac{V}{2^{3/4}\pi^{-1/2}F_0^{1/2}G^{-1/4}} \quad (2.10)$$

$$w = \frac{W}{2^{7/8}\pi^{-3/4}\alpha^{1/2}F_0^{3/4}G^{-5/8}} \quad (2.11)$$

where z is the dimensional height above the source, V is the plume radius, b, times the velocity, u, and $W = b^2u$, all of which are non-dimensionalized by the entrainment coefficient, α, the buoyancy flux, F_0, and $G = -(g/\rho_{ref})d\rho_a/dx$. The initial conditions are given by the following series:

$$v^4 = 0.1368x^{8/3} - 0.0098x^{16/3} + 0.0001x^{21/3} + ... \tag{2.12}$$

$$w = 0.3649x^{5/3} - 0.0025x^{13/3} + ... \tag{2.13}$$

where the variables are defined above. This solution is evaluated such that the plume width is the same as the source radius, and the solutions are used to begin the integral model.

3.1.4. Neto

Neto developed initial conditions that begin at the source exit (Neto, 2012). Velocity at the source is found using

$$u = \frac{Q_l}{\left(1 - \frac{Q_g}{Q_g + Q_l}\right)\left(\frac{\pi d^2}{4}\right)} \tag{2.14}$$

where Q_l is the liquid volume flow rate at the source, Q_g is the gas volume flow rate at the source, and d is the source diameter. The initial plume width is taken as the diameter of the orifice. This initial condition is the only condition that assumes the flow contains momentum at the source exit. It should be noted that Q_l cannot be zero; thus this equation cannot be used for bubble plumes.

3.2. Results and Discussion

True values are calculated for the sensitivity analysis; true values are the output values calculated during the integral model. Figure 3.2 shows an example case of the true values achieved through the model. The black lines represent the Wüest initial conditions; because these values are more constrained than the other models, these values will be used as the base case for comparison. The subsequent figures in this section are found from similar true value cases.

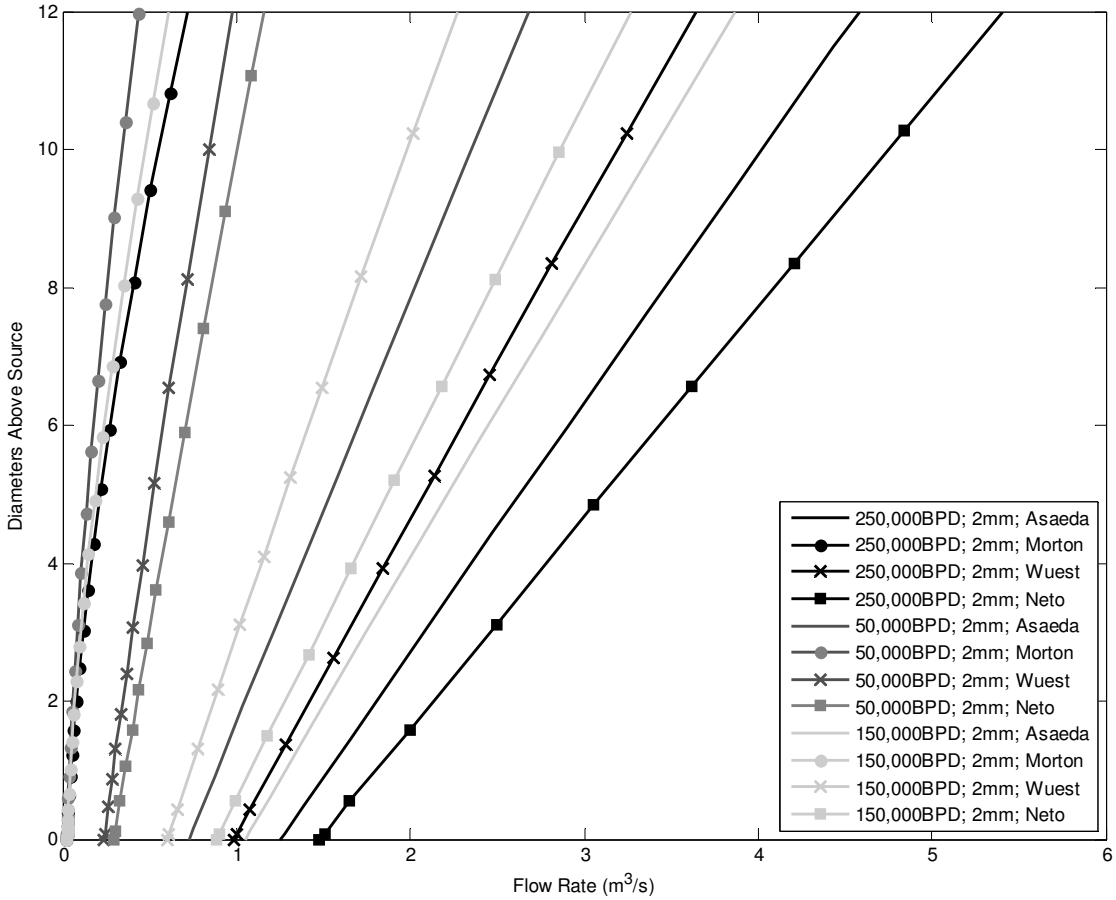

Figure 3.2: True values for flow rate. These values are from Case 1.

Figure 3.3 through Figure 3.5 show the set of four initial conditions up to 12 diameters away from the source. 12 diameters represents the length used to describe the ZFE by many researchers. Changes in bubble diameter were found to have little effect in all cases, so the figures neglect these cases for clarity. Slip velocity has little effect since most of the initial conditions contain u_s internally in one of the variables, or not at all. Figure 3.3 represents Case 1 results, Figure 3.4 represents Case 2 results, and Figure 3.5 represents Case 3 results for initial conditions at 50 kBPD, 150 kBPD, and 250 kBPD. Wüest was used as the base case in the sensitivity analysis for all cases. The sensitivity equation is defined as

$$E = \frac{N_B - N_1}{N_B} \tag{2.15}$$

where E is the sensitivity, N_B is the base case value, and N_1 is the compared value. This value corresponds to the sensitivity of the parameter where a higher value is equivalent to higher sensitivity.

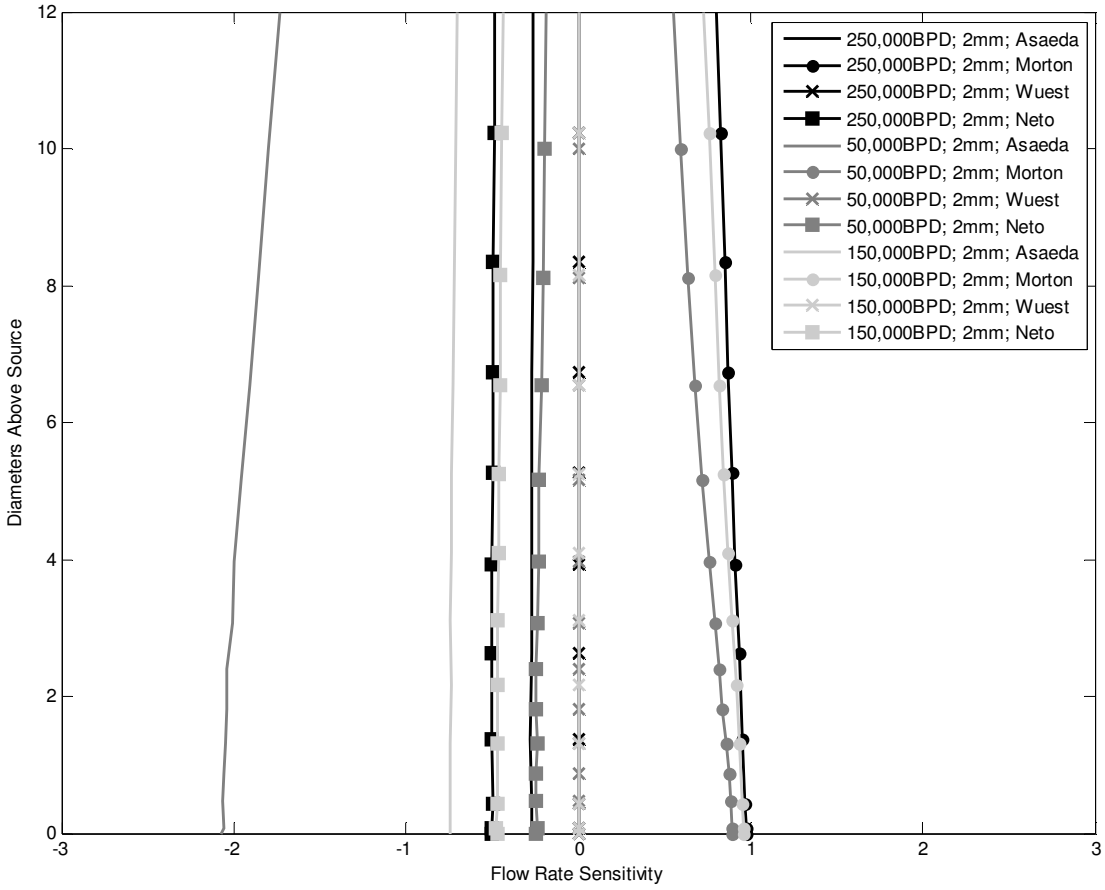

Figure 3.3: Sensitivity of flow rate to different initial conditions 12 diameters away from source. Case 1, a depth of 1829 m, is used for all results in this figure. The values include a range of flow rates from 50 kBPD to 250 kBPD and four initial conditions: (Asaeda & Imberger, 1993), (Morton, Taylor, & Turner, 1956), (Wüest, Brooks, & Imboden, 1992), and (Neto, 2012).

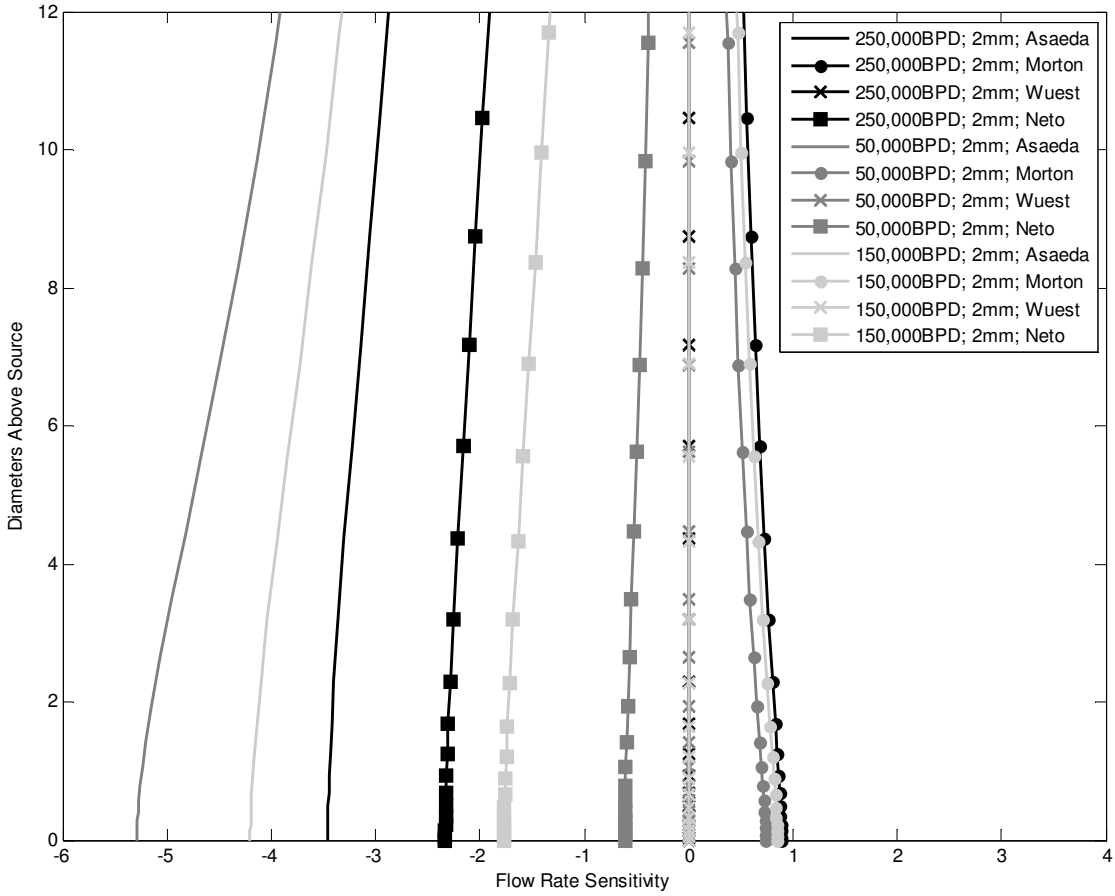

Figure 3.4: Sensitivity of flow rate to different initial conditions 12 diameters away from source. Case 2, a depth of 3000 m, is used for all results in this figure.

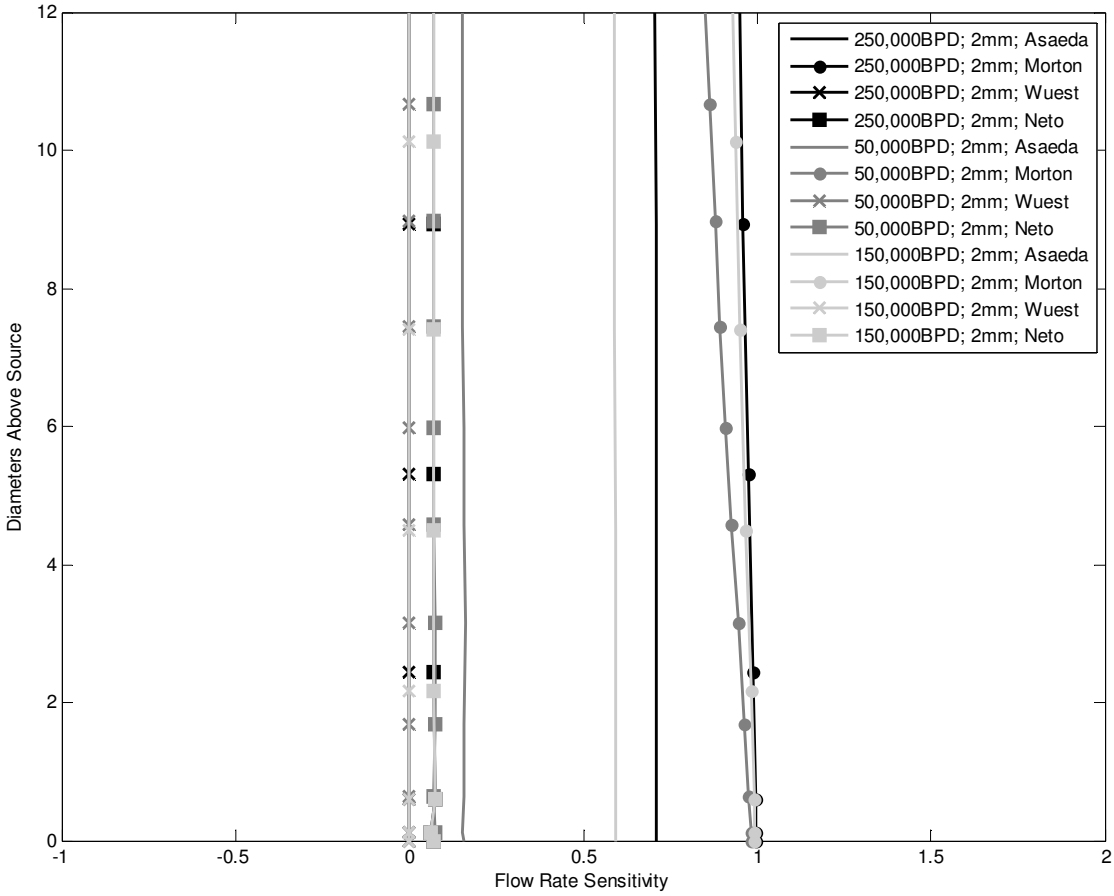

Figure 3.5: Sensitivity of flow rate to different initial conditions 12 diameters away from source. Case 3, a depth of 914 m, is used for all results in this figure.

The Morton initial conditions tend to stay closely grouped and within 100% of the Wüest conditions. Morton is similar to the Wüest conditions in every case in that the flow rate sensitivity remains nearly vertical at 100%; this shows that results determined using the Morton initial condition differ from those calculated from Wüest by a factor of 2 near the source.

The Asaeda initial conditions, when compared to the Wüest base case, vary more with changes in flow rate than Morton conditions, but still remain within 200% of each other. These conditions more closely resemble the Wüest conditions when in shallow water and tend to stray away in deeper water.

The Neto conditions become more similar to the Wüest conditions at shallow water depths. These values tend to have the least sensitivity compared to the Wüest conditions. The Neto initial conditions tend to converge in shallow water; this shows that flow rate becomes less important in shallow water when determining the use of initial conditions. In general the cases tend to converge in shallower water leading to the conclusion that the choice of initial conditions is more important as depth increases. All cases converge and become identical after the first peeling event.

It is impossible to tell which initial condition is more accurate in this study. Future research can be conducted to find true values for inside and close to the ZFE to confirm the initial condition that gives the most accurate results.

4. SENSITIVITY OF PLUME PARAMETERS FOR ESTIMATION OF LEAK FLOW RATE

The purpose of this section is to determine the plausibility of estimating leak flow rate using other measured parameters. A remotely operated vehicle, ROV, has the ability to measure several parameters including temperature, measured through a thermometer; velocity, measured through current meters; concentration, through taken samples; and plume width, using velocity distribution. The results of these measurements will constrain the model to estimate flow rate.

4.1. Model

Several cases were evaluated using the following model to determine the sensitivity of various parameters to changes in flow rate. These results may aid to a method of fast evaluation of the flow rate in time sensitive situations such as oil well blow-outs in the Gulf of Mexico. The test cases were developed based on Mustang's figures of drilling barrels per day (BPD) and depth in the Gulf of Mexico shown in Figure 4.1 (Mustang Engineering, 2012). These flow rates represent all wells developed by each platform. The case depths are shown on the x-axis; the enclosing lines were used to find a range of production volume reasonable for each water depth. Case 2 is outside the range of data acquired, therefore will use the same production volumes as Case 1. The cases evaluated are described in Table 4.1.

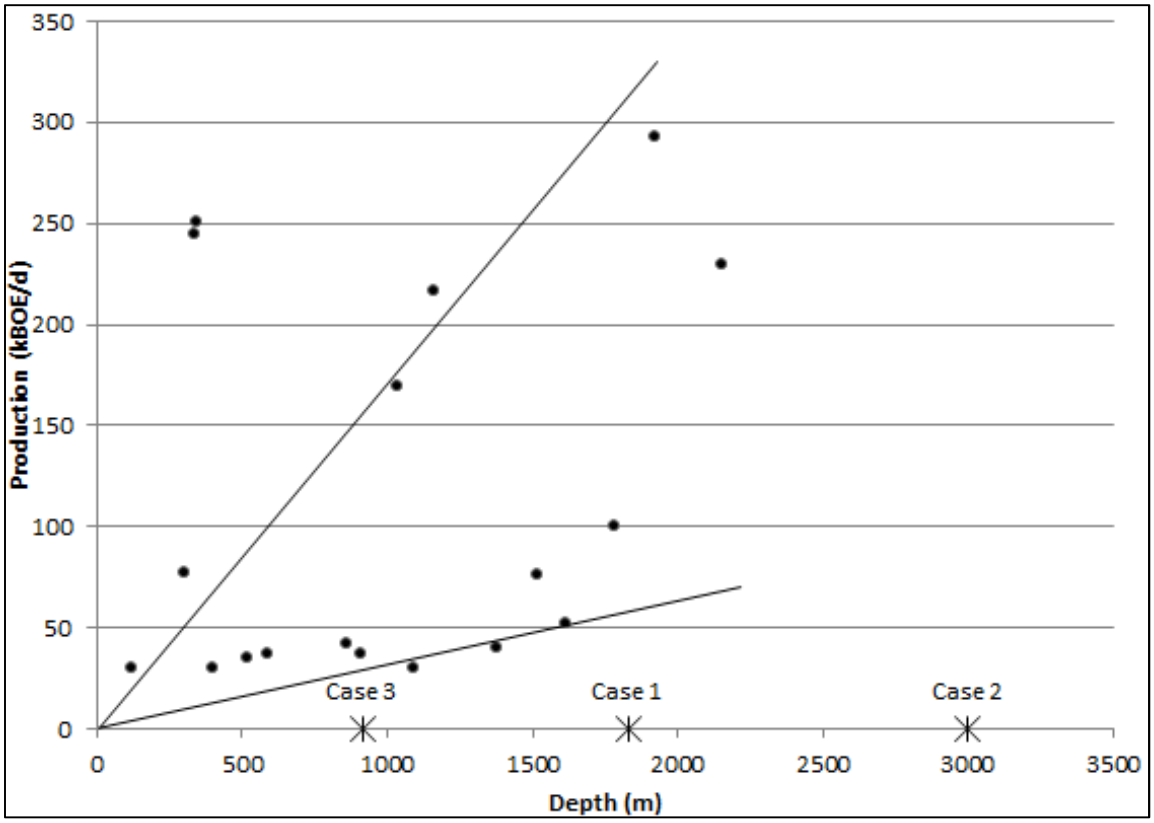

Figure 4.1: Current platform depth and production in the Gulf of Mexico.

Table 4.1: Description of cases run for sensitivity to flow rate.

Water Depth (m):	Run 1 (BPD oil)	Run 2 (BPD oil)	Run 3 (BPD oil)	Run 4 (BPD oil)	Run 5 (BPD oil)
Case 1: 1829	50,000	100,000	150,000	200,000	250,000
Case 2: 3000	50,000	100,000	150,000	200,000	250,000
Case 3: 914.4	10,000	50,000	100,000	150,000	200,000

4.1.1. Governing Equations

A set of governing equations are evaluated in the integral plume model. It is assumed that the equations are obtained from (Crounse B. C., 2000) unless stated otherwise. It should be noted that the integral model uses a top-hat velocity profile simplification as this reduces complexity without detracting from accuracy. A top-hat velocity profile differs from a Gaussian profile also used in modeling in that the top-hat profile assumes a constant velocity across the width of the inner/outer plume. This constant velocity is such that the area under the top-hat profile would be the same as the area under the Gaussian. This simplification reduces complexity because Gaussian profiles contain asymptotic tails on either end of the profile; whereas top-hat profiles end at the edges of the plume it describes. Figure 4.2 is a visual representation of the Gaussian and top-hat profiles.

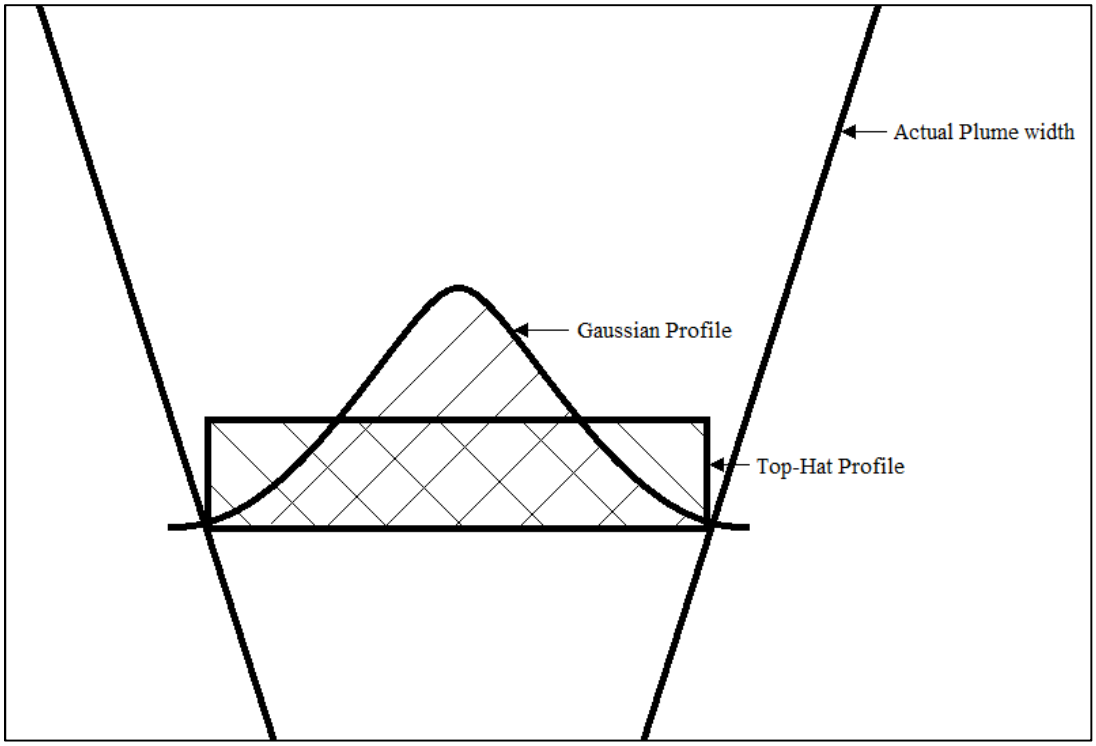

Figure 4.2: Visual description of the difference between Gaussian and Top-Hat velocity profiles.

4.1.1.1. Inner Plume

The basis for the model comes from the self-similarity assumption and entrainment hypothesis. Cross-sectionally averaged profiles yield a set of conservation equations that evolve along the plume centerline, the solution for which yields the profile parameters. It should be noted that multiple classes of bubbles can be present with additional conservation equations; however, in this study, the bubbles are assumed to be identical. The conservation equations are based on several state variables defined as

$$W_b = \frac{1}{6}\pi d_b^3 N_b \rho_b \tag{3.1}$$

where W_b is the flux of droplet mass, d_b is the effective bubble diameter, N_b is the number of bubbles, and ρ_b is the density of hydrocarbons inside the bubble;

$$Q_i = (1 - C_b)\pi b_i^2 u_i \tag{3.2}$$

where Q_i is the flow rate in the inner plume assuming a top hat profile, C_b is the void fraction occupied by bubbles, b_i is the inner plume half-width, and u_i is the average inner plume velocity;

$$M_i = \xi Q_i \rho_i u_i \tag{3.3}$$

where M_i is the kinematic momentum flux of the inner plume including droplets, ξ is an amplification factor given in (Milgram, 1983), and ρ_i is the inner plume density;

$$S_i = Q_i s_i \tag{3.4}$$

where S_i is the salinity flux, and s_i is the inner plume salinity;

$$J_i = Q_i \rho_r c_p T_i \tag{3.5}$$

where J_i is the heat flux, ρ_r is a reference density, c_p is the heat capacity of sea water, and T_i is the temperature of the inner plume; and

$$C_i = Q_i c_i \tag{3.6}$$

where C_i is the mass flux of constituent, and c_i is the concentration of a given constituent in the inner plume.

The buoyant forces are given by

$$\hat{B}_b = g \frac{Q_b}{u_s + u_i}\left(\rho_b - \rho_a\right) \tag{3.7}$$

where $\hat{B}_b$ is the buoyancy force of the bubbles on the entrained plume fluid, g is the acceleration due to gravity, u_s is the slip velocity, and ρ_a is the ambient density given by an equation of state;

$$\hat{B}_i = g \frac{Q_i}{u_i} (\rho_i - \rho_a) \tag{3.8}$$

where $\hat{B}_i$ is the buoyancy force of the inner plume without bubbles.

The mixing equations represent fluxes into and out of the inner plume and ambient water and are based on the entrainment hypothesis. Then entrained fluxes are based on the entrainment hypothesis. Figure 4.3 shows a visual representation of the equations that follow.

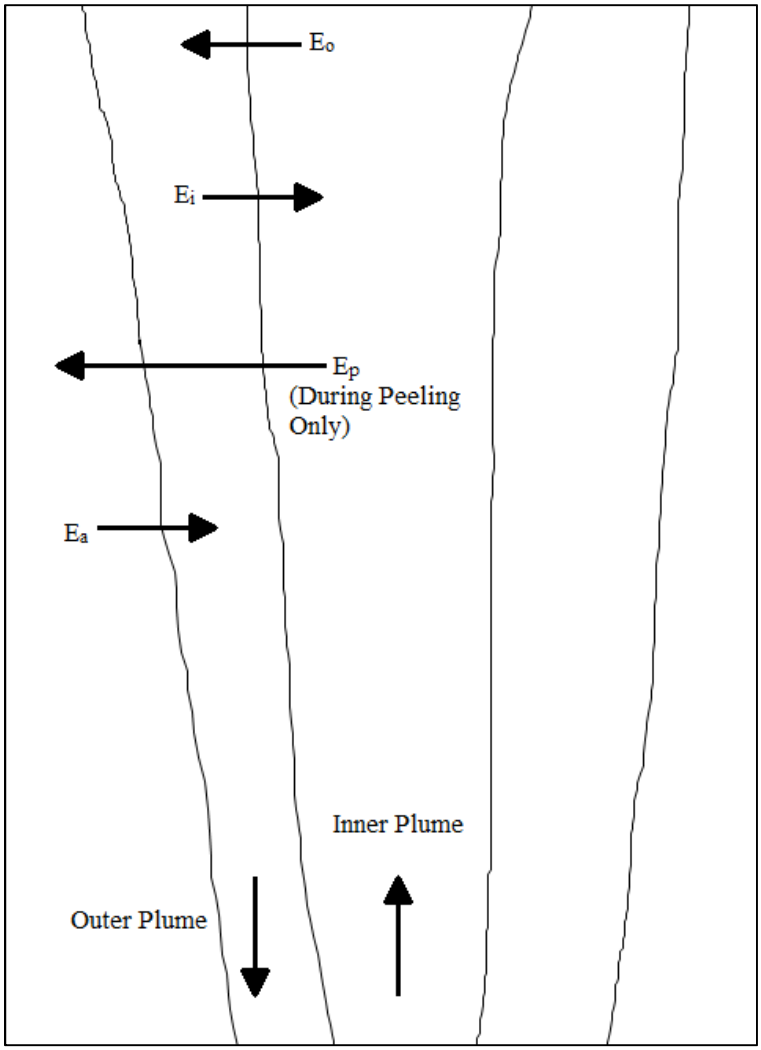

Figure 4.3: Visual representation of entrainment fluxes.

The entrained fluxes are defined as

$$E_i = \begin{cases} 2\pi b_i \alpha_i (u_i - u_o) & (AI) \\ 2\pi b_i \alpha_i u_i & (BC) \end{cases} \tag{3.9}$$

where E_i represents the volume flux into the inner plume from the outer plume if the outer plume is present (AI) or the flow into the inner plume from the ambient fluid if the outer plume is not present (BC), and α_i is the entrainment coefficient;

$$E_o = 2\pi b_i \alpha_o u_o \tag{3.10}$$

where E_o represents the volume flux from the inner plume to the outer plume, α_o is the entrainment coefficient, and u_o is the velocity of the outer plume;

$$E_p = \varepsilon \left(\frac{u_b}{u_i} \right)^2 \left(\frac{B_i}{u_i^2} \right) \tag{3.11}$$

where E_p represents the volume flux peeling from the inner plume into the intrusion, ε is the peeling factor, and B_i is the buoyancy of the inner plume given by

$$B_i = gQ_i \frac{(\rho_i - \rho_a)}{\rho_r} \ . \tag{3.12}$$

Conservation equations are used to close the model so that the general laws of physics apply; for example, conservation of mass equations ensure that the model does not allow mass to be added or eliminated. The inner plume conservation equations are given by the following: Conservation of bubble mass is defined as

$$\frac{dW_b}{dz} = -N_b \pi d_b^2 \frac{K(C_s - c_i)}{u_i + u_s} \tag{3.13}$$

where K is the mass transfer coefficient, and C_s is the saturation concentration. This equation is based on the discrete bubble model found from the Ranz-Marshall dissolution equation (Ranz & Marshall, 1952). Conservation of mass is defined as

$$\frac{dQ_i}{dz} = E_i + E_o + E_p \ . \tag{3.14}$$

The terms represent the flow from the outer plume into the inner plume, the inner plume into the outer plume, and the inner plume into the peeling region respectively. Conservation of momentum is defined as

$$\frac{dM_i}{dz} = \hat{B}_b - \hat{B}_i + E_i \rho_o u_o + E_o \rho_i u_i + E_p \rho_i u_i \tag{3.15}$$

where ρ_o is the outer plume density. The first term represents the buoyancy contribution from the bubbles, and the second represents the buoyancy contribution due to the difference in density between the inner plume and ambient. The remaining terms account for momentum exchange among the inner and outer plumes. The remaining terms account for momentum exchange among the inner and outer plumes. Conservation of mass for a given particulate is defined as

$$\frac{dC_i}{dz} = E_i c_o + E_o c_i + E_p c_i \tag{3.16}$$

where c_o is the concentration of the particulate in the outer plume. The terms represent the concentration flux from the outer plume to the inner plume, from the inner plume to the outer plume, and the inner plume to the peeling region respectively. Conservation of salinity is defined as

$$\frac{dS_i}{dz} = E_i s_o + E_o s_i + E_p s_i \tag{3.17}$$

where s_o is the salinity in the outer plume. The terms in this equation are similar to those described for equation(3.16). Conservation of heat is defined as

$$\frac{dJ_i}{dz} = c_p \rho_{ref} (E_i T_o + E_o T_i + E_p T_i) + \frac{dW_b}{dz} \Delta H_{sol} - \frac{dJ_g}{dz} - \frac{dJ_o}{dz} \tag{3.18}$$

$$\frac{dJ_g}{dz} = -\frac{\pi N_b d_b^{\,2}}{(u_i + u_s)\rho_g c_{pg} \beta_g T_g} \tag{3.19}$$

$$\frac{dJ_o}{dz} = -\frac{\pi N_b d_b^{\,2}}{(u_i + u_s)\rho_o c_{po} \beta_o T_o} \tag{3.20}$$

where T_o is the temperature in the outer plume, dJ_g/dz is the conservation of heat for gas, dJ_o/dz is the conservation of heat for oil, ρ_g is the density of gas, ρ_o is the density of oil, c_{pg} is the specific heat of gas, c_{po} is the specific heat of oil, β_g is the mass transfer coefficient for gas, β_o is the mass transfer coefficient for oil, T_g is the temperature of gas, T_o is the temperature of oil, and ΔH_{sol} is the heat of solution for a given constituent. The first terms are the heat fluxes from the outer plume into the inner plume, the inner plume into the outer plume, and the inner plume into the peeling region respectively. The last term represents the heat transferred via dissolution; additional terms must be added for all constituents.

4.1.1.2. Outer Plume

The outer plume state variables are defined as follows:

$$Q_o = \pi(b_o^2 - b_i^2)u_o \tag{3.21}$$

where Q_o is the outer plume volume flux, and b_o is the outer plume width;

$$M_o = \xi Q_o \rho_o u_o \tag{3.22}$$

where M_o is the momentum flux of the outer plume;

$$S_o = Q_o s_o \tag{3.23}$$

where S_o is the salinity flux of the outer plume;

$$J_o = Q_o \rho_r c_p T_o \tag{3.24}$$

where J_o is the heat flux in the outer plume; and

$$C_o = Q_o c_o \tag{3.25}$$

where C_o is the concentration of the given constituent in the outer plume.

An additional buoyant force term is given as

$$\hat{B}_o = g\frac{Q_o}{u_o}(\rho_o - \rho_a) \tag{3.26}$$

where $\hat{B}_o$ is the buoyancy force of the outer plume.

An additional mixing term is added for the volume transfer from the ambient to the outer plume, E_a, given by

$$E_a = 2\pi b_o \alpha_a u_o \tag{3.27}$$

where α_o is the entrainment coefficient.

The conservation equations for the outer plume are similar to the inner plume.

Conservation of mass is given by

$$\frac{dQ_o}{dz} = E_i + E_o + E_p + E_a \ . \tag{3.28}$$

The terms are similar to those given in equation (3.14) with an added term E_a representing the flow from the outer plume into the ambient.

Conservation of momentum is given by

$$\frac{dM_o}{dz} = \hat{B}_o + E_i\rho_o u_o + E_o\rho_i u_i + E_p\rho_i u_i + E_a\rho_a u_a \tag{3.29}$$

where u_a is the velocity of the ambient water. The first term represents the buoyant force due to the density difference between the outer plume and the ambient. The following terms represent contributions due to the exchange from the outer plume to the inner plume, the inner plume to the outer plume, the inner plume to the peeling region, and the

ambient to the outer plume. Conservation of the concentration of a constituent is given by

$$\frac{dC_o}{dz} = E_i c_o + E_o c_i + E_p c_i + E_a c_a \tag{3.30}$$

where c_a is the concentration of the constituent in the ambient water. The terms are similar to those given for equation (3.16) with the exception of the last term which represents the concentration flux from the ambient to the outer plume. Conservation of salinity is given by

$$\frac{dS_o}{dz} = E_i s_o + E_o s_i + E_p s_i + E_a s_a \tag{3.31}$$

where s_a is the salinity of the ambient water. The terms in this equation are similar to those given for equation (3.30). Conservation of heat is given by

$$\frac{dJ_o}{dz} = c_p \rho_r (E_i T_o + E_o T_i + E_p T_i + E_a T_a) \tag{3.32}$$

where T_a is the temperature of the ambient water. The terms are similar to those given for equation (3.18); however this equation adds a term for heat transfer from the ambient to the outer plume, and it neglects the final term from equation (3.18) due to the assumption that no bubbles travel to the outer plume.

4.1.2. Initial Conditions and Model Closure

The initial conditions are determined using the Wüest equation (2.1) evaluated using Matlab's zeroing function (*fzero*).

The model is closed by determining functions for several variables. The model assumes an entrainment that varies linearly by the difference in velocities between two regions. Entrainment coefficients are determined for the mass transfer between the inner plume and ambient flow, the inner plume and outer plume, and the outer plume and ambient flow. The slip velocity of the bubbles is determined by (Clift, Grace, & Weber, 1978). The mass transfer is determined by the discrete bubble model developed by Wüest, et.al. (1992). The density of seawater is given by an equation of state described in (Crounse B. C., 2000) in the Appendix. Table 4.2 shows the constants used in the SIMP integral model and their values (Socolofsky, Bhaumik, & Seol, "Double-Plume Integral Models for Near-Field Mixing in Multiphase Plumes", 2008).

Table 4.2: Constant coefficients used in the SIMP model.

Coefficient	Value
ρ_r	1031
αi	0.055
αo	0.110
αa	0.110
λ_1	0.20
λ_2	1.20
ε	0.0500
ξ	1.10

4.1.3. Numerical Model

The integral model is evaluated using Matlab's ODE solver (*ode23s*) in the SIMP model. This solver is specifically used for stiff solutions, such as those found when plumes peel. The inner plume is evaluated up to the surface. Then, the model starts at the surface and

evaluates the outer plumes through the water column using the results found for the inner plume. This is an iterative process, so the model will evaluate the inner plume again with the outer plume data. This process will repeat until the answers converge, generally in three to five iterations (Socolofsky, Bhaumik, & Seol, "Double-Plume Integral Models for Near-Field Mixing in Multiphase Plumes", 2008).

4.2. Sensitivity Analysis

This sensitivity analysis is used to determine the relative effects of flow rate on several parameters. The cases run are described in Table 4.1. A base case for the analysis is taken to be at 100,000 BPD of oil, and all of the results will be compared to this base case using the equation (2.15).

The sensitivity bars are labeled with values representing where that particular sensitivity value occurs where *S* represents the location at the source and *I* represents the location at the intrusion.

4.3. Temperature in the Inner Plume

Sensitivity results can be found in the Appendix and are summarized in Figure 4.4 through Figure 4.6. The sensitivities for each case were calculated through the water column. Each result was truncated so that the summarized results below occur between 10 diameters above the source and the trap height for each case. The median was calculated using 1000 points equally spaced along the truncated results. The error bars represent the highest and lowest sensitivity along the truncated water column. Water

depths at which the highest sensitivities occur are also represented on the figure as diameters away from the source, *#D*; the source, *S*; or the intrusion, *I*. It should be noted that values which occur at the source or intrusion would be difficult to model and measure accurately, respectively. Figure 4.4 shows the sensitivity for Case 1, at a depth of 1829 m. The flow rates from Table 4.1 are given using the symbols at the median; the first three represent 250,000 BPD, the second three represent 200,000 BPD and so on. Each of the clusters has 3 sets of medians and error bars representing the bubble diameter in the simulation. The medians are small in comparison to the span of the error bars, showing that sensitivity is relatively small and difficult to measure correctly. The error bars range values of sensitivity that are not unique to individual flow rates; this leads to the conclusion that for measurements taken along the water column, it is difficult to determine flow rate using temperature alone.

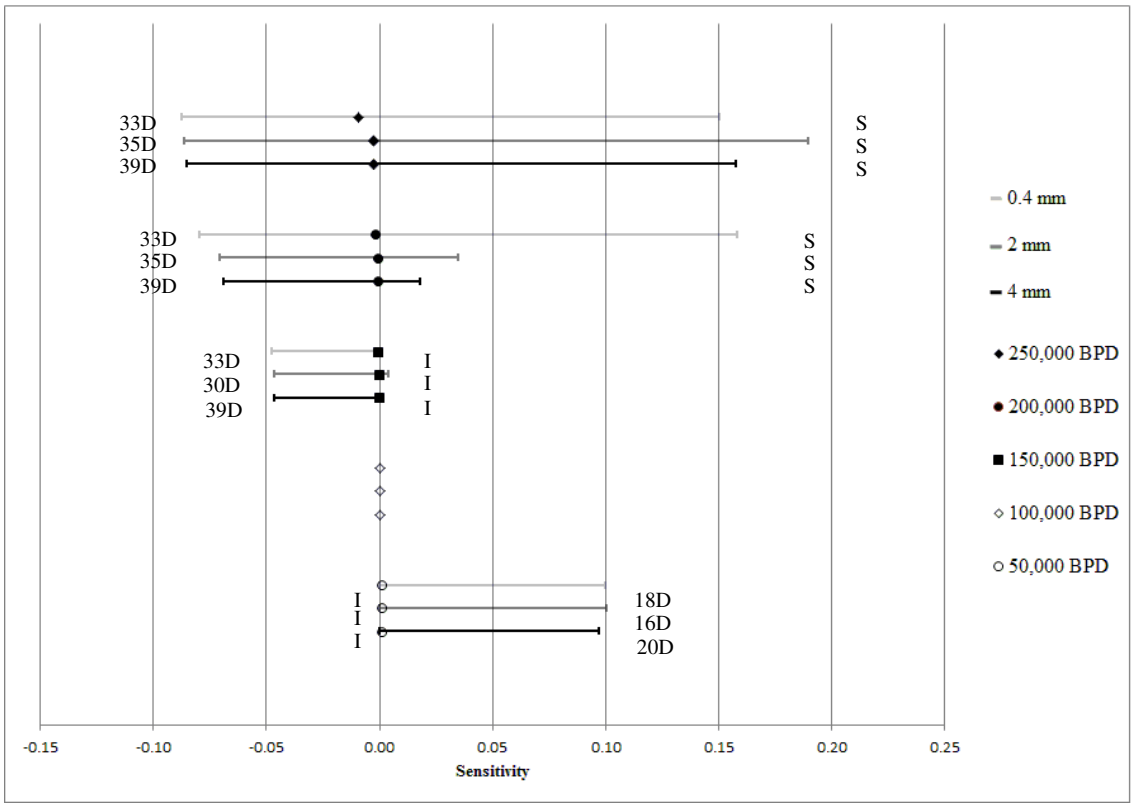

Figure 4.4: Temperature sensitivity for Case 1. The median sensitivity according to bubble diameters 0.4 mm, 2 mm, and 4 mm are given by light, medium, and dark error bar shades respectively. Flow rates of 250, 200, 150, 100, and 50 kBPD are given by filled diamond, filled circle, filled square, unfilled diamond, and unfilled circle respectively. The error bars represent the maximum and minimum sensitivity inside the range of 10 diameters above the source and the trap height.

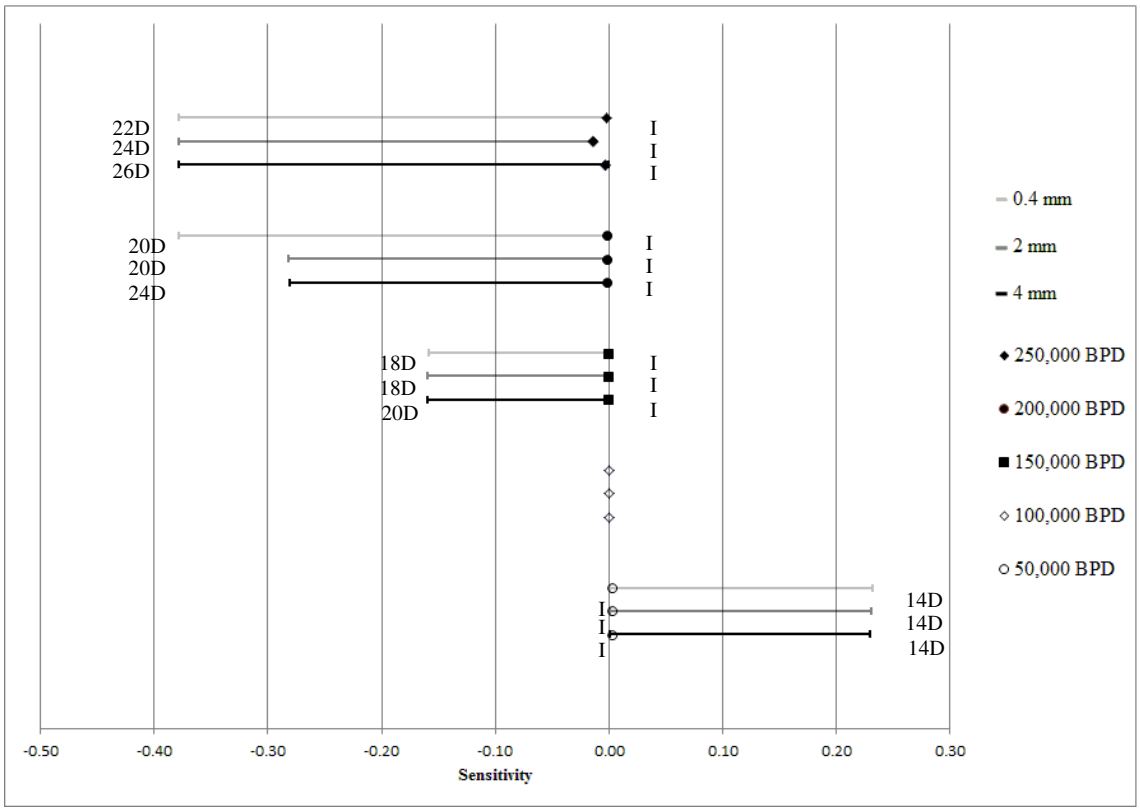

Figure 4.5: Temperature sensitivity for Case 2. The median sensitivity according to bubble diameters 0.4 mm, 2 mm, and 4 mm are given by light, medium, and dark error bar shades respectively. Flow rates of 250, 200, 150, 100, and 50 kBPD are given by filled diamond, filled circle, filled square, unfilled diamond, and unfilled circle respectively. The error bars represent the maximum and minimum sensitivity inside the range of 10 diameters above the source and the trap height.

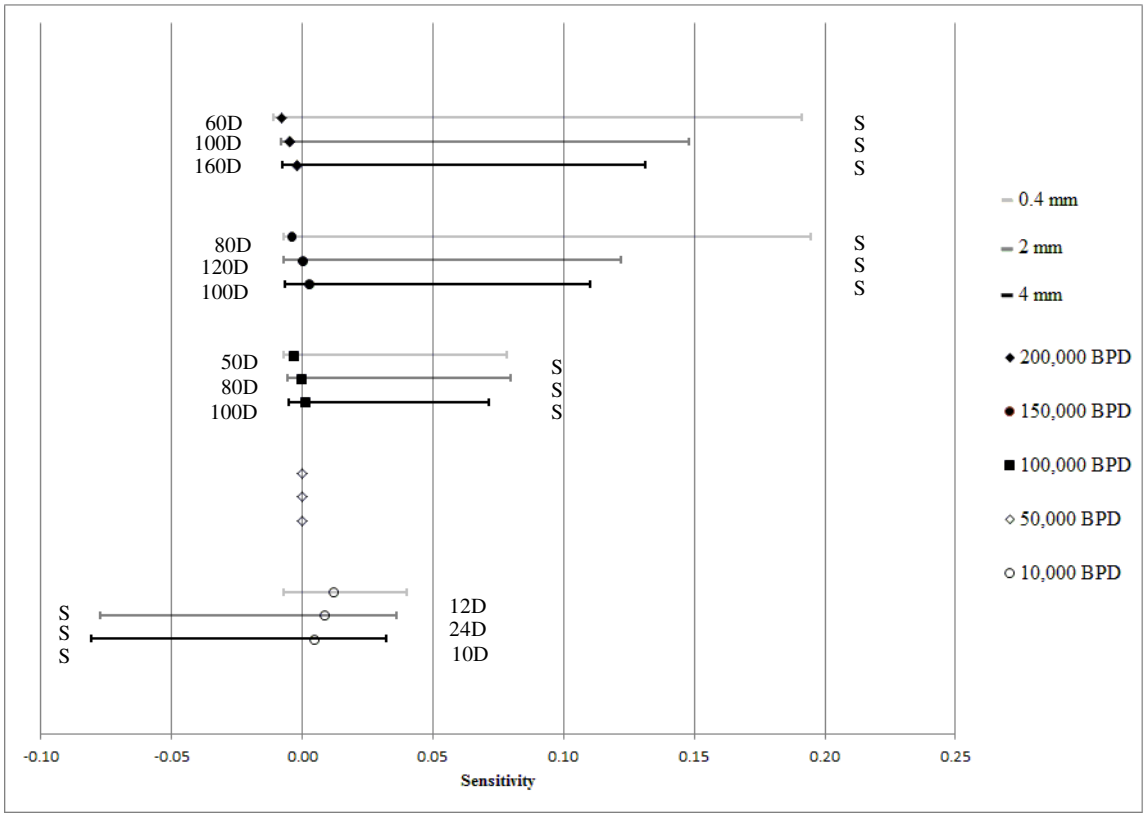

Figure 4.6: Temperature sensitivity for Case 3. The median sensitivity according to bubble diameters 0.4 mm, 2 mm, and 4 mm are given by light, medium, and dark error bar shades respectively. Flow rates of 200, 150, 100, 50 and 10 kBPD are given by filled diamond, filled circle, filled square, unfilled diamond, and unfilled circle respectively. The error bars represent the maximum and minimum sensitivity inside the range of 10 diameters above the source and the trap height.

Figure 4.5 represents Case 2 at 3000 m and shows that the maximum and minimum values are more consistent with large depths. However, the median values remain close to zero relative to the span of the error bars. The error bars for all cases have a region in which there is little to no overlap with other cases; this allows for the use of temperature at certain regions through the water column to be used to determine flow rate.

Figure 4.6 shows the results for Case 3 at a water depth of 914 m. This figure demonstrates more sensitivity in the median in relation to the span of the maximum and minimum. This implies that efforts to determine flow rate through temperature measurements could be more plausible at smaller water depths.

Due to the largely overlapping sensitivities, it is concluded that temperature has an inadequate sensitivity to flow rate for the purposes described in this research.

4.4. Velocity in the Inner Plume

Velocity sensitivity for the entire water column is given in the Appendix. Figure 4.7 through Figure 4.9 truncate the results to the range between 10 diameters above the source and the trap height for each case. The medians were found using 1000 equally spaced points in the truncated range.

Figure 4.7 shows a reasonable separation of the median values in relation to flow rate. The median values show roughly a 15% increase in velocity with a 50,000 BPD increase

in flow rate. The large error span detracts from the parameter's usefulness; however, it should be noted that the medians are relatively close to the inner bound. This allows for at least half of the possible measuring heights to be in close range of the median. This differs from the temperature sensitivity in that the medians are significantly different from the base case.

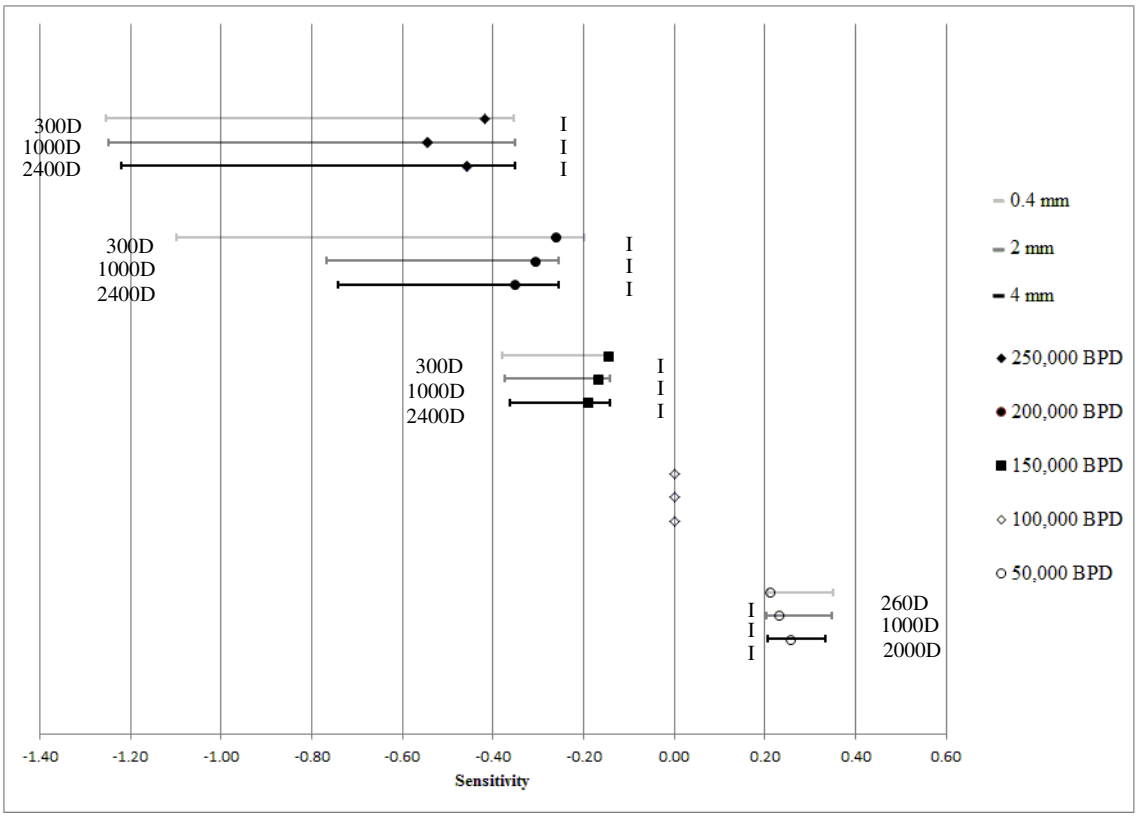

Figure 4.7: Velocity sensitivity for Case 1. The median sensitivity according to bubble diameters 0.4 mm, 2 mm, and 4 mm are given by light, medium, and dark error bar shades respectively. Flow rates of 250, 200, 150, 100, and 50 kBPD are given by filled diamond, filled circle, filled square, unfilled diamond, and unfilled circle respectively. The error bars represent the maximum and minimum sensitivity inside the range of 10 diameters above the source and the trap height.

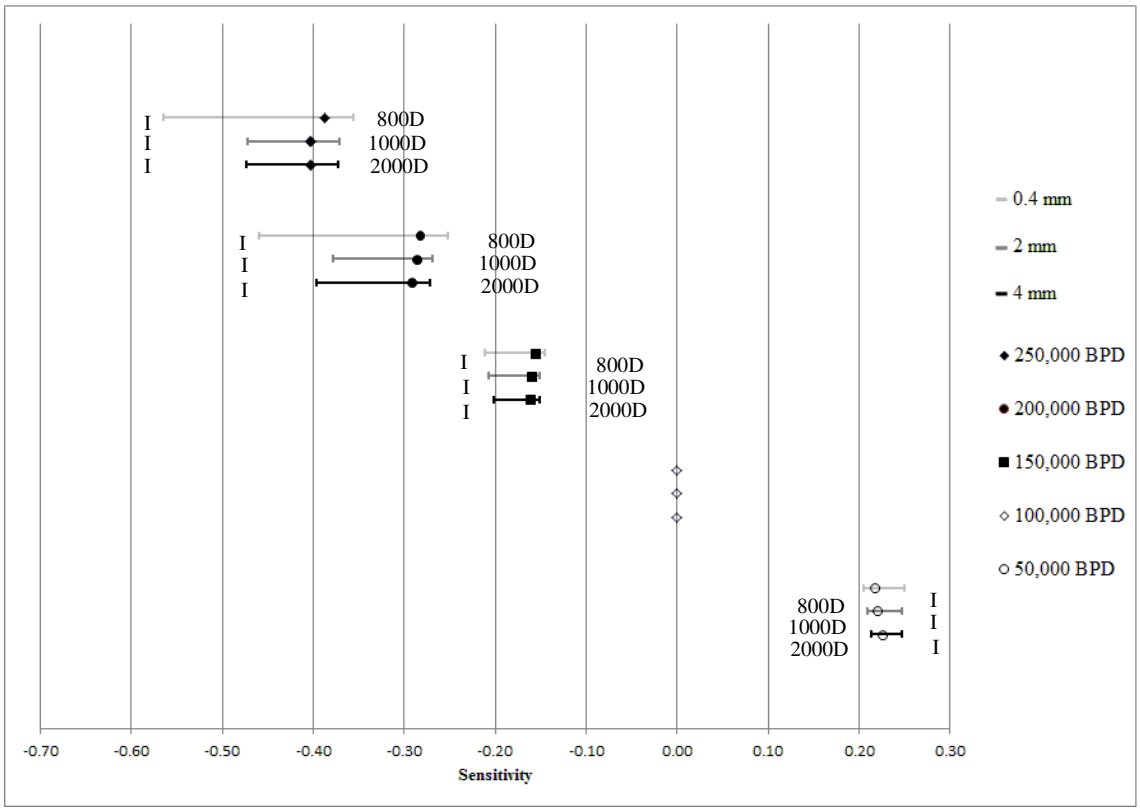

Figure 4.8 : Velocity sensitivity for Case 2. The median sensitivity according to bubble diameters 0.4 mm, 2 mm, and 4 mm are given by light, medium, and dark error bar shades respectively. Flow rates of 250, 200, 150, 100, and 50 kBPD are given by filled diamond, filled circle, filled square, unfilled diamond, and unfilled circle respectively. The error bars represent the maximum and minimum sensitivity inside the range of 10 diameters above the source and the trap height.

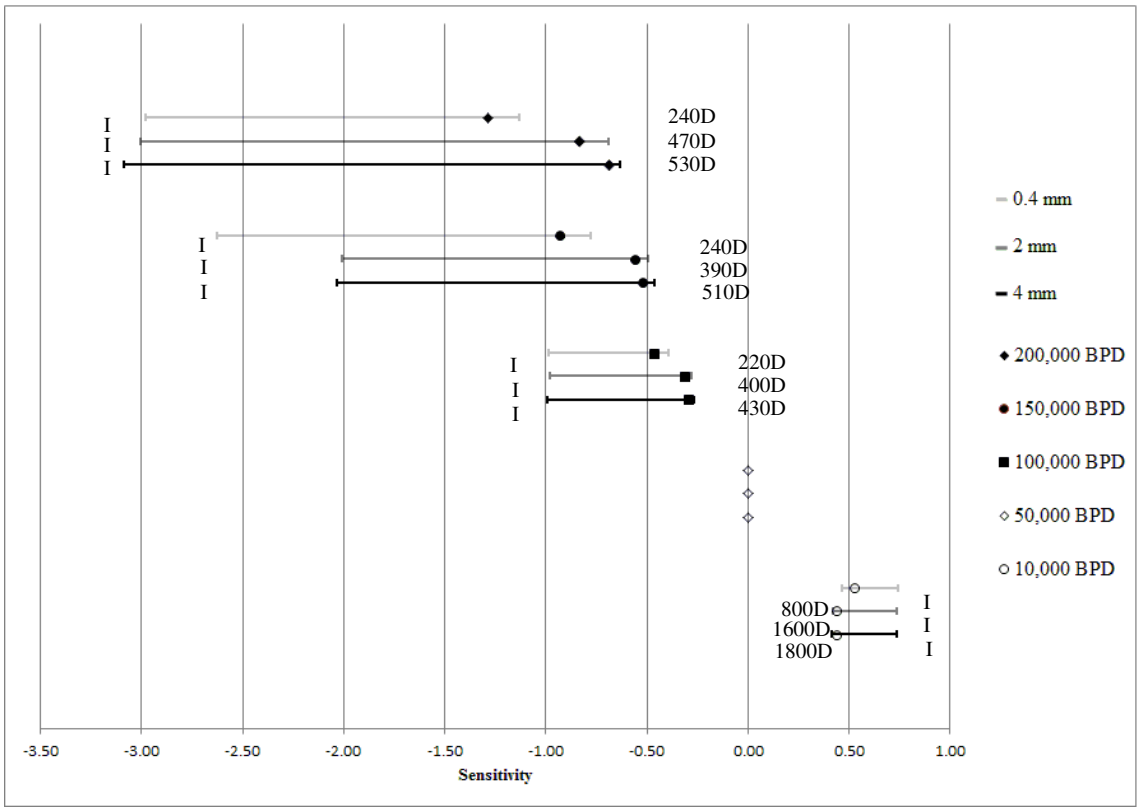

Figure 4.9: Velocity sensitivity for Case 3. The median sensitivity according to bubble diameters 0.4 mm, 2 mm, and 4 mm are given by light, medium, and dark error bar shades respectively. Flow rates of 200, 150, 100, 50 and 10 kBPD are given by filled diamond, filled circle, filled square, unfilled diamond, and unfilled circle respectively. The error bars represent the maximum and minimum sensitivity inside the range of 10 diameters above the source and the trap height.

Figure 4.8 represents velocity sensitivity for Case 2, at 3000 m water depth. It should be noted that the range of sensitivity is significantly smaller at the larger water depth. There is little overlap in the sensitivity range, showing that velocity is an adequate parameter to use in determining flow rate at large depths.

Figure 4.9 shows larger medians and larger ranges of sensitivities. There is large overlap in the error bars. The plausibility of using velocity as the parameter for determining flow rate significantly decreases for smaller depths.

It is concluded that velocity could be used to determine flow rate, but should be used in conjunction with another parameter for confirmation.

4.5. Plume Width

Figure 4.10 through Figure 4.12 contain the sensitivity of plume width to flow rate. The results are listed in the appendix for the full water column. For this analysis the results were truncated to the distance between 10 diameters after the source and the trap height for each case. The error bars represent the highest and lowest sensitivity values in this truncated section.

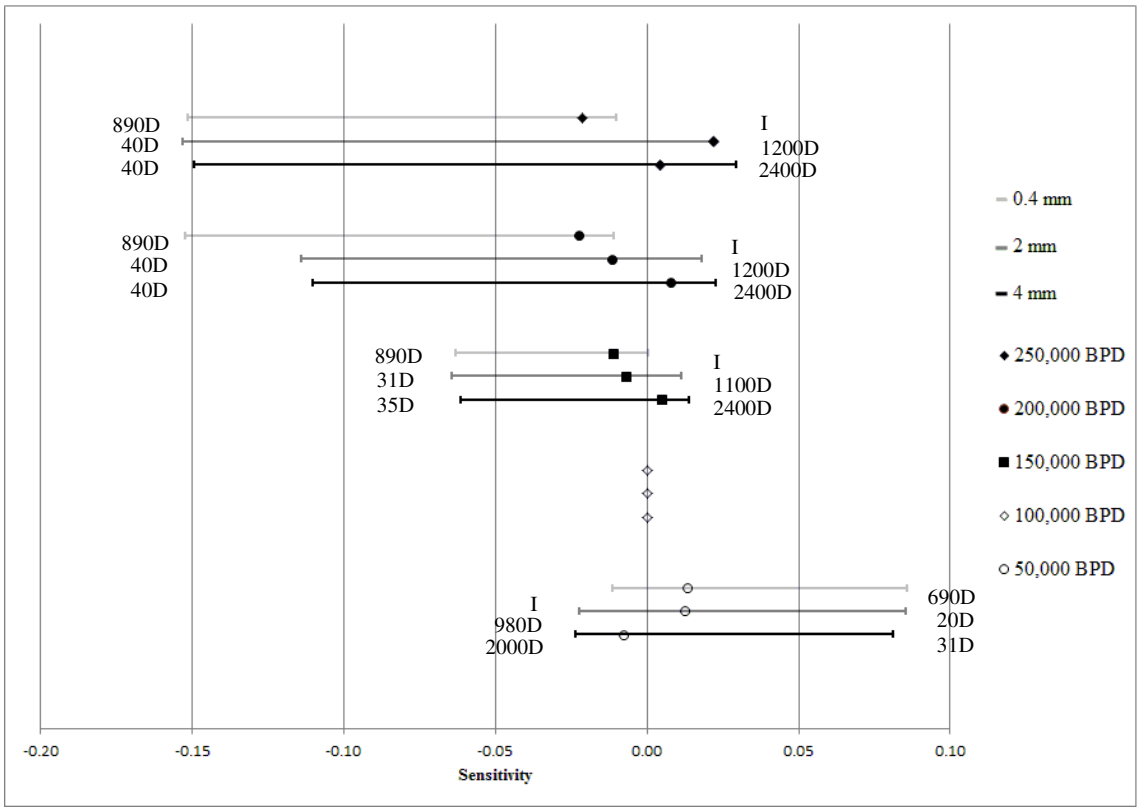

Figure 4.10: Width sensitivity for Case 1. The median sensitivity according to bubble diameters 0.4 mm, 2 mm, and 4 mm are given by light, medium, and dark error bar shades respectively. Flow rates of 250, 200, 150, 100, and 50 kBPD are given by filled diamond, filled circle, filled square, unfilled diamond, and unfilled circle respectively. The error bars represent the maximum and minimum sensitivity inside the range of 10 diameters above the source and the trap height.

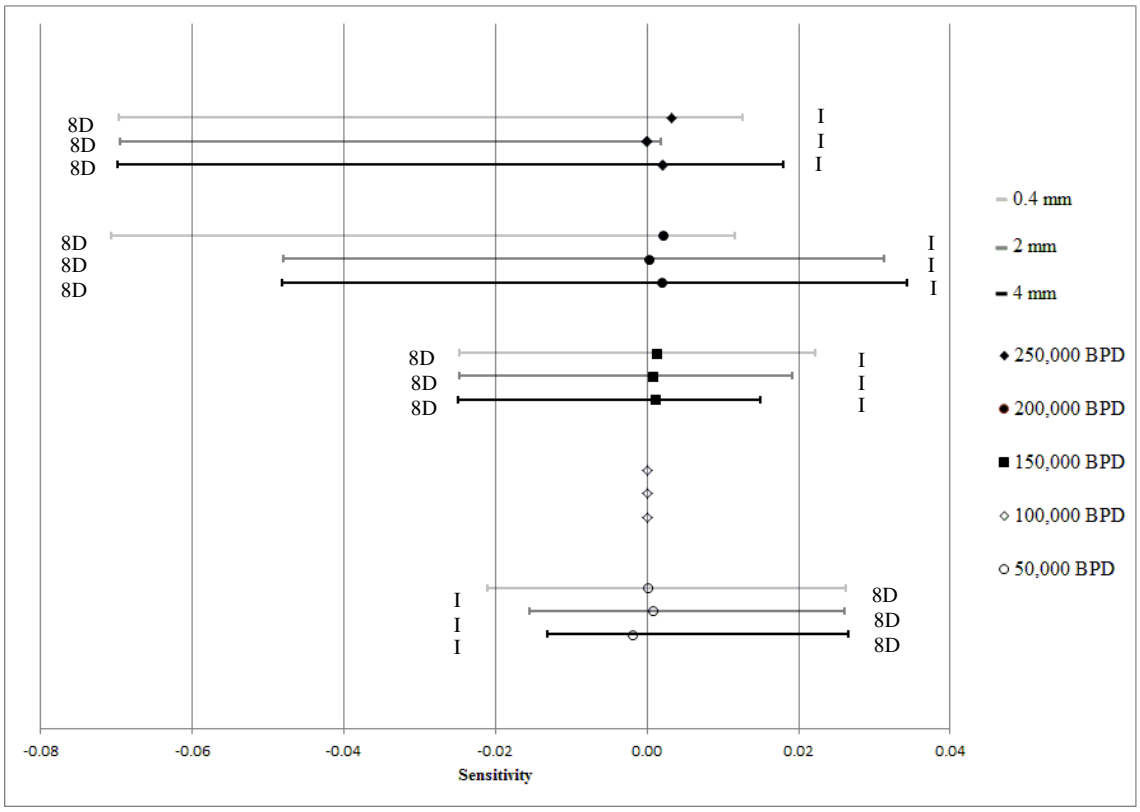

Figure 4.11: Width sensitivity for Case 2. The median sensitivity according to bubble diameters 0.4 mm, 2 mm, and 4 mm are given by light, medium, and dark error bar shades respectively. Flow rates of 250, 200, 150, 100, and 50 kBPD are given by filled diamond, filled circle, filled square, unfilled diamond, and unfilled circle respectively. The error bars represent the maximum and minimum sensitivity inside the range of 10 diameters above the source and the trap height.

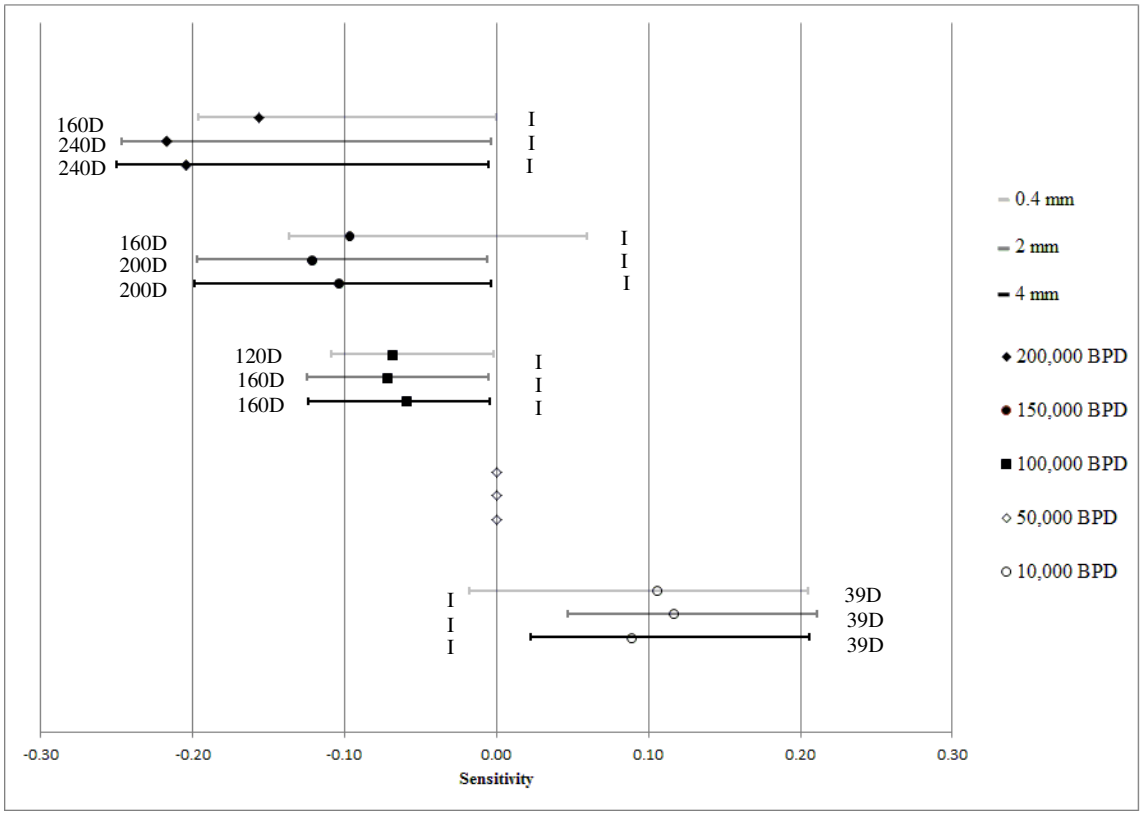

Figure 4.12: Width sensitivity for Case 3. The median sensitivity according to bubble diameters 0.4 mm, 2 mm, and 4 mm are given by light, medium, and dark error bar shades respectively. Flow rates of 200, 150, 100, 50 and 10 kBPD are given by filled diamond, filled circle, filled square, unfilled diamond, and unfilled circle respectively. The error bars represent the maximum and minimum sensitivity inside the range of 10 diameters above the source and the trap height.

Figure 4.10 shows the sensitivity results for Case 1. The median values for all cases are within 5% of the base case. This parameter is therefore unusable for this purposes discussed here. The error bars in this case are also too large to accurately determine sensitivity values in practical instances. This result largely confirms self-similarity in that the spreading angle should be constant independent of flow rate if the plume is strictly self-similar.

As with other parameters, the median values get smaller with greater water depth and the span of error bars reduce in size with greater water depth. The best case for plume width sensitivity is Case 3, but it is not recommended as a parameter to use unless in conjunction with another.

4.6. Trap Height

The sensitivity of trap height to flow rate is shown in Figure 4.13 through Figure 4.15. The true values used in this analysis can be found in the Appendix. Figure 4.13 represents the sensitivity of trap height to flow rate at the Case 1 depth for three possible bubble diameters. It should be noted that for every 50,000 BPD change in flow rate, the trap height sensitivity changes by approximately 0.5%.

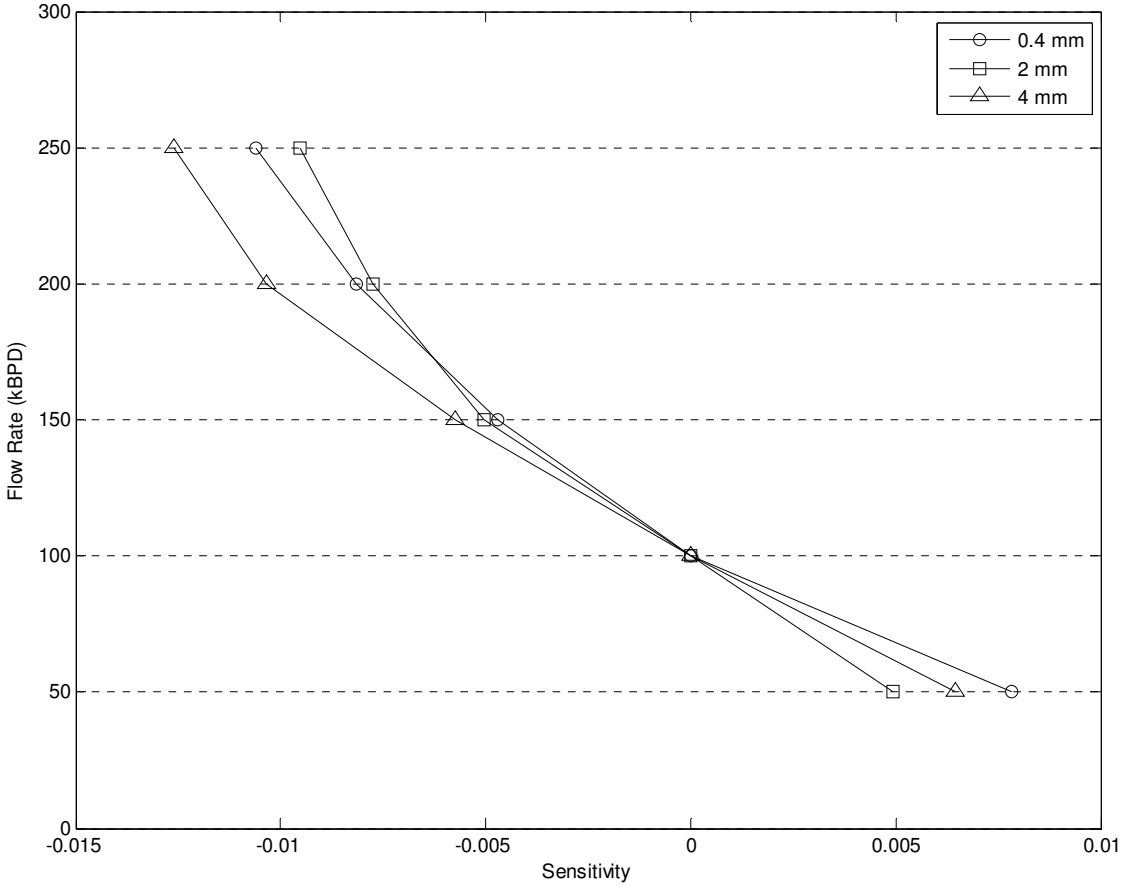

Figure 4.13: Trap height sensitivity relative to flow rate for Case 1. Bubble diameters 0.4 mm, 2 mm, and 4 mm are represented by circle, square, and triangle, respectively. 100,000 BPD is used as the base case.

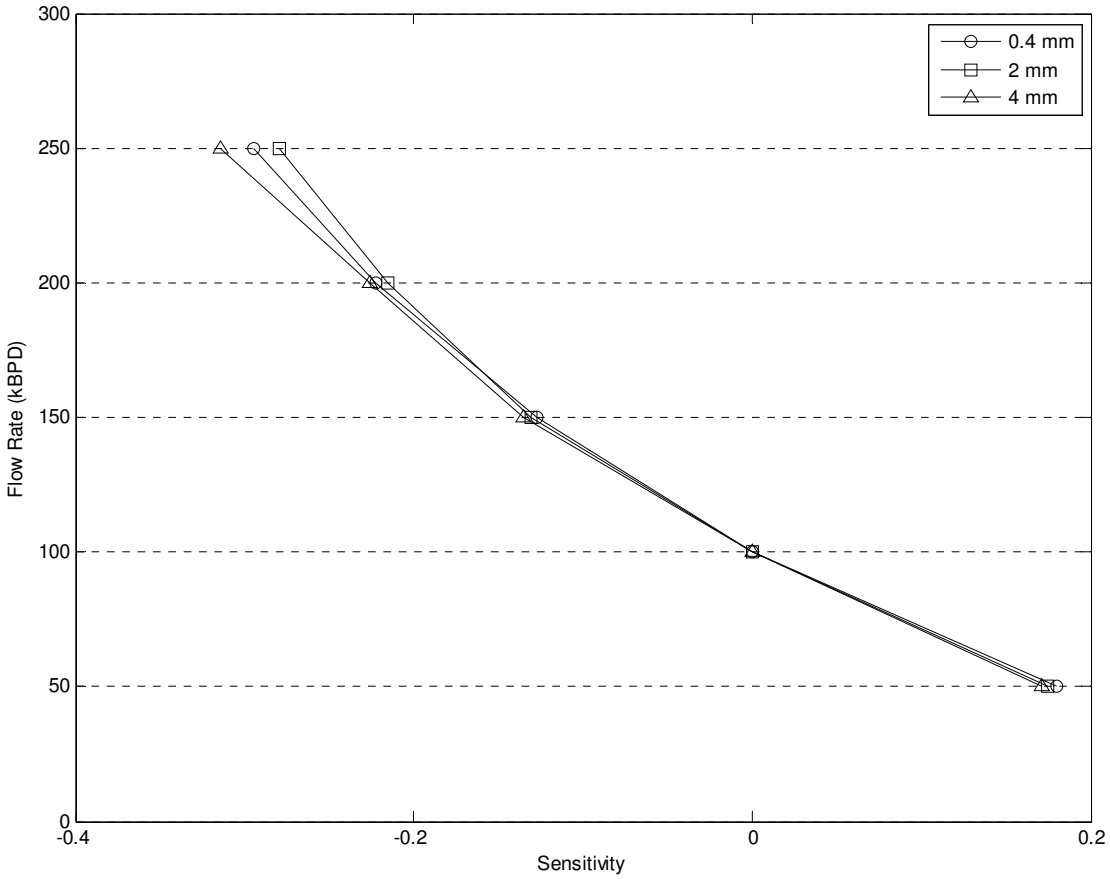

Figure 4.14: Trap height sensitivity relative to flow rate for Case 2. Bubble diameters 0.4 mm, 2 mm, and 4 mm are represented by circle, square, and triangle, respectively. 100,000 BPD is used as the base case.

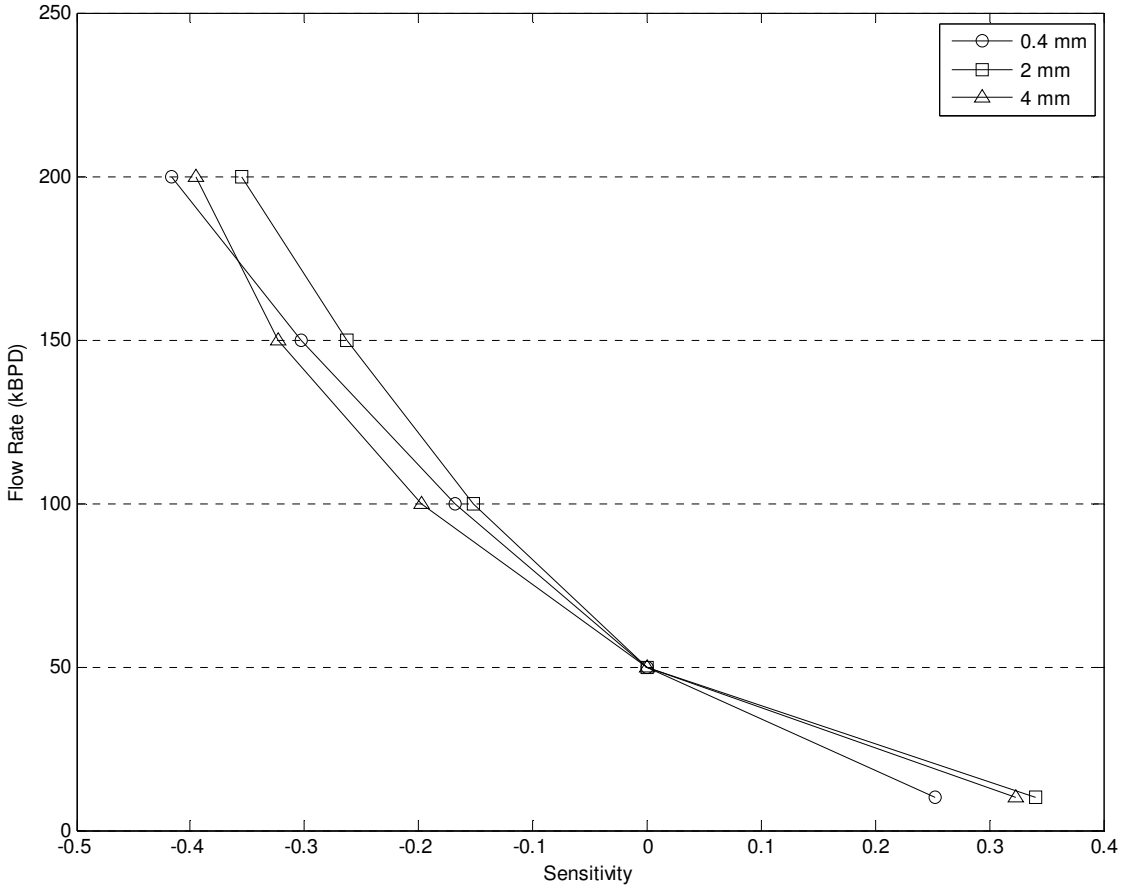

Figure 4.15: Trap height sensitivity relative to flow rate for Case 3. Bubble diameters 0.4 mm, 2 mm, and 4 mm are represented by circle, square, and triangle, respectively. 50,000 BPD is used as the base case.

Both Case 2, shown in Figure 4.14, and Case 3, shown in Figure 4.15, have a larger sensitivity to trap height than Case 1. This leads to the possible conclusion that there is a zone of water depths in which there occurs a minimum range of sensitivity. Case 2 shows a change of approximately 10% per change of 50,000 BPD with less change in sensitivity at higher flow rates. Case 3 shows a change of approximately 10-15% per change of 50,000 BPD with the same change in sensitivity decline at higher flow rates.

4.7. Methane Concentration in the Outer Plume

Figure 4.16 through Figure 4.18 show the sensitivity of methane concentration in the outer plume for Case 1 through 3 respectively. Median values were not calculated for these figures as there should be no ambiguity between flow rates due to the small overlaps. The horizontal lines represent the range of values present in the sensitivity analysis. 100,000 BPD was used as the base case for Case 1 and 2, and 50,000 BPD was used as the base case for Case 3.

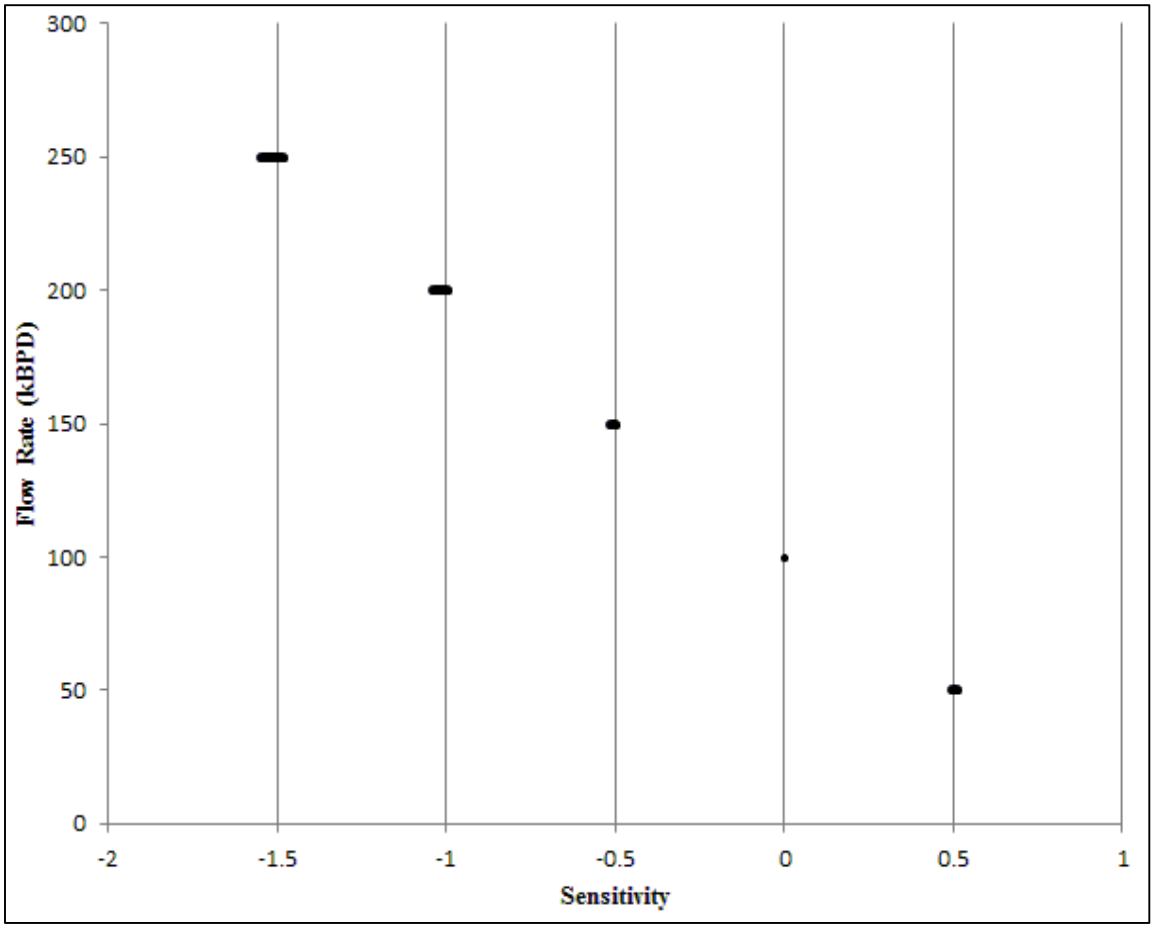

Figure 4.16: Sensitivity for methane concentration in the first intrusion for Case 1.

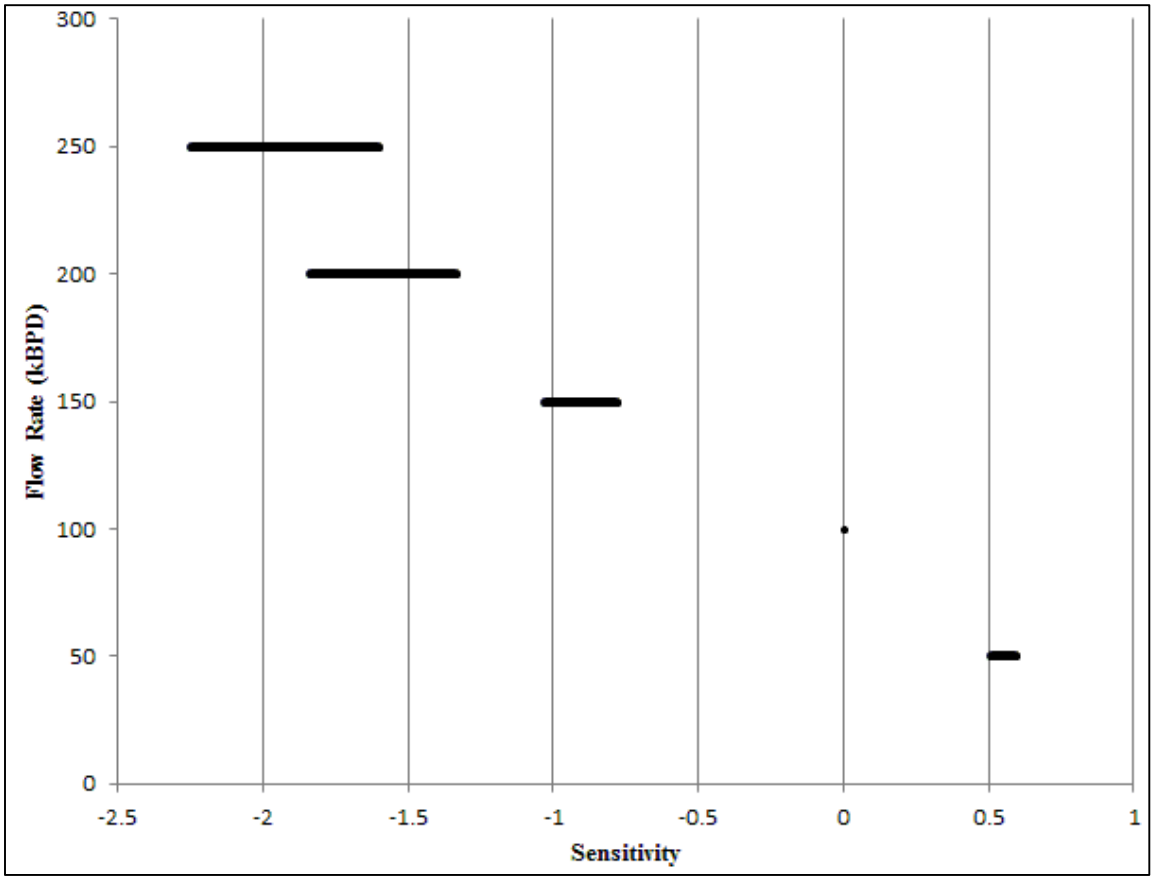

Figure 4.17: Sensitivity for methane concentration in the first intrusion for Case 2.

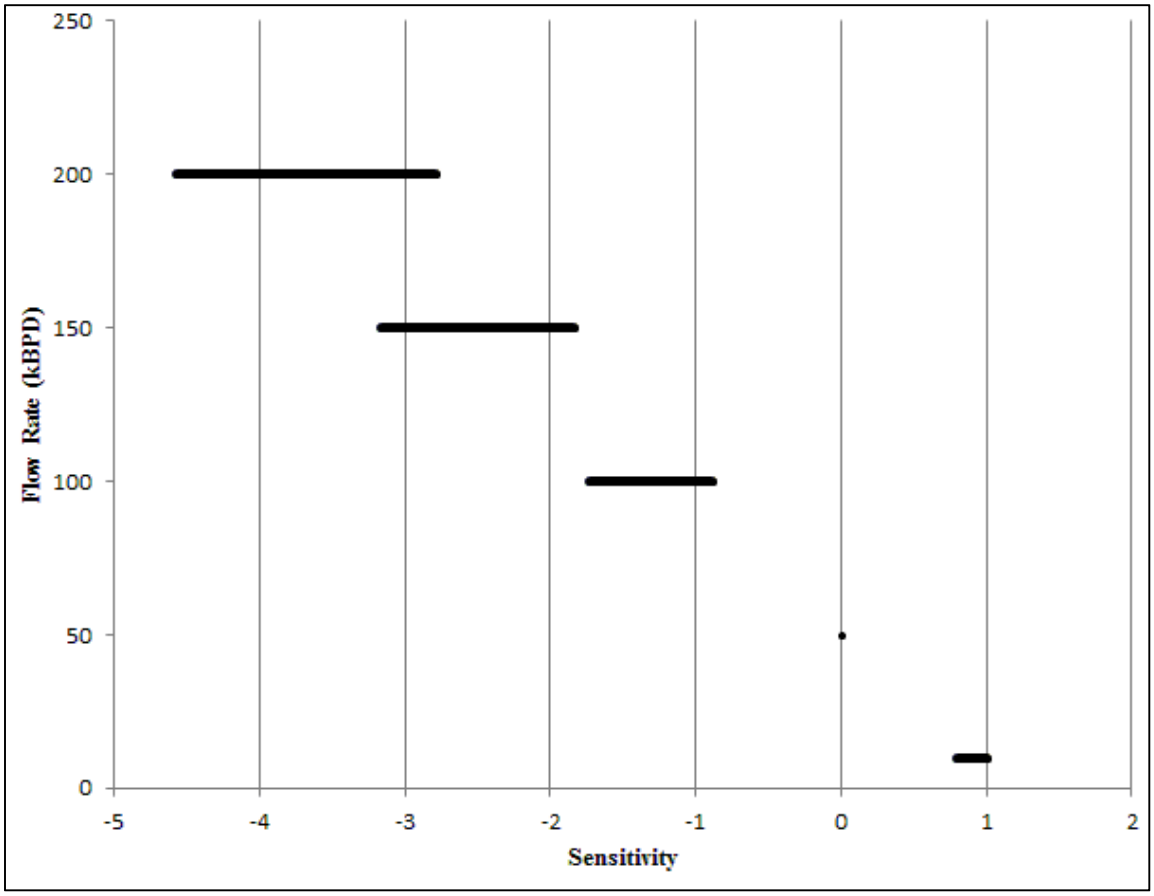

Figure 4.18: Sensitivity for methane concentration in the first intrusion for Case 3.

Case 1 has the smallest ranges of sensitivity values, showing that this technique is most accurate in this case. As flow rates increase by 50 kBPD, sensitivity increases by about 50% for Case 1. The largest overlap occurs in Case 2 between 200 and 250 kBPD, but in the case that this situation occurs, other parameters can be used to confirm flow rate. The sensitivity roughly increases by 50% for every increase in 50 kBPD. Case 3 shows the largest sensitivity variations between flow rates at roughly 125% for every 50 kBPD change.

These values show that the most reliable parameter for determining flow rate in a plume is methane concentration in the first intrusion. Other parameters should only be used in conjunction with this parameter. ROVs can easily obtain a water sample from the outer plume, allowing this parameter to be easily measured.

4.8. Comparison to Predictions of Empirical Equations

Non-dimensional values were discussed in Section 2.2. The non-dimensional velocity and trap height were both used in this section to determine if sensitivity can be predicted using these non-dimensional equations.

4.8.1. Non-Dimensional Velocity

Equation (1.4) was used in determining the characteristic velocity for each set of conditions. A weighted average was performed to match the characteristic velocity to the numerical values such that larger flow rates had larger effects on the average and is defined as

$$Avg. = \frac{\sum_{1}^{N} Q_N V_N}{\sum_{1}^{N} Q_N} \tag{3.33}$$

where $Avg.$ is the weighted average, Q_N represents each flow rate, and V_N represents the values for which the average is taken. Figure 4.19 through Figure 4.21 show the sensitivity for numerical medians for each condition in Case 1 as the solid symbol and the non-dimensional value in the unfilled symbol. Case 1 shows reasonable correlation between non-dimensional and true values. Correlation is similar regardless of bubble diameter. The sensitivity in this case varies less than 10% for all values.

Figure 4.22 through Figure 4.24 show the sensitivity comparison for true and non-dimensional values for Case 2. It is apparent that Case 2 shows a higher correlation between both values than Case 1 for all bubble diameters. The sensitivity varies less than 10% for all values.

Figure 4.25 through Figure 4.27 show the sensitivity for the median and non-dimensional values for Case 3. Though the correlation is still high for this set of cases, the sensitivity can vary as much as 50%.

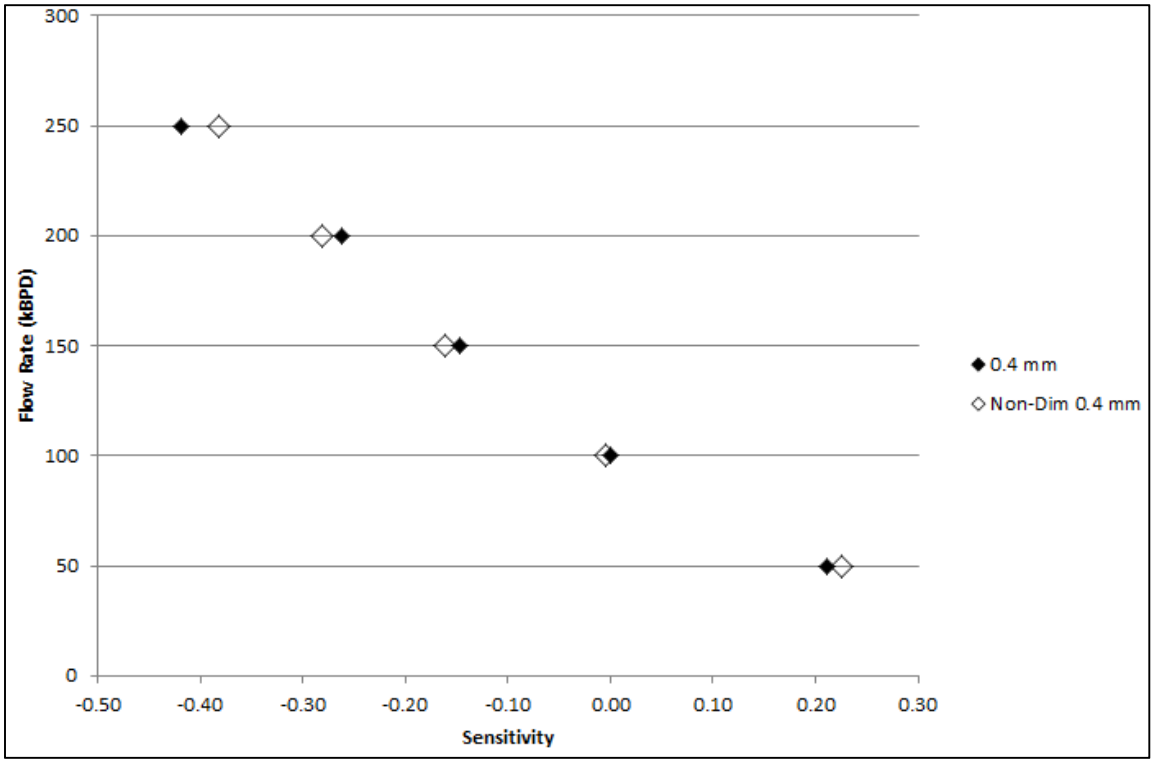

Figure 4.19: Median velocity and non-dimensional velocity for Case 1 with a bubble diameter of 0.4 mm.

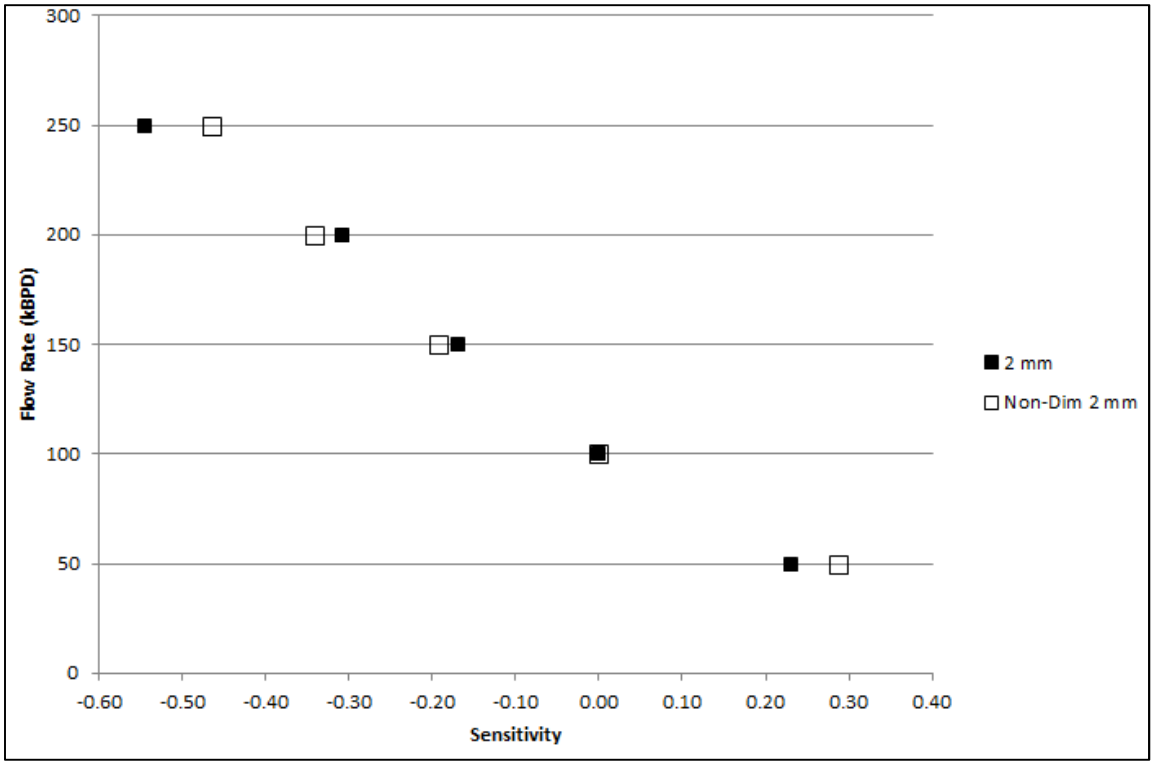

Figure 4.20: Median velocity and non-dimensional velocity for Case 1 with a bubble diameter of 2 mm.

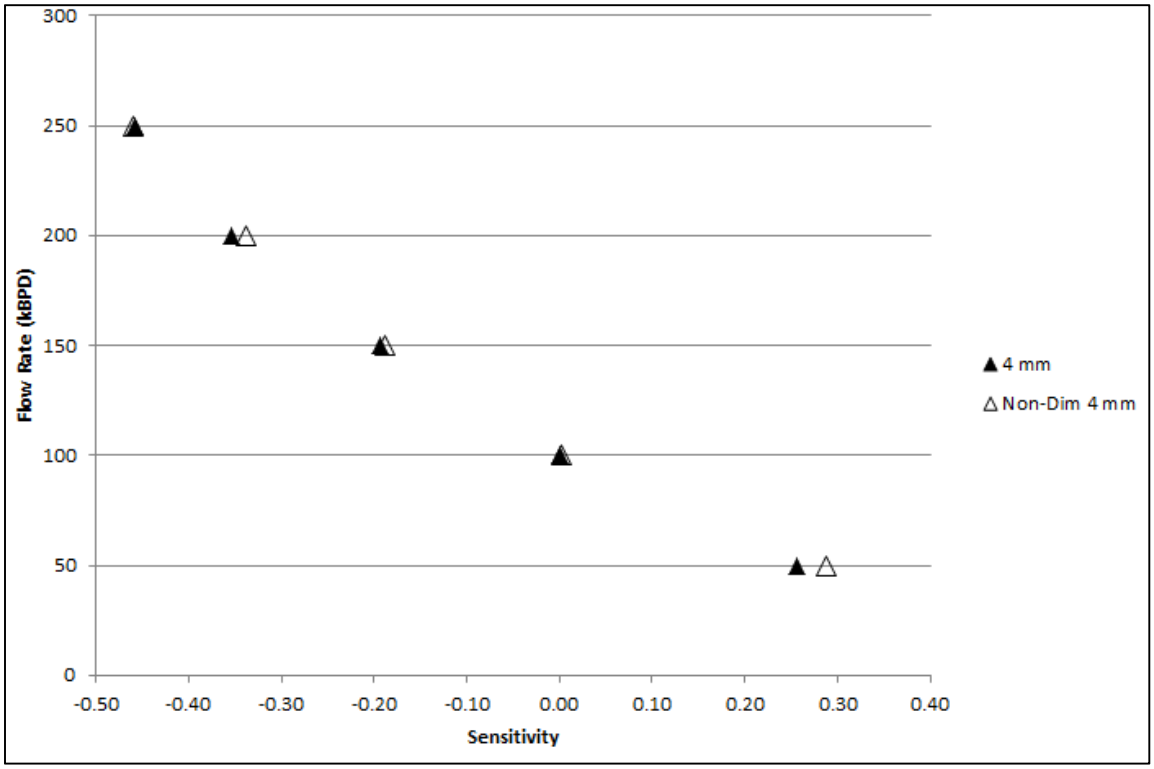

Figure 4.21: Median velocity and non-dimensional velocity for Case 1 with a bubble diameter of 4 mm.

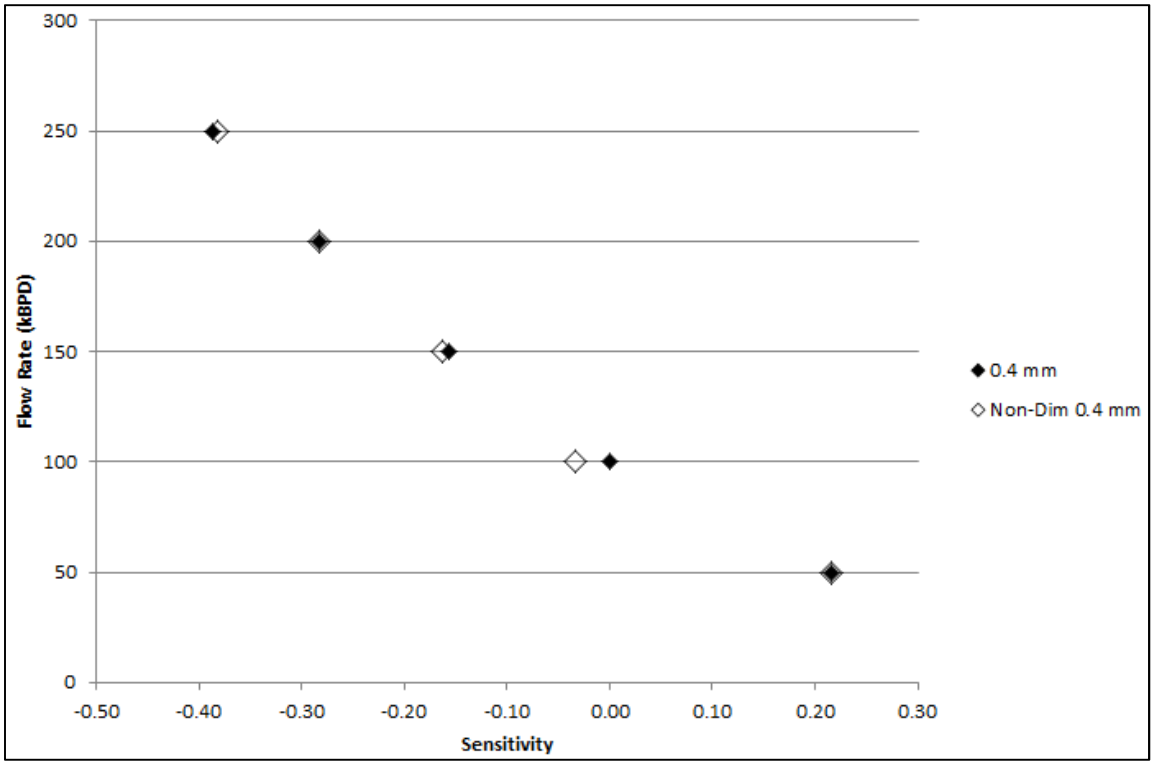

Figure 4.22: Median velocity and non-dimensional velocity for Case 2 with a bubble diameter of 0.4 mm.

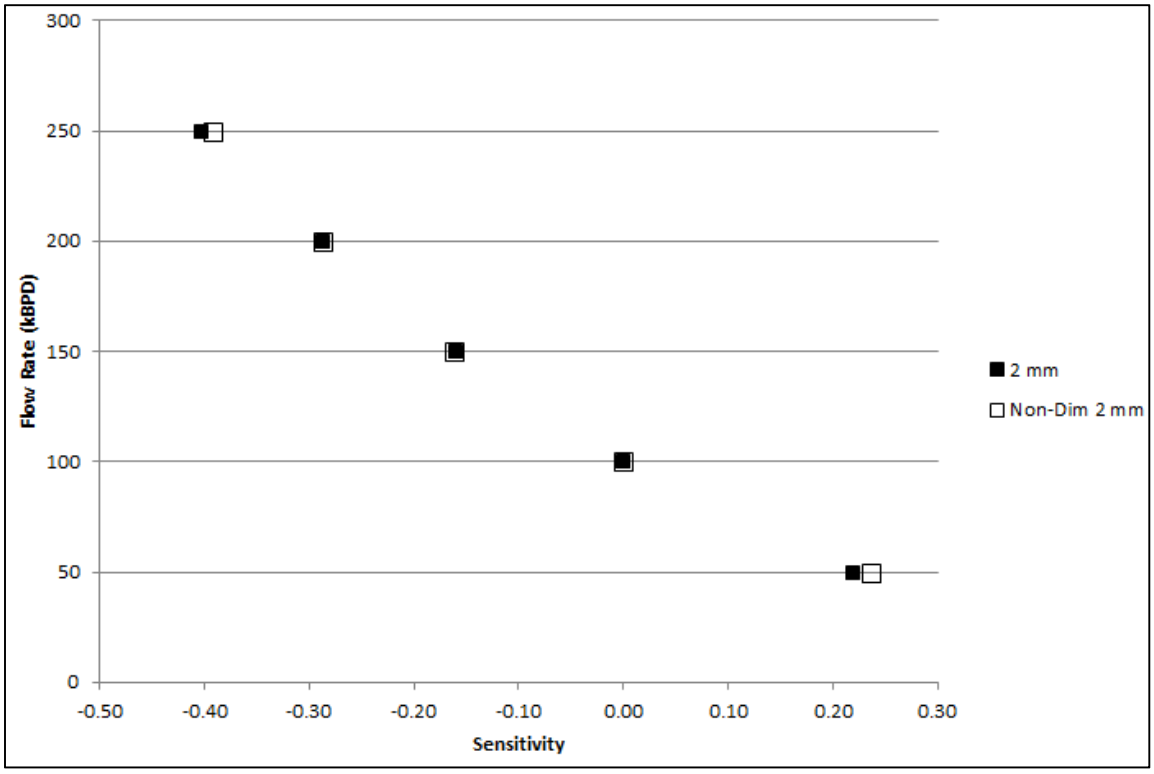

Figure 4.23: Median velocity and non-dimensional velocity for Case 2 with a bubble diameter of 2 mm.

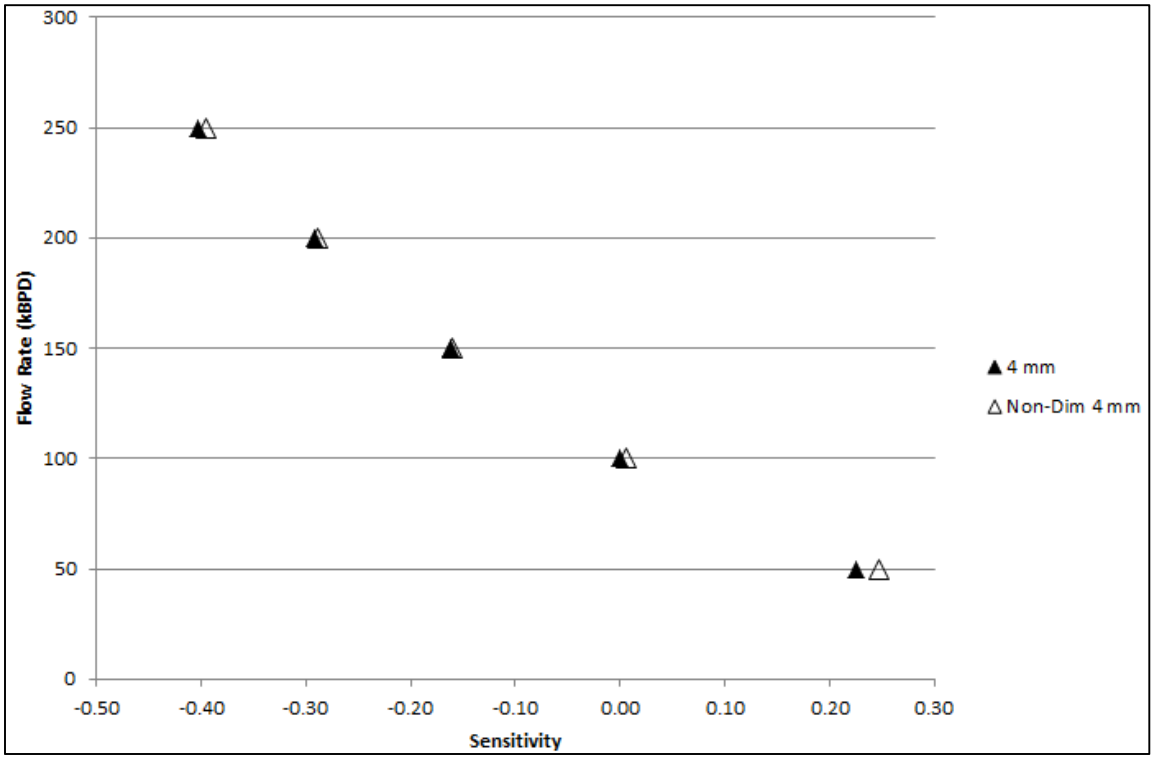

Figure 4.24: Median velocity and non-dimensional velocity for Case 2 with a bubble diameter of 4 mm.

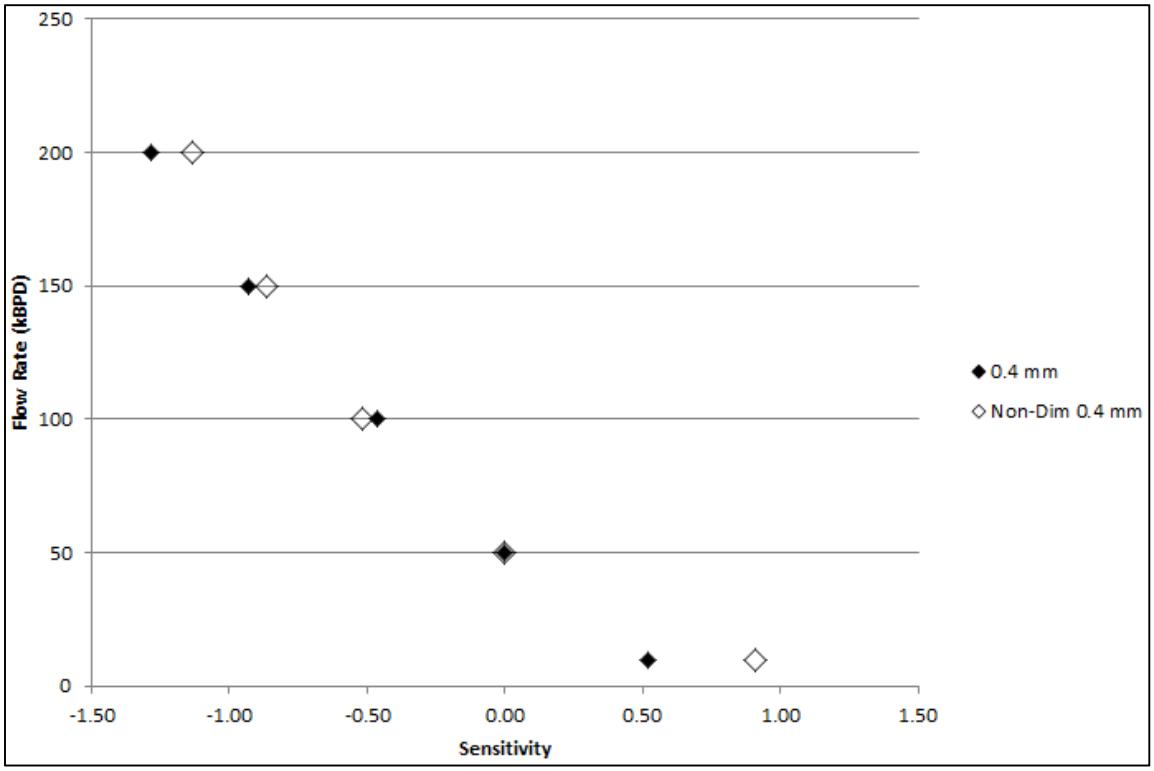

Figure 4.25: Median velocity and non-dimensional velocity for Case 3 with a bubble diameter of 0.4 mm.

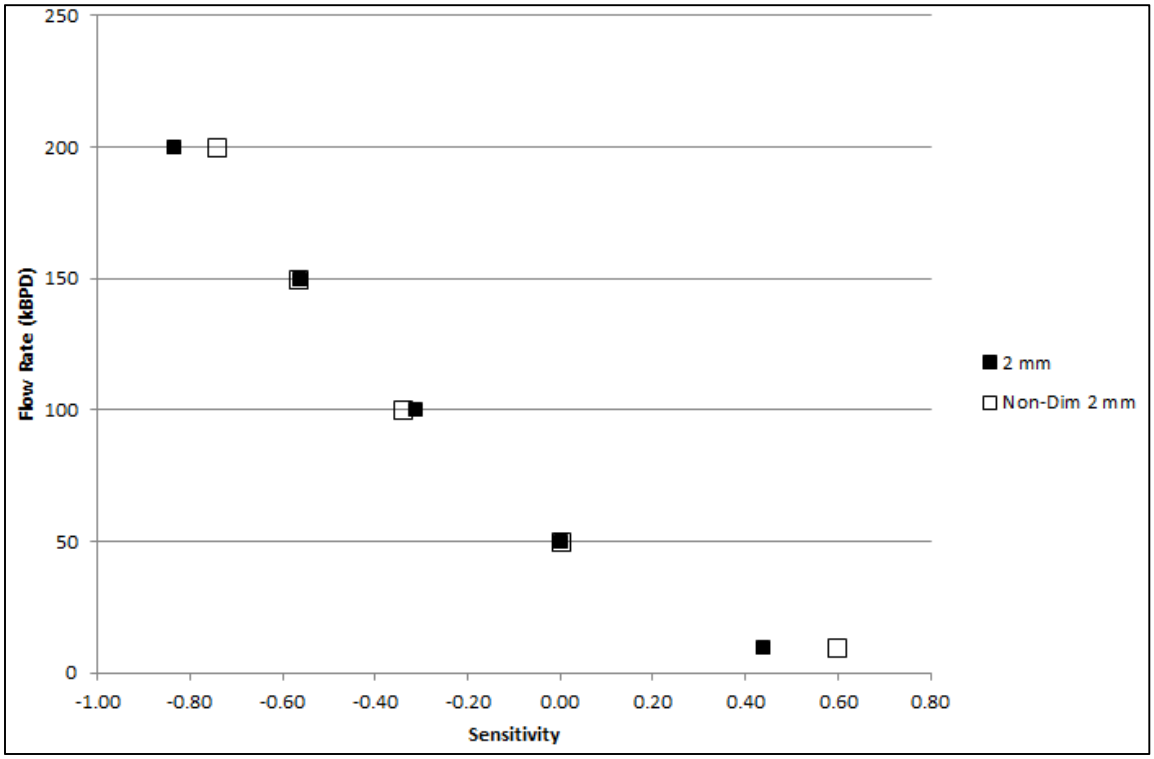

Figure 4.26: Median velocity and non-dimensional velocity for Case 3 with a bubble diameter of 2 mm.

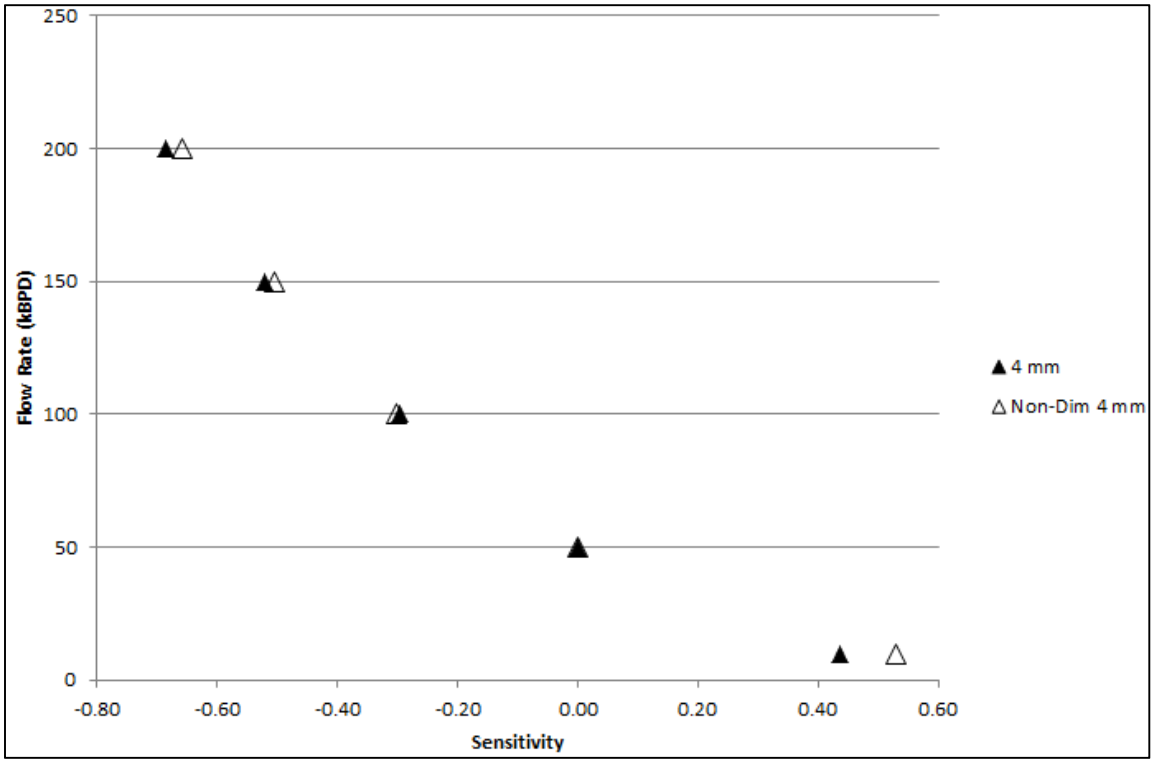

Figure 4.27: Median velocity and non-dimensional velocity for Case 3 with a bubble diameter of 4 mm.

The sensitivities of the median and non-dimensional velocity for all cases show high correlation. Deeper water shows a closer relation between values than shallower water. This analysis shows that non-dimensional values can be used to predict reasonably accurate sensitivity values for velocity when only one data point is available. It also shows that the empirical equations and the model behave similarly despite the fact that the empirical equations lack dissolution. This is further evidence that the model solution is rather weakly dependent on leak rate and, hence, it will be difficult to estimate leak rate by matching to measured data.

4.8.2. Non-Dimensional Trap Height

Equation (1.7) was used to determine the non-dimensional trap height. The multiplied coefficient was found by setting the sensitivity of the maximum flow rate to the non-dimensional sensitivity.

Figure 4.28 through Figure 4.30 show the sensitivity for trap height and non-dimensional trap height for Case 1 for diameters of 0.4 mm, 2 mm, and 4 mm respectively. Correlation between both values is reasonable.

Figure 4.31 through Figure 4.33 show the sensitivity of trap height and non-dimensional trap height for Case 2 for bubble diameters of 0.4 mm, 2 mm, and 4 mm respectively. Correlation remains reasonable with slightly closer results than Case 1.

Figure 4.34 through Figure 4.36 represent the sensitivity of trap height and non-dimensional trap height for Case 3 with bubble diameters of 0.4 mm, 2 mm, and 4 mm respectively. Correlation remains very high for this case as well.

All cases have significantly large correlation between the trap height and non-dimensional trap height sensitivities. Trap height sensitivity can be predicted using the non-dimensional values and one true value.

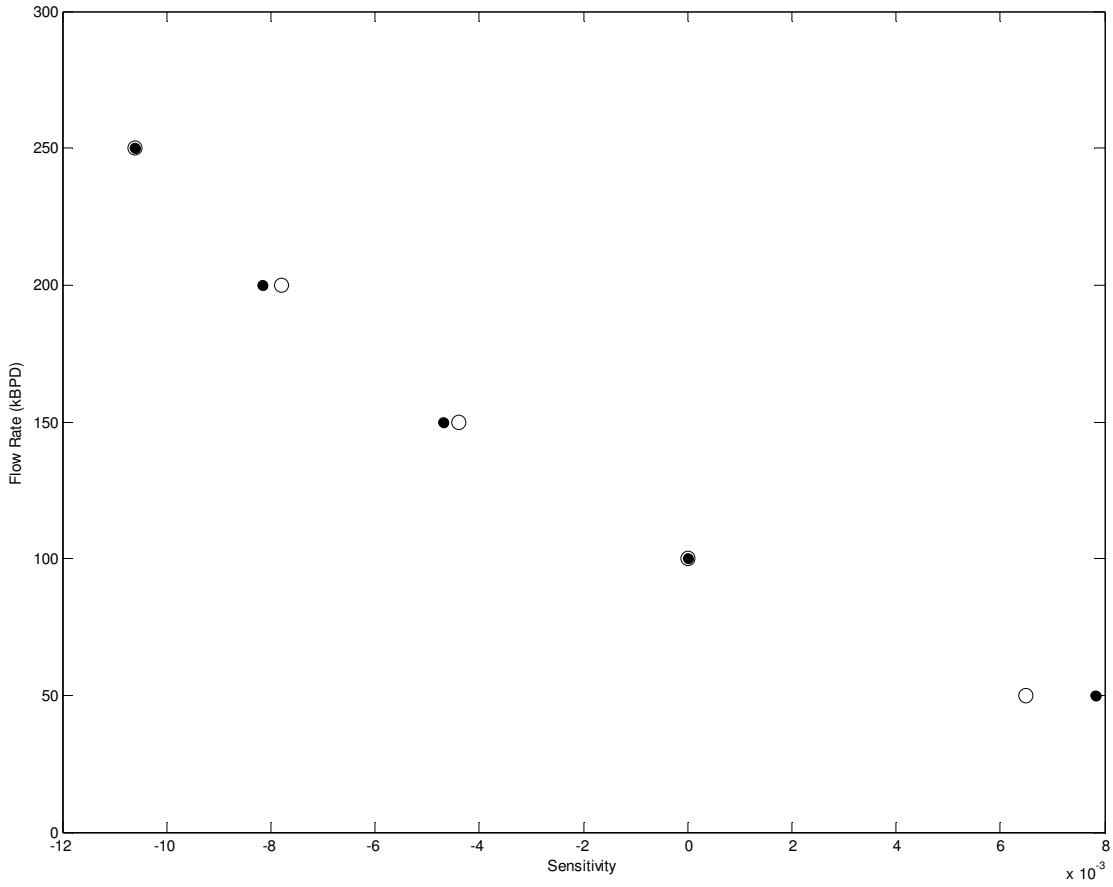

Figure 4.28: Sensitivity of trap height (solid symbols) and non-dimensional trap height (unfilled symbols) for Case 1 with 0.4 mm bubble diameter.

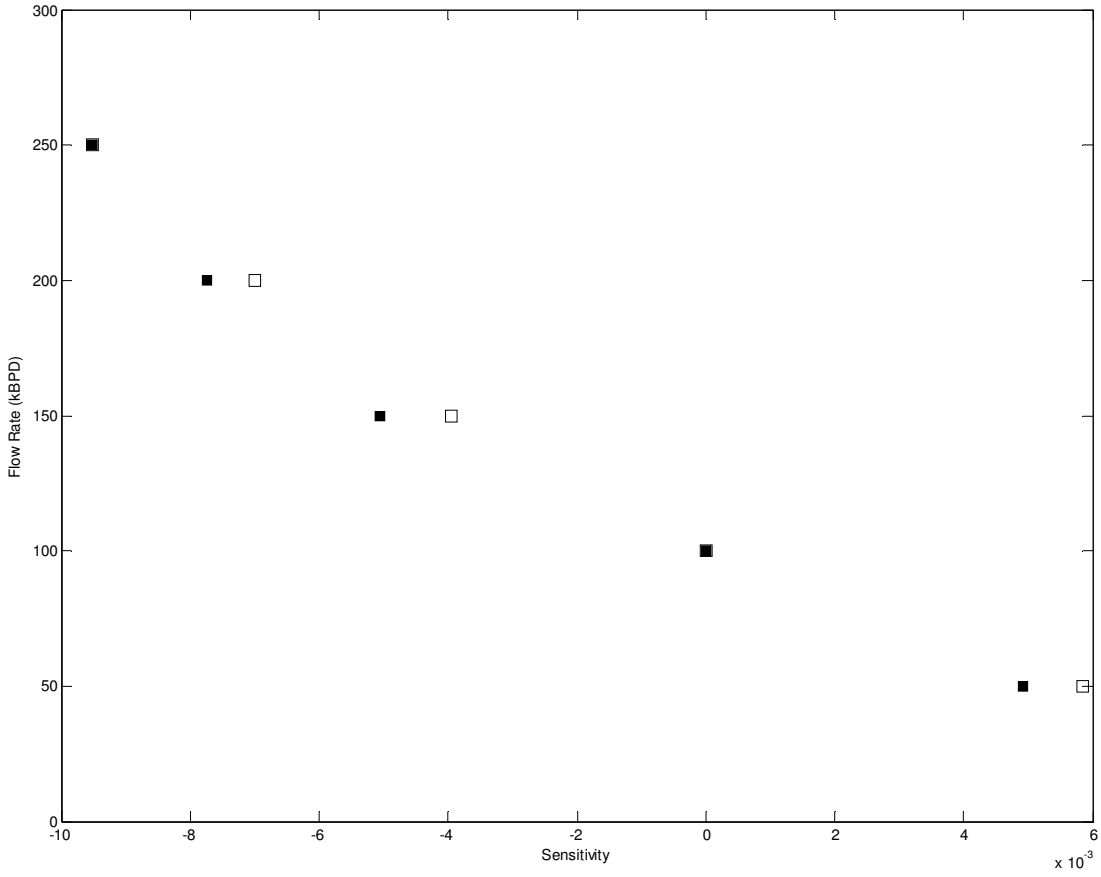

Figure 4.29: Sensitivity of trap height (solid symbols) and non-dimensional trap height (unfilled symbols) for Case 1 with 2 mm bubble diameter.

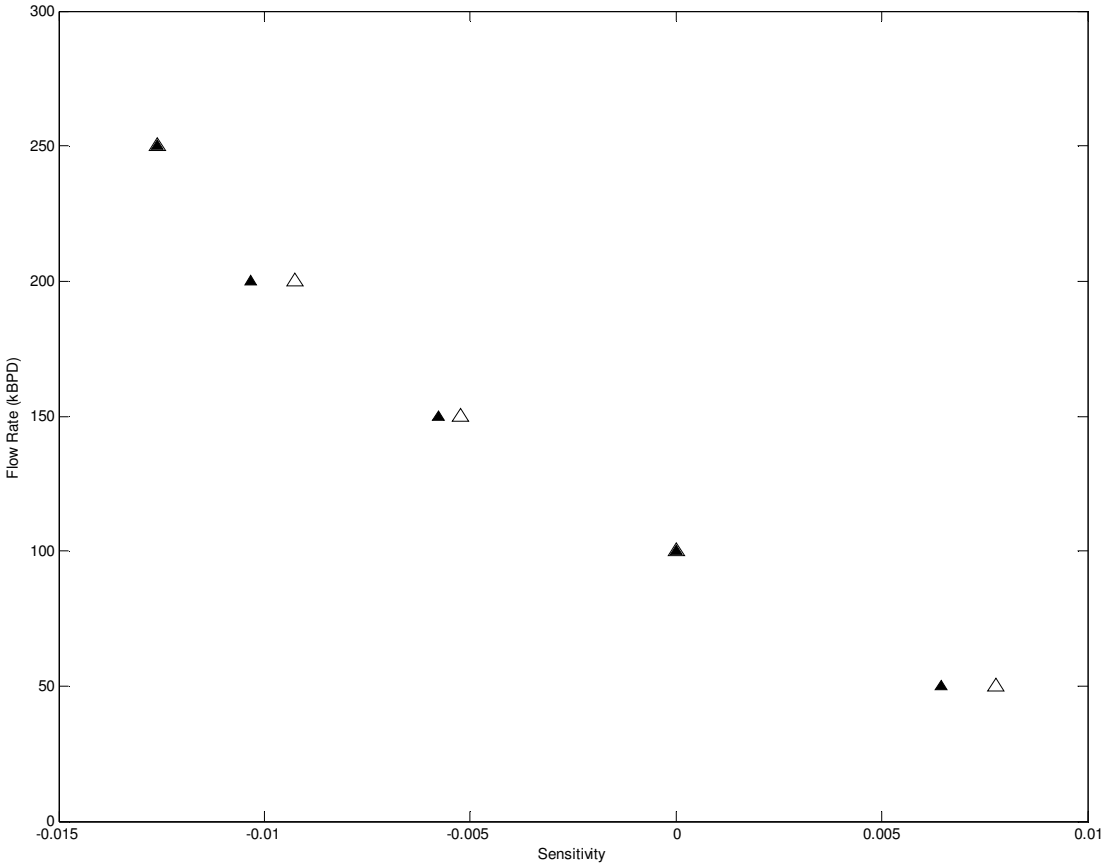

Figure 4.30: Sensitivity of trap height (solid symbols) and non-dimensional trap height (unfilled symbols) for Case 1 with 4 mm bubble diameter.

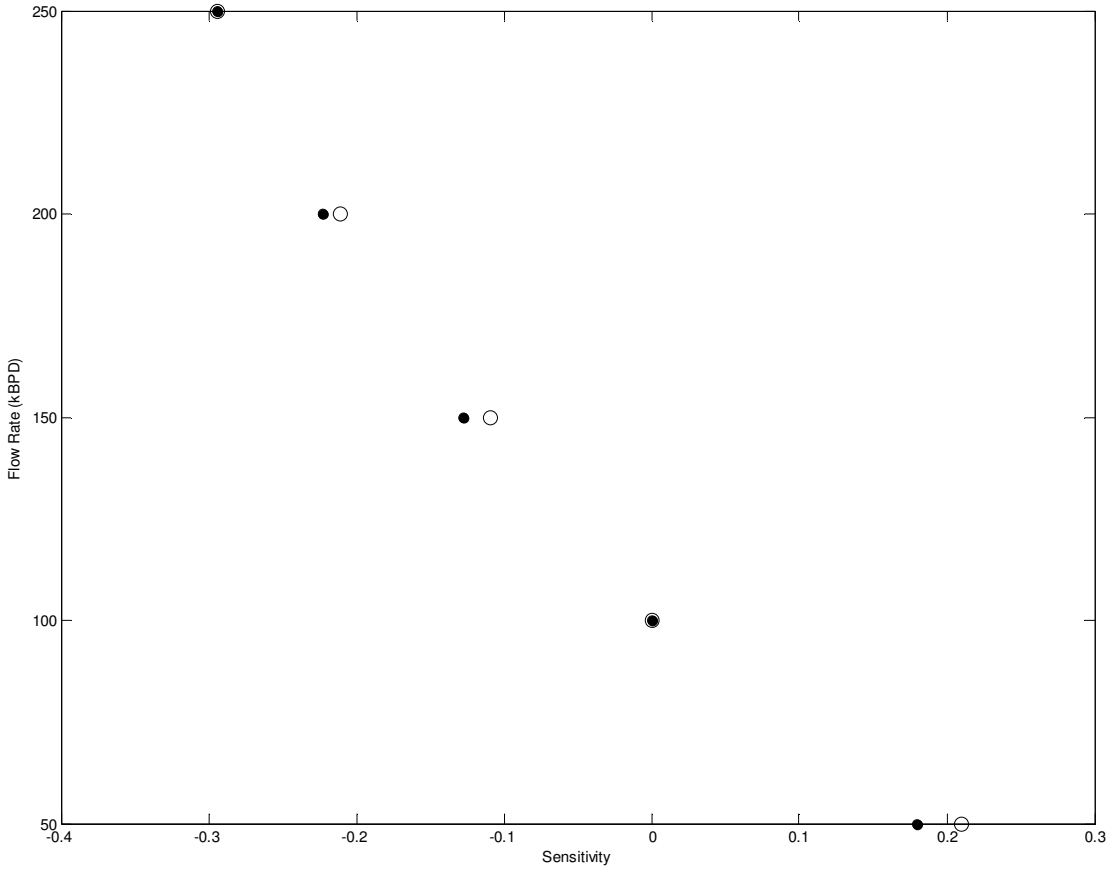

Figure 4.31: Sensitivity of trap height (solid symbols) and non-dimensional trap height (unfilled symbols) for Case 2 with 0.4 mm bubble diameter.

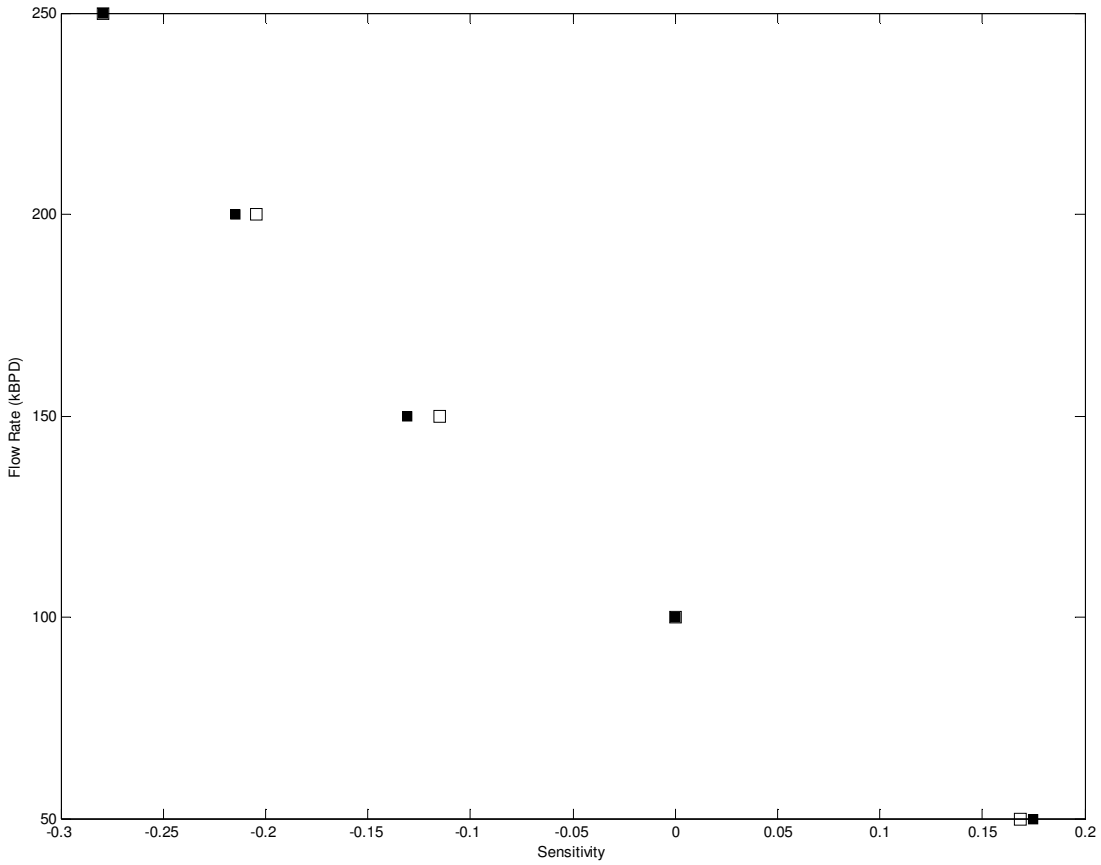

Figure 4.32: Sensitivity of trap height (solid symbols) and non-dimensional trap height (unfilled symbols) for Case 2 with 2 mm bubble diameter.

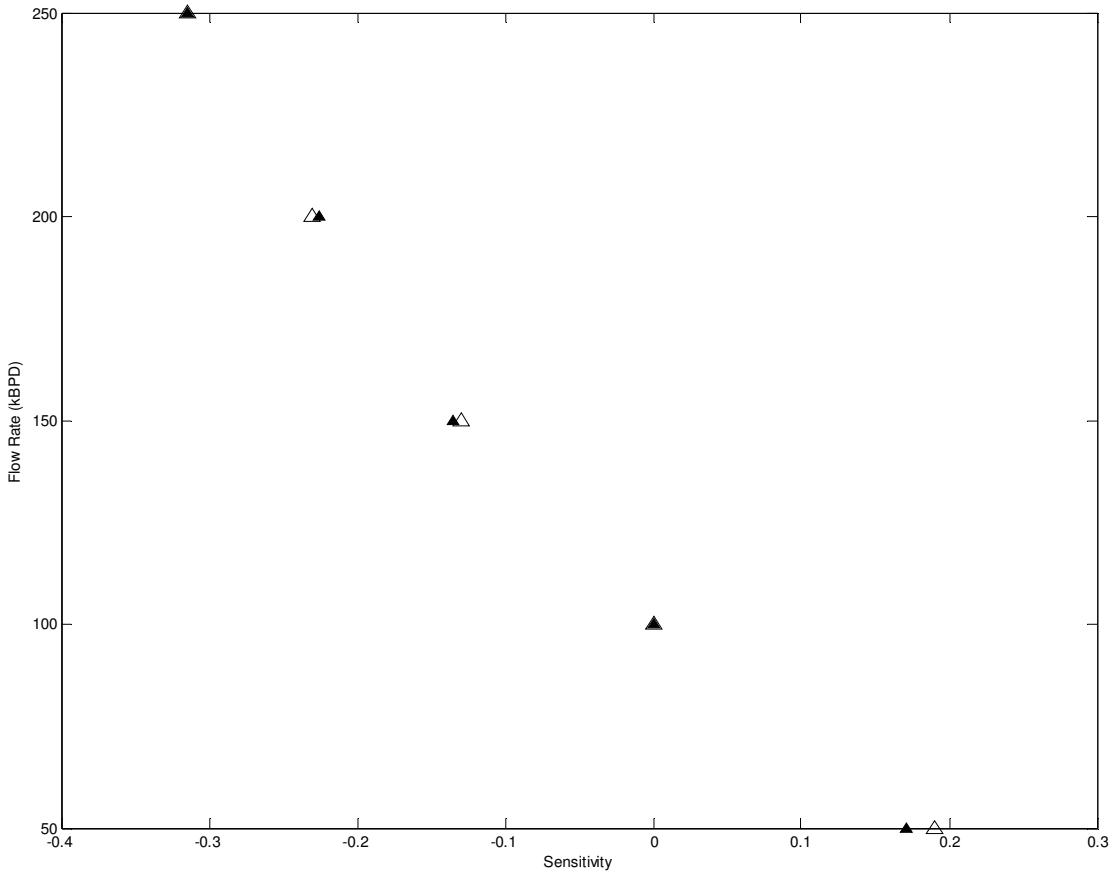

Figure 4.33: Sensitivity of trap height (solid symbols) and non-dimensional trap height (unfilled symbols) for Case 2 with 4 mm bubble diameter.

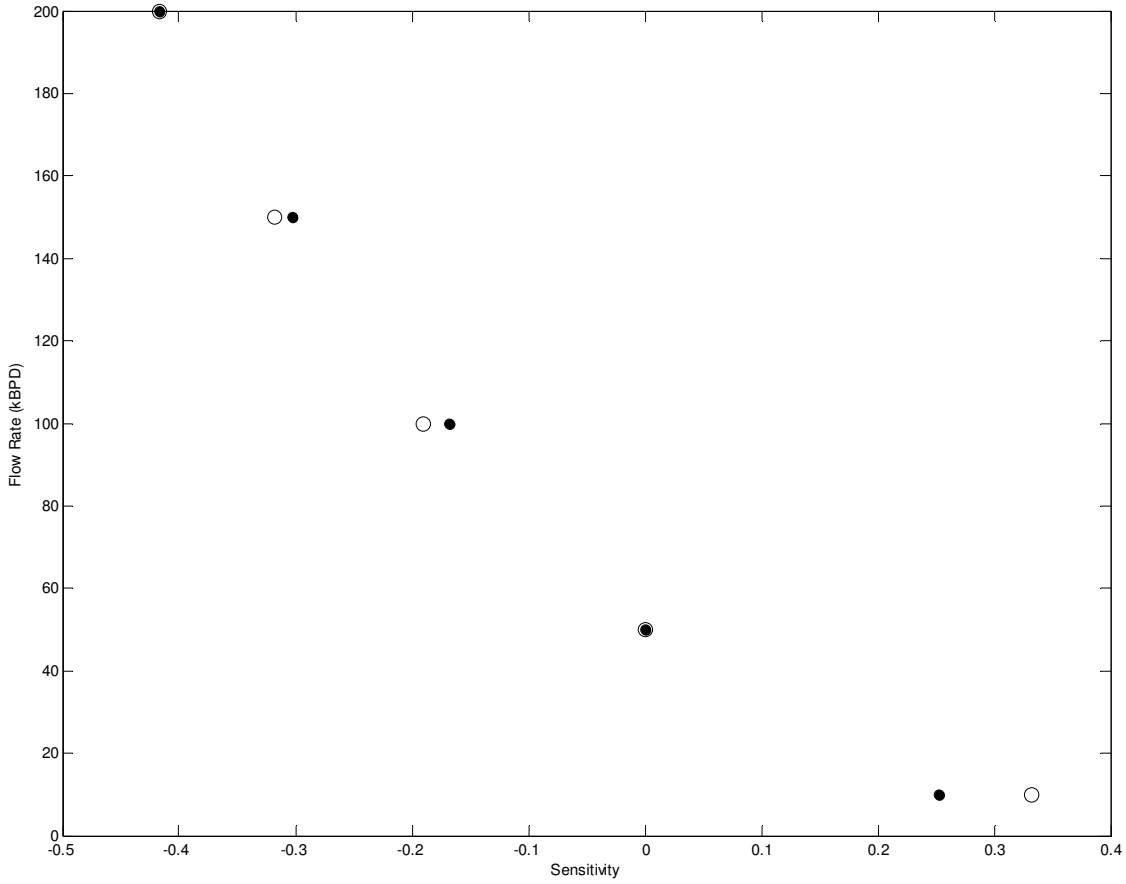

Figure 4.34: Sensitivity of trap height (solid symbols) and non-dimensional trap height (unfilled symbols) for Case 3 with 0.4 mm bubble diameter.

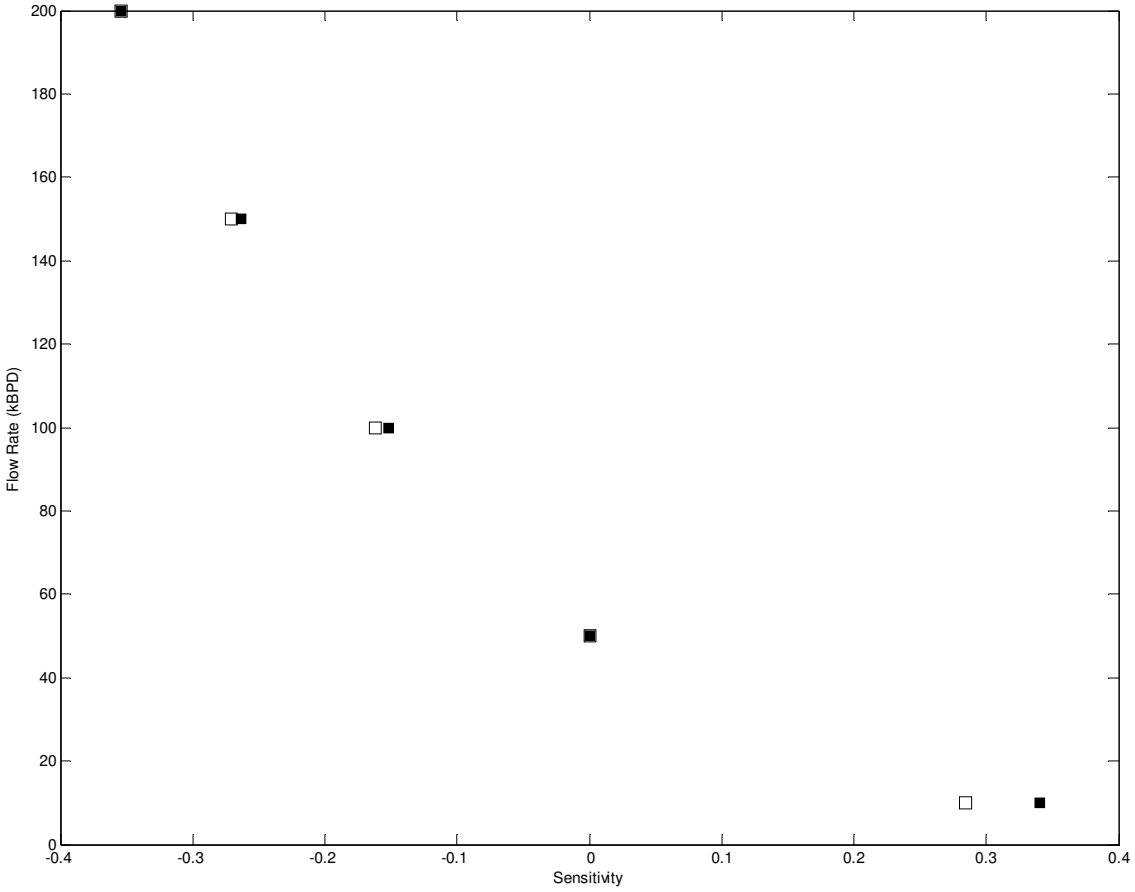

Figure 4.35: Sensitivity of trap height (solid symbols) and non-dimensional trap height (unfilled symbols) for Case 3 with 2 mm bubble diameter.

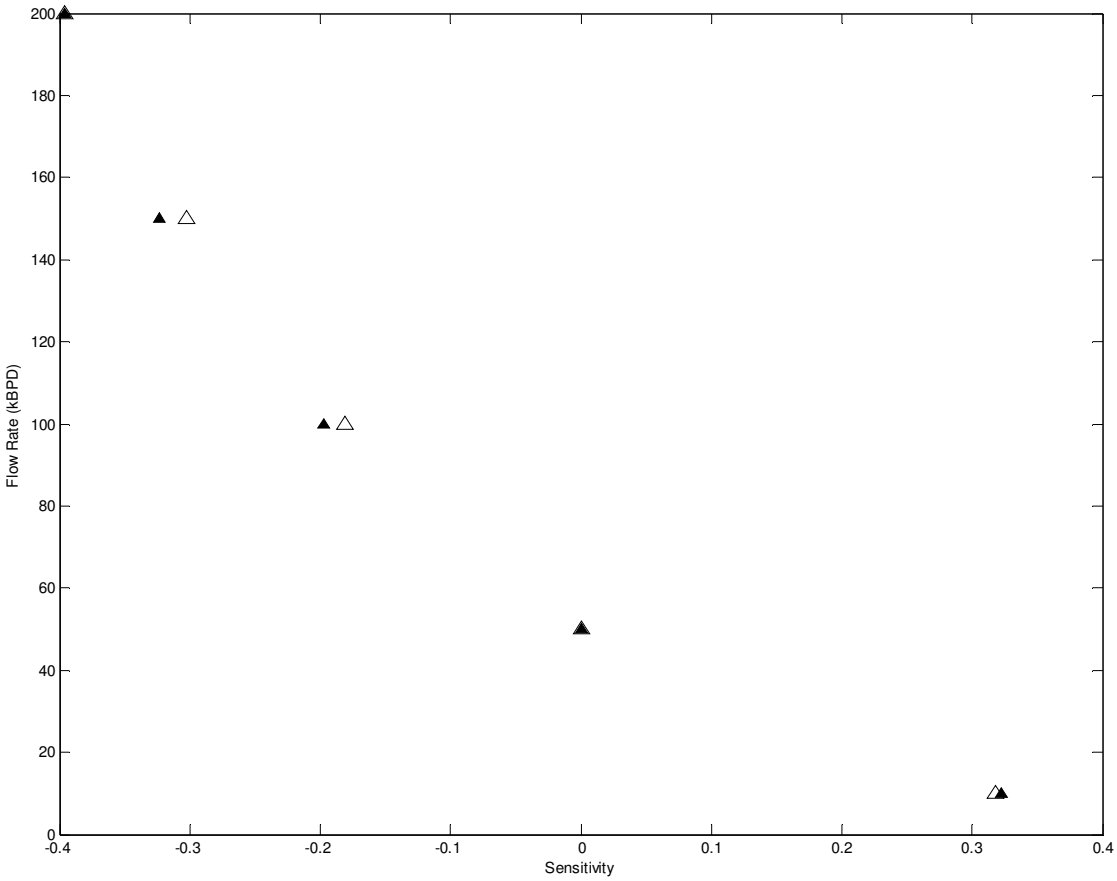

Figure 4.36: Sensitivity of trap height (solid symbols) and non-dimensional trap height (unfilled symbols) for Case 3 with 4 mm bubble diameter.

4.9. Summary of Results

Parameters that may lead to the determination of flow rate were investigated. The purpose is to find a parameter that, when measured in an oil leak, can be compared to model results to determine the flow rate of the leak. It was determined that methane concentration in the intrusion has the best potential to be used in model comparisons. Velocity, plume width, and trap height can be used to corroborate the results, but temperature shows little ability to be used for the purpose of this study. However, it should be noted maximum sensitivity occurs at roughly the same height among different flow rates in most cases, so further research may allow measurements targeted at maximum sensitivity to be conducted that may be appropriate to use in model comparisons.

Non-dimensional comparisons show close correlation between modeled results and non-dimensional variables. This reduces the number of modeling scenarios done when a parameter is measured in an oil leak. One scenario can be used and combined with non-dimensional values to determine an approximate flow rate, and scenarios can be run with an approximate value in mind, thus reducing the time needed to find a solution.

Further research will determine if these parameters can be used with field data to accurately determine flow rate.

5. CONTAINMENT DOME EXPERIMENT

This chapter is included to use laboratory experiments to show a containment dome is operational.

5.1. Set Up

The containment dome used in this experiment was provided by Shell. The dome contains an inlet at the base for an air/oil/entrained water mixture to flow from the riser system at the base of the tank into the dome. The piping set up is shown in Figure 5.1. The oil flow rate was controlled by a valve located between the oil drum and the flow meters. The flow meters were placed over 10 diameters upstream and downstream from any valves or bends in the piping. High capacity and low capacity flow meters were used depending on the flow rate into the system. The flow meters were on separate tracks, each having its own control valve. The air flow rate was controlled and measured using an air mass flow meter. The air and oil were mixed along a length of pipe before exiting the riser system.

Figure 5.2 shows the tank dimensions and the adjusted directions for the experiment.

Figure 5.3 shows the operation of the containment dome. A gas/oil/water mixture flows in the center of the base of the dome. As the mixture flows upward the oil is siphoned off

the top and the remaining sea water flows from the outlets in the bottom. The important dimension for this study is the inlet diameter which was 16 cm.

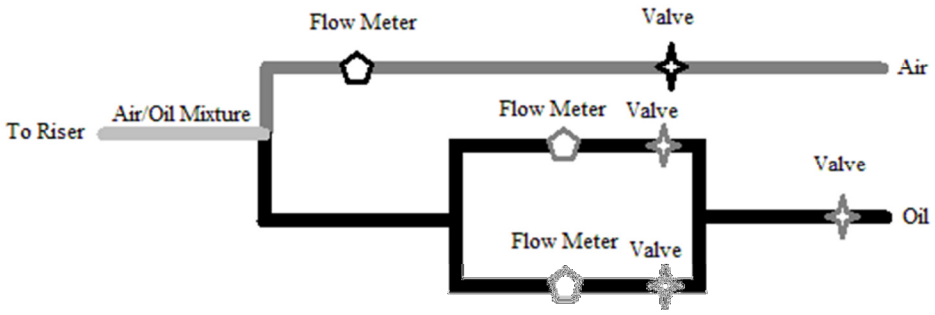

Figure 5.1: Piping set up for the experiment. Air and oil intakes are on the right and the air/oil mixture outlet is on the left.

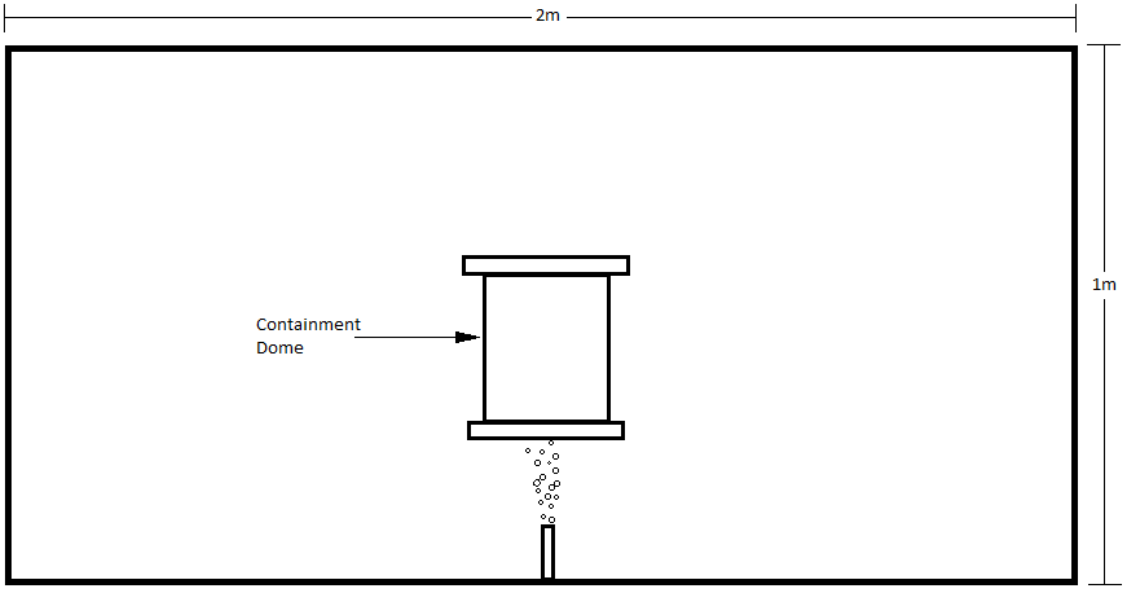

Figure 5.2: Experimental set up with tank dimensions.

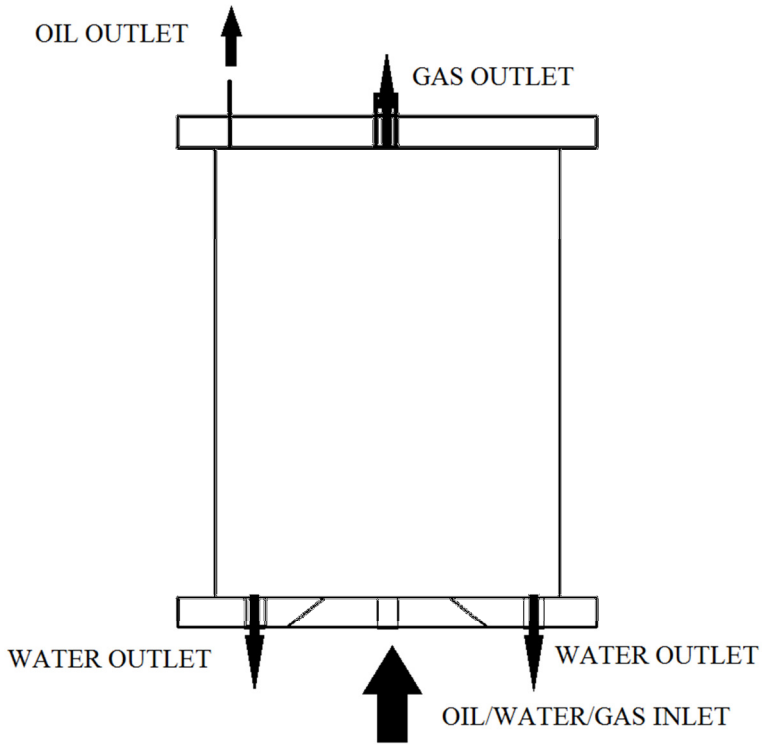

Figure 5.3: Containment dome with flow arrows.

5.2. Results

Table 5.1 shows the operating conditions of the containment dome.

Table 5.1: Laboratory conditions.

		Optimal Position
Position	Vertical (cm)	2.5
	Horizontal (cm)	0
	Rotational (degrees)	0
Flow rates	Oil in (liters/minute)	2.08
	Air in (liters/minute)	45
	Oil/Water out (liters/minute)	2.02

5.3. Scaling and Prototype Conditions

Gravitational and inertial forces were determined to be dominant in this situation. Froude scaling

$$Fr = \frac{U}{\sqrt{gL}} \tag{4.1}$$

where Fr is the Froude number, U is the characteristic velocity, and L is the characteristic length, was used to geometrically scale both the containment dome and the riser system. Velocity scaling was achieved using

$$\frac{U_P}{U_M} = \sqrt{\frac{g_P\left(1-\frac{\rho_g}{\rho_l}\right)_P L_P}{g_M\left(1-\frac{\rho_g}{\rho_l}\right)_M L_M}} \tag{4.2}$$

where subscripts P and M represent prototype and model respectively, ρ_g is the gas density, and ρ_l is the liquid density. Gas density is found through

$$\rho_g = \frac{M_g P_g}{R_g T_g} \tag{4.3}$$

where M_g is the molar mass, P_g is the pressure, R_g is the universal gas constant, and T_g is the temperature. Since the ratio of prototype and model gravities and density ratios are negligible, Equation (4.2) reduces to

$$\frac{U_P}{U_M} = \left(\frac{L_P}{L_M}\right)^{0.5} \tag{4.4}$$

which leads to

$$\frac{Q_P}{Q_M} = \frac{U_P A_P}{U_M A_M} = \left(\frac{L_P}{L_M} \right)^{2.5} \tag{4.5}$$

where A is the area of the orifice. The length scale is given as 1:20. The flow rates are approximately scaled in Table 5.2.

Table 5.2: Prototype values for failure conditions.

		Optimal Position
Position	Vertical (m)	0.5
	Horizontal (m)	0
	Rotational (degrees)	0
Flow rates	Oil in (bbl/day)	34
	Air in (liters/minute)	80000
	Oil/Water out (bbl/day)	33

The prototype dome inlet dimensions are 3.2 m funneling to 1 m, and the riser diameter is 31 cm. These inlet and riser dimensions will be used in numerically modeling the limits in Section 5.4.

5.4. Predictions Using Integral Model

This model was numerically tested at a depth of 30.5 m with the values given in Table 3.1. The oil and gas temperature was set to 53°C. The true plume width was found 3 standard deviations away from the center where the standard deviation is given as

$$\sigma = \frac{\sqrt{2}\lambda_2 Q_i}{\sqrt{\pi M_i}} \tag{4.6}$$

where λ_2 is taken as 1.2. The results for conditions are shown in Figure 5.4. The unfilled square represents the experimental condition. The test condition must be more restrictive to show preference to initial condition.

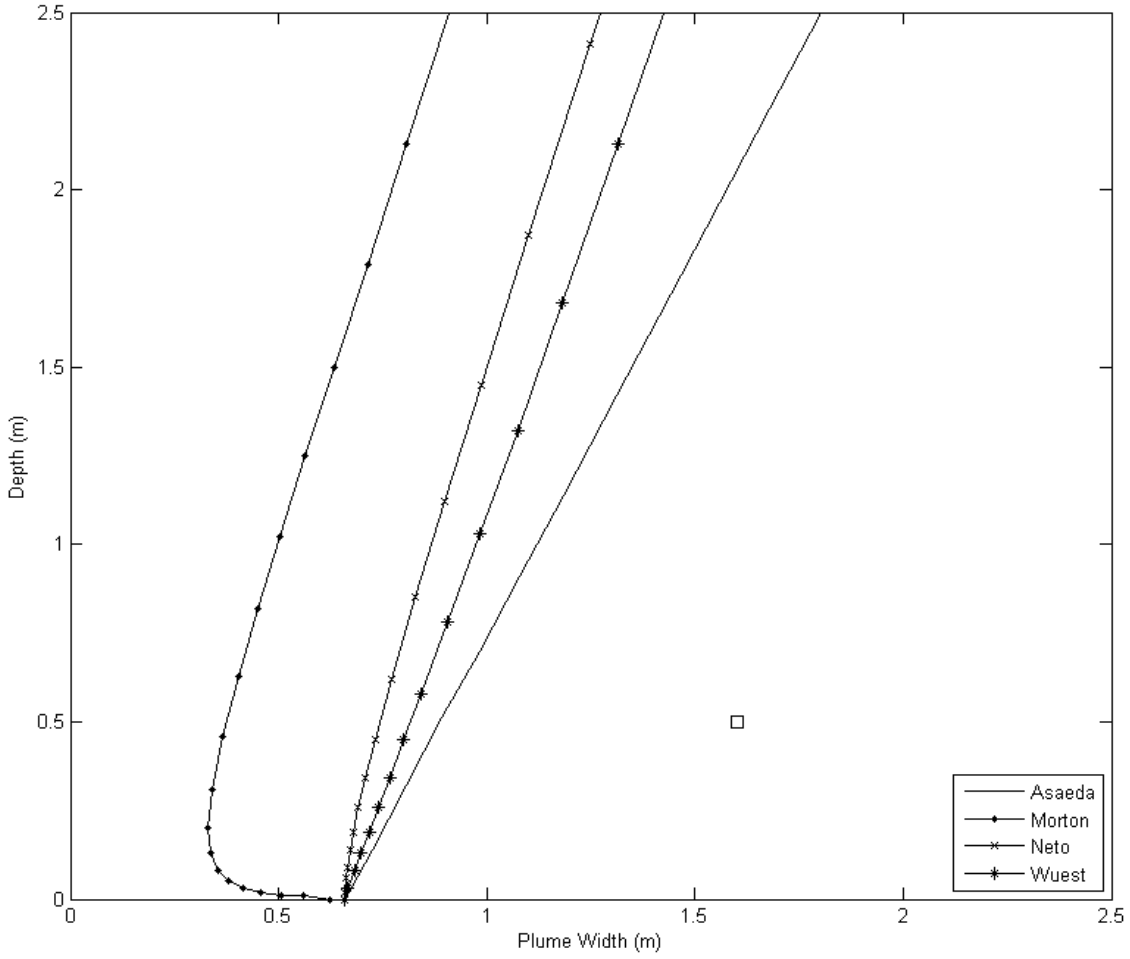

Figure 5.4: Results using Asaeda, Morton, Neto, and Wüest initial conditions. Experimental condition is given as unfilled square.

6. SUMMARY AND CONCLUSIONS

There has been much advancement in integral modeling techniques; these advancements were combined into the SIMP modeling program which was used to draw conclusions related to deep water oil well blow outs.

Initial conditions were compared and found to converge with shallow water depths. The comparison was made to a base case. The Neto initial conditions are found to vary further from the values given by the Asaeda, Wüest, and Morton initial conditions. The most accurate of the initial conditions is unable to be determined with numerical modeling alone. Future analysis of experimental modeling can be used to determine the most accurate initial condition for a variety of scenarios.

Analysis was done on several parameters to determine sensitivity to flow rate. Temperature and plume width show little sensitivity to changes in flow rate, but centerline velocity and trap height show moderate sensitivity. The largest sensitivity was found for methane concentration in the first intrusion. All of these parameters are easily measured from the ROV being used to investigate a blowout. All parameters can be used in conjunction to determine flow rate using integral modeling. It was also found that non-dimensional equations can be used to predict sensitivity for trap height and

centerline velocity. Future research in the field can be used to determine the validity of these parameters as adequate to determine flow rate.

The containment dome was shown to be operational.

REFERENCES

Anderson, K., Bhatnager, G., Crosby, D., Hatton, G., Manfield, P., Kuzmicki, A., et al. (2012). "Hydrates in the Ocean Beneath, Around, and Above Production Equipment". *Energy & Fuels, 26*(7), 4167-4176.

Asaeda, T., & Imberger, J. (1993). "Structure of Bubble Plumes in Linearly Stratified Environments". *Journal of Fluid Mechanics, 249*, 35-57.

Bombardelli, F. A., Buscaglia, G. C., Rehmann, C. R., Rincon, L. E., & Garcia, M. H. (2007). "Modeling and Scaling of Aeration Bubble Plumes: A Two-Phase Flow Analysis". *Journal of Hydraulic Research, 45*(5), 617-630.

Chen, C. J., & Nikitopoulos, C. P. (1979). "On the Near Field Characteristics of Axisymmetric Turbulent Buoyant Jets in a Uniform Environment". *International Journal of Heat and Mass Transfer, 22*, 245-255.

Clift, R., Grace, J. R., & Weber, M. E. (1978). *"Bubbles, Drops and Particles".* New York, New York: Academic Press.

Crounse, B. C. (2000, June). *"Modeling Buoyant Droplet Plumes in a Stratified Environment". Ph.D Thesis.* Massachusetts Institute of Technology, Cambridge, MA.

Crounse, B. C., Wannamaker, E. J., & Adams, E. E. (2007). "Integral Model of a Multiphase Plume in Quiescent Stratification". *Journal of Hydraulic Engineering, 133*(1), 70-75.

EPA. (1999, December). *Emergency Management.* Retrieved May 25, 2013, from U.S. Environmental Protection Agency: http://www.epa.gov/osweroe1/content/learning/pdfbook.htm

Gill, A. (1982). *"Ocean-Atmosphere Dynamics".* New York, NY: Academic Press.

Henderson-Sellers, B. (1983). "The Zone of Flow Establishment for Plumes with Significant Buoyancy". *Applied Mathmatics in Modelling, 7*, 395-398.

McDougall, T. J. (1977). "Bubble Plumes in Stratified Environments". *Journal of Fluid Mechanics, 85*(4), 655-672.

Milgram, J. H. (1983). "Mean Flow in Round Bubble Plumes". *Journal of Fluid Mechanics, 133*, 345-376.

Morton, B. R., Taylor, G., & Turner, J. S. (1956). "Turbulent Gravitational Convection from Maintained and Instantaneous Sources". *Proceedings of the Royal Society A: Mathematical, Physical and Engineering Sciences, 234*(1196), 1-23.

Mustang Engineering. (2012). *"2012 Deepwater Solutions & Records for Concept Selection".* Retrieved October 29, 2012, from Wood Group Mustang: http://www.mustangeng.com/AboutMustang/Publications/Publications/Deepwater%20Poster%20Final.pdf

Neto, I. E. (2012). "Modeling the Liquid Volume Flux in Bubbly Jets Using a Simple Integral Approach". *Journal of Hydraulic Engineering, 138*(2), 210-215.

Ranz, W., & Marshall, W. (1952). "Evaporation from Drops". *Chem. Eng. Prog., 48*(3), 141-146.

Socolofsky, S. A., & Adams, E. E. (2005). "Role of Slip Velocity in the Behavior of Stratified Multiphase Plumes". *Journal of Hydraulic Engineering, 131*(4), 273-282.

Socolofsky, S. A., & Bhaumik, T. (2008). "Dissolution of Direct Ocean Carbon Sequestration Plumes Using an Integral Model Approach". *Journal of Hydraulic Engineering, 134*(11), 1570-1578.

Socolofsky, S. A., Bhaumik, T., & Seol, D.-G. (2008). "Double-Plume Integral Models for Near-Field Mixing in Multiphase Plumes". *Journal of Hydraulic Engineering, 134*(6), 772-783.

Wüest, A., Brooks, N. H., & Imboden, D. M. (1992). "Bubble plume modeling for lake restoration". *Water Resources Research, 28*(12), 3235-3250.

APPENDIX A

A.1 Sea water equation of state

This is the sea water equation of state used in the integral model (Gill, 1982). It calculates salt water density, ρ_{sw}, in kg/m^3 using temperature, T, in degrees Celcius; salinity, S, in PSU; and pressure, P, in bars.

At standard atmosphere (P = 0):

$$\begin{aligned}
\rho_{sw}(S,T,0) = \quad & 999.842594 && +6.793952\times10^{-2}T \\
& -9.095290\times10^{-3}T^2 && +1.001685\times10^{-4}T^3 && -1.120083\times10^{-6}T^4 \\
& +6.536332\times10^{-9}T^5 && +8.24493\times10^{-1}S && -5.72466\times10^{-3}S^{3/2} \\
& +4.8314\times10^{-4}S^2 && -4.0899\times10^{-3}TS && +7.6438\times10^{-5}T^2S \\
& -8.2467\times10^{-7}T^3S && +5.3875\times10^{-9}T^4S && +1.0227\times10^{-4}TS^{3/2} \\
& -1.6546\times10^{-6}T^2S^{3/2}
\end{aligned} \tag{7.1}$$

Under pressure:

$$\rho_{sw}(S,T,P) = \frac{\rho_{sw}(S,T,0)}{1-\dfrac{P}{K(S,T,P)}} \tag{7.2}$$

where

$$
\begin{aligned}
K(S,T,P) = \quad & 19652.21 && +148.4206T \\
& -2.327105T^2 && +1.360477\times10^{-2}T^3 && -5.155288\times10^{-5}T^4 \\
& +3.239908P && +1.43713\times10^{-3}TP && +1.16092\times10^{-4}T^2P \\
& -5.77905\times10^{-7}T^3P && +8.50935\times10^{-5}P^2 && -6.12293\times10^{-6}TP^2 \\
& +5.2787\times10^{-8}T^2P^2 && +54.6746S && -0.603459TS \\
& +1.09987\times10^{-2}T^2S && -6.1670\times10^{-5}T^3S && +7.944\times10^{-2}S^{3/2} \\
& +1.6483\times10^{-2}TS^{3/2} && -5.3009\times10^{-4}T^2S^{3/2} && +2.2838\times10^{-3}PS \\
& -1.0981\times10^{-5}TPS && -1.6078\times10^{-6}T^2PS && +1.91075\times10^{-4}PS^{3/2} \\
& -9.9348\times10^{-7}P^2S && +2.0816\times10^{-8}TP^2S && +9.1697\times10^{-10}T^2P^2S
\end{aligned}
\tag{7.3}
$$

A.2 Plots for Sensitivity Analysis

These figures represent the results from which the figures in Section 4 were calculated.

A.2.1 Case 1, Depth: 1829 m, Bubble Diameter: 0.4 mm

This case applies to Figure A.1 through Figure A.5.

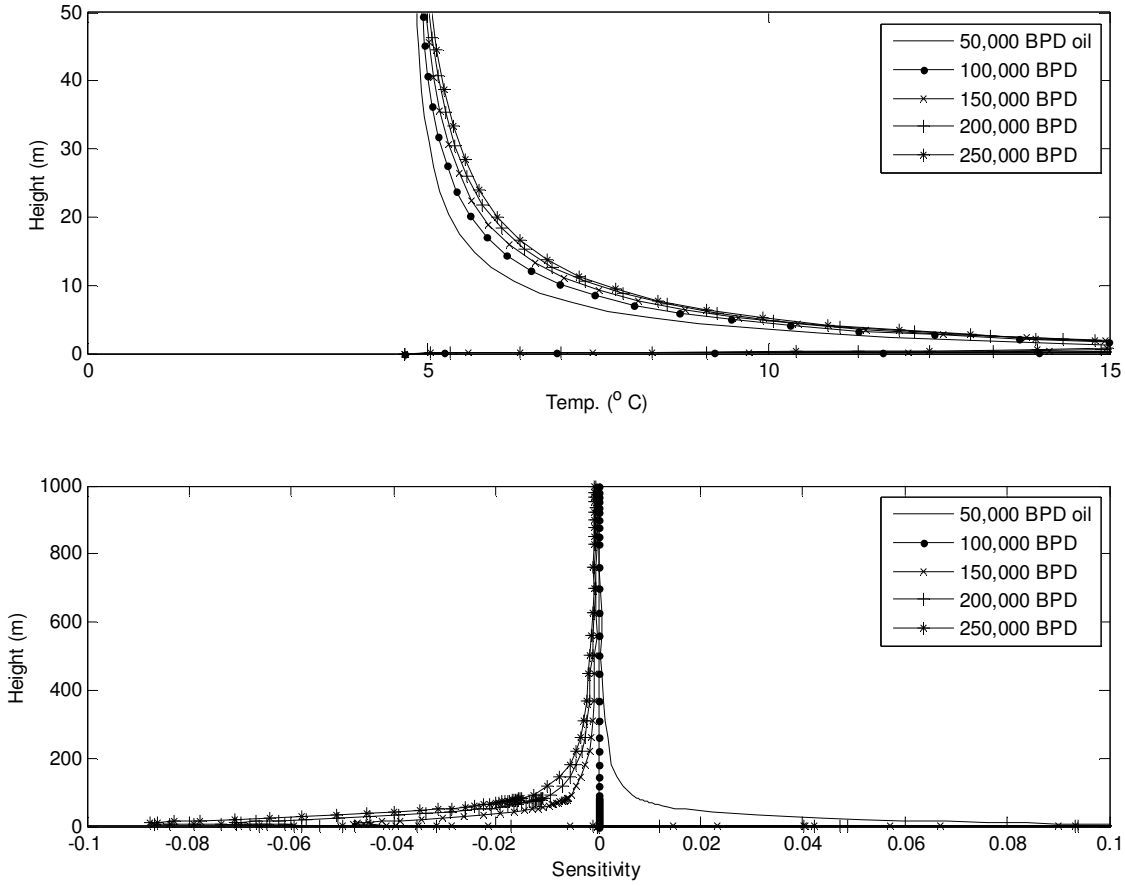

Figure A.1: Top: Raw data for inner plume temperature at a series of flow rates. Bottom: Sensitivity analysis of the temperature at the same flow rates. 100,000 BPD is used as the reference.

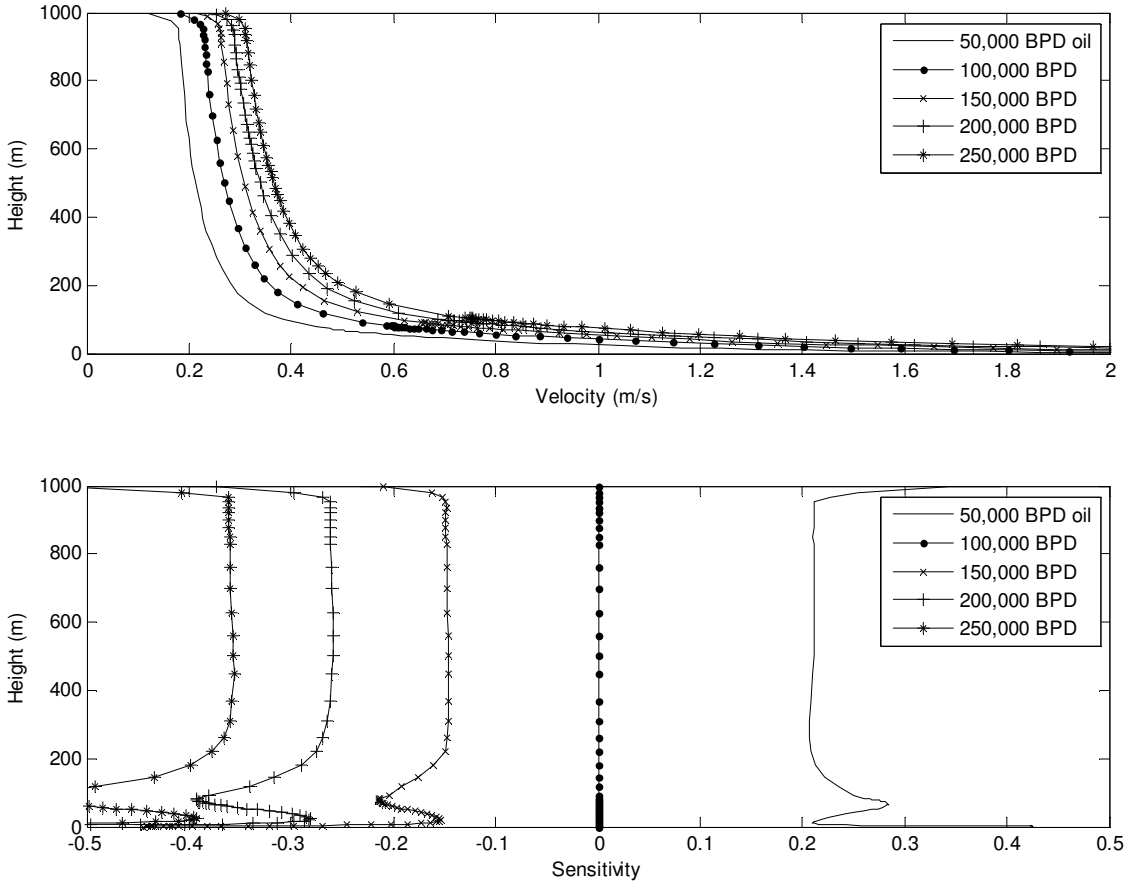

Figure A.2: Top: Raw data for inner plume mean velocity at a series of flow rates. Bottom: Sensitivity analysis of the mean velocity at the same flow rates. 100,000 BPD is used as the reference.

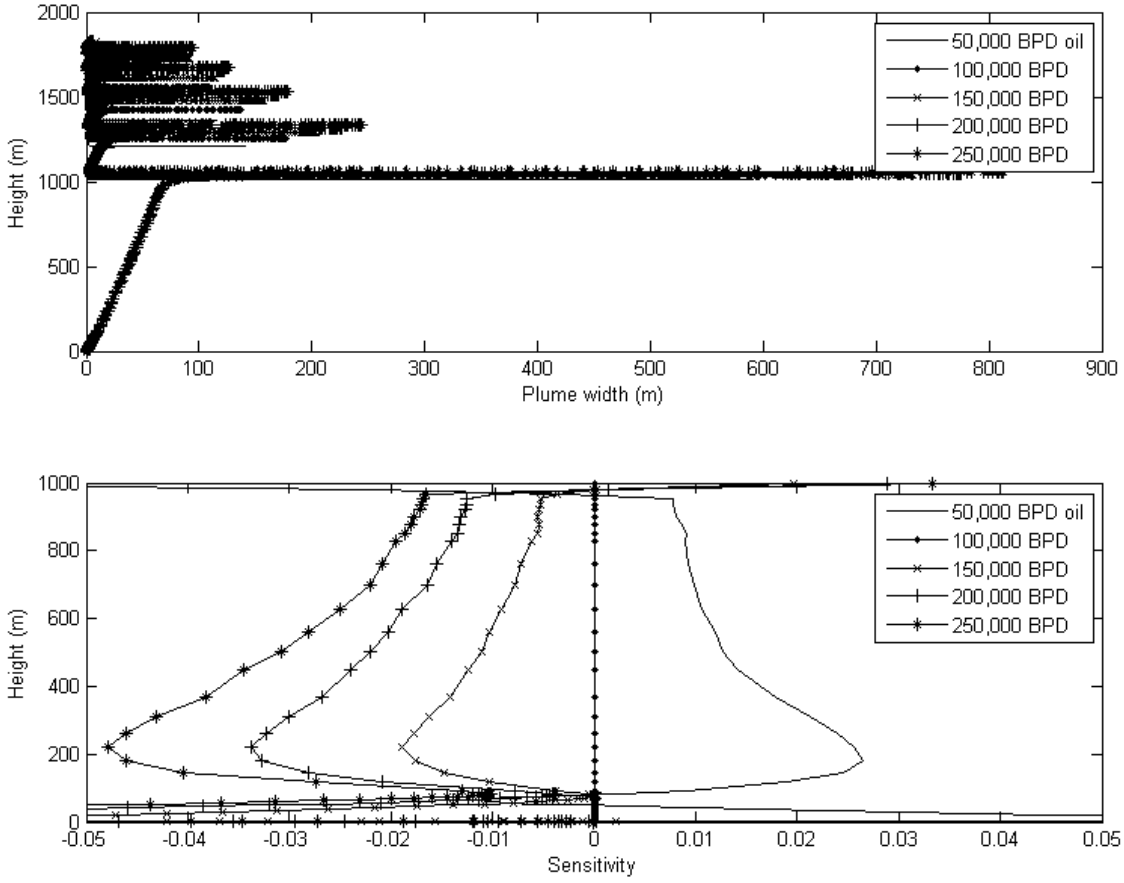

Figure A.3: Top: Raw data for inner plume width at a series of flow rates. Bottom: Sensitivity analysis of the width at the same flow rates. 100,000 BPD is used as the reference.

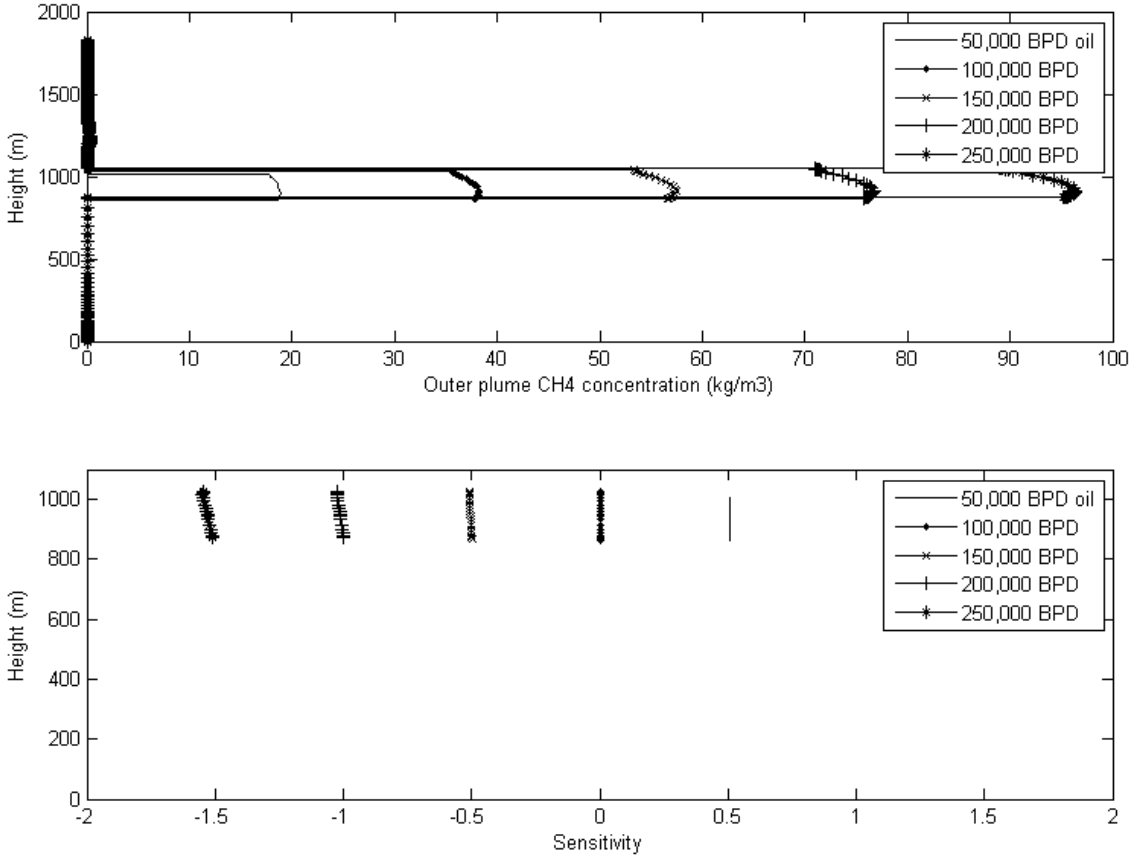

Figure A.4: Top: Raw data for outer plume CH_4 concentration at a series of flow rates. Bottom: Sensitivity analysis of the CH_4 at the same flow rates. 100,000 BPD is used as the reference.

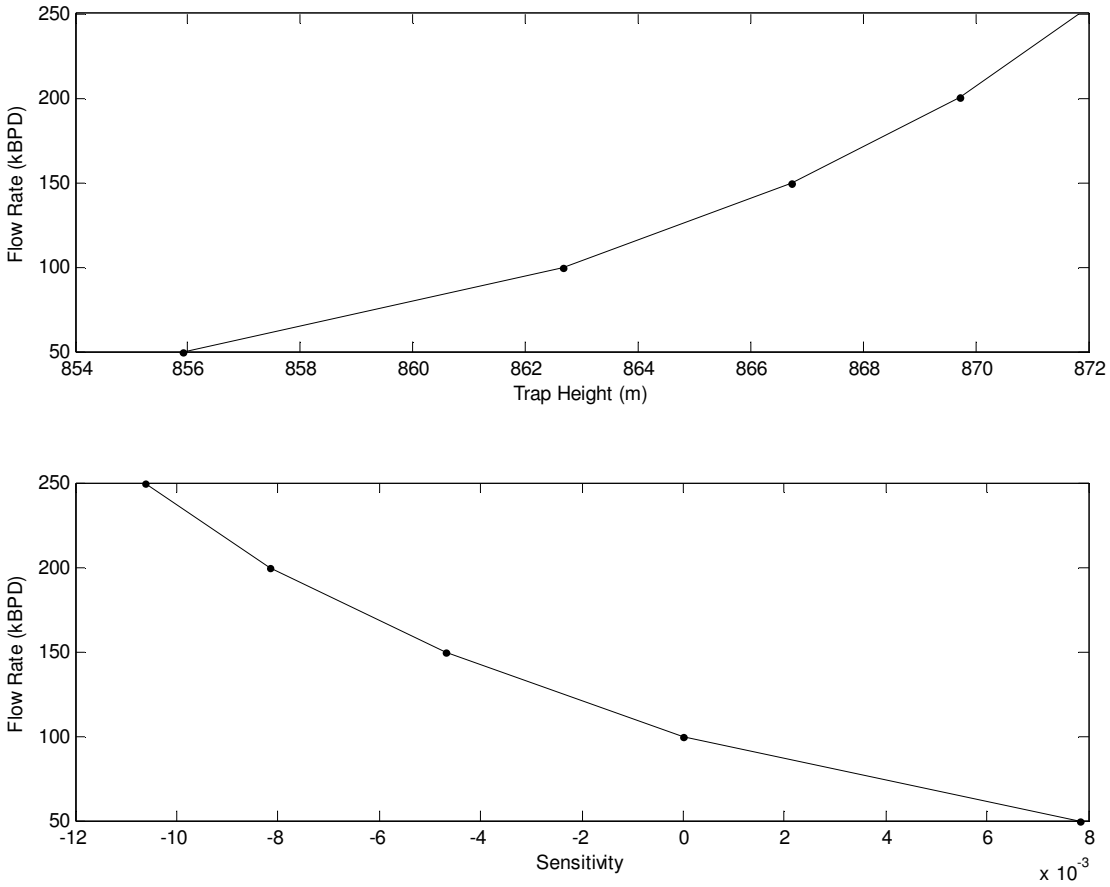

Figure A.5: Top: Trap height for the outer plume with respect to flow rate. Bottom: Sensitivity in relation to flow rate with 100,000 BPD used as the reference value.

A.2.2 Case 2, Depth: 3000 m, Bubble Diameter: 0.4 mm

This case applies to Figure A.6 through Figure A.10.

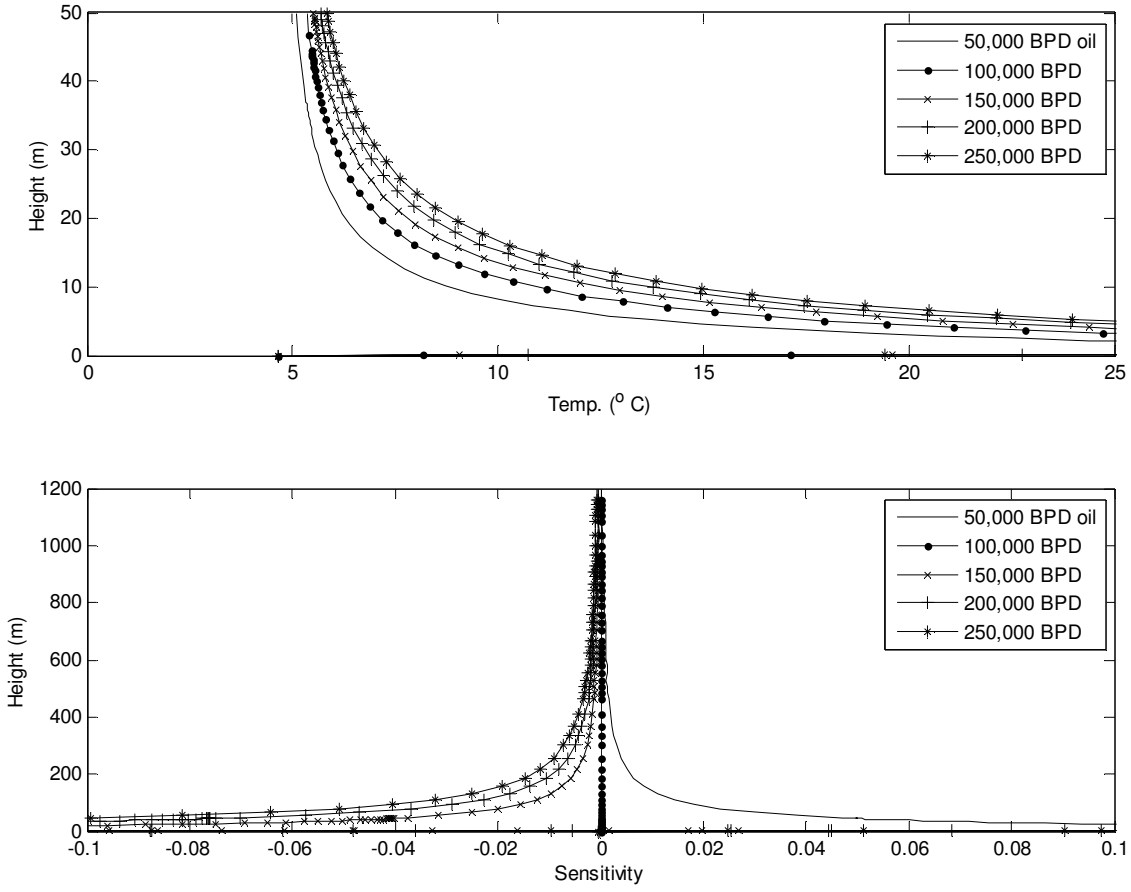

Figure A.6: Top: Raw data for inner plume temperature at a series of flow rates. Bottom: Sensitivity analysis of the temperature at the same flow rates. 100,000 BPD is used as the reference.

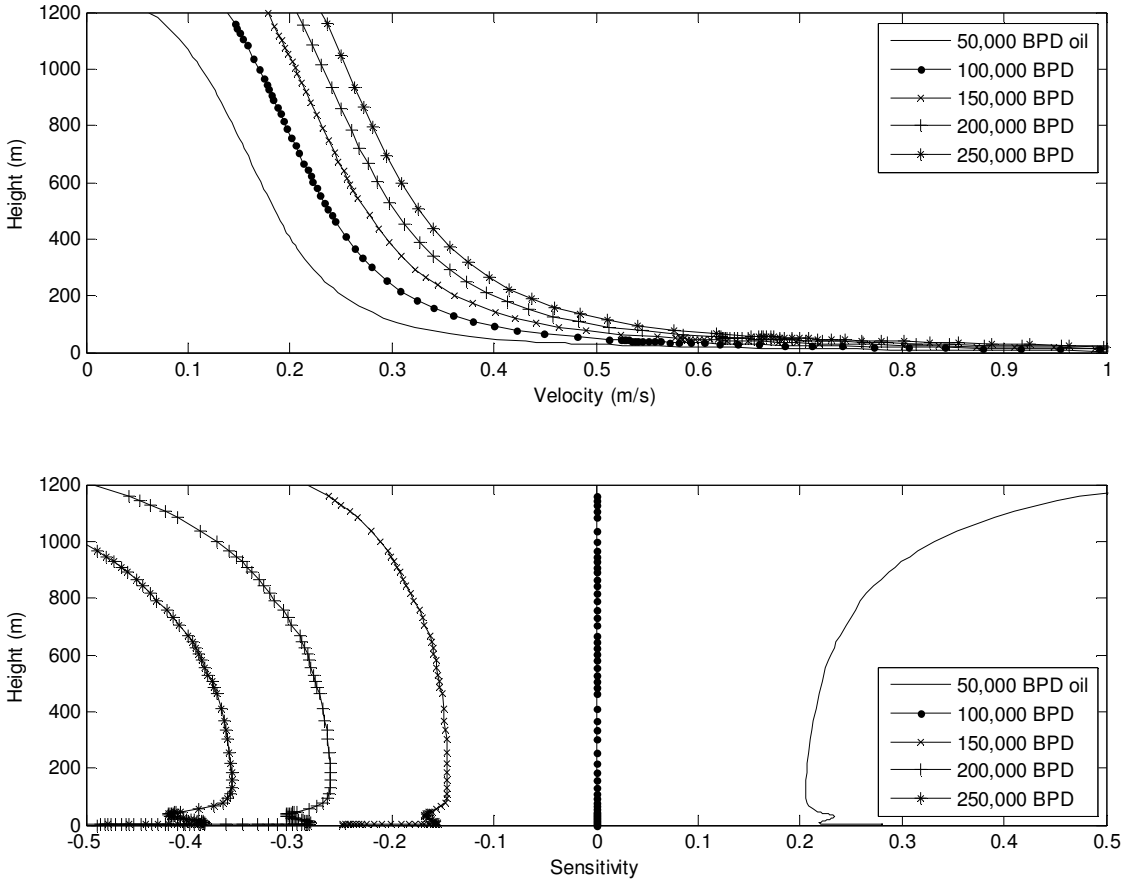

Figure A.7: Top: Raw data for inner plume mean velocity at a series of flow rates. Bottom: Sensitivity analysis of the mean velocity at the same flow rates. 100,000 BPD is used as the reference.

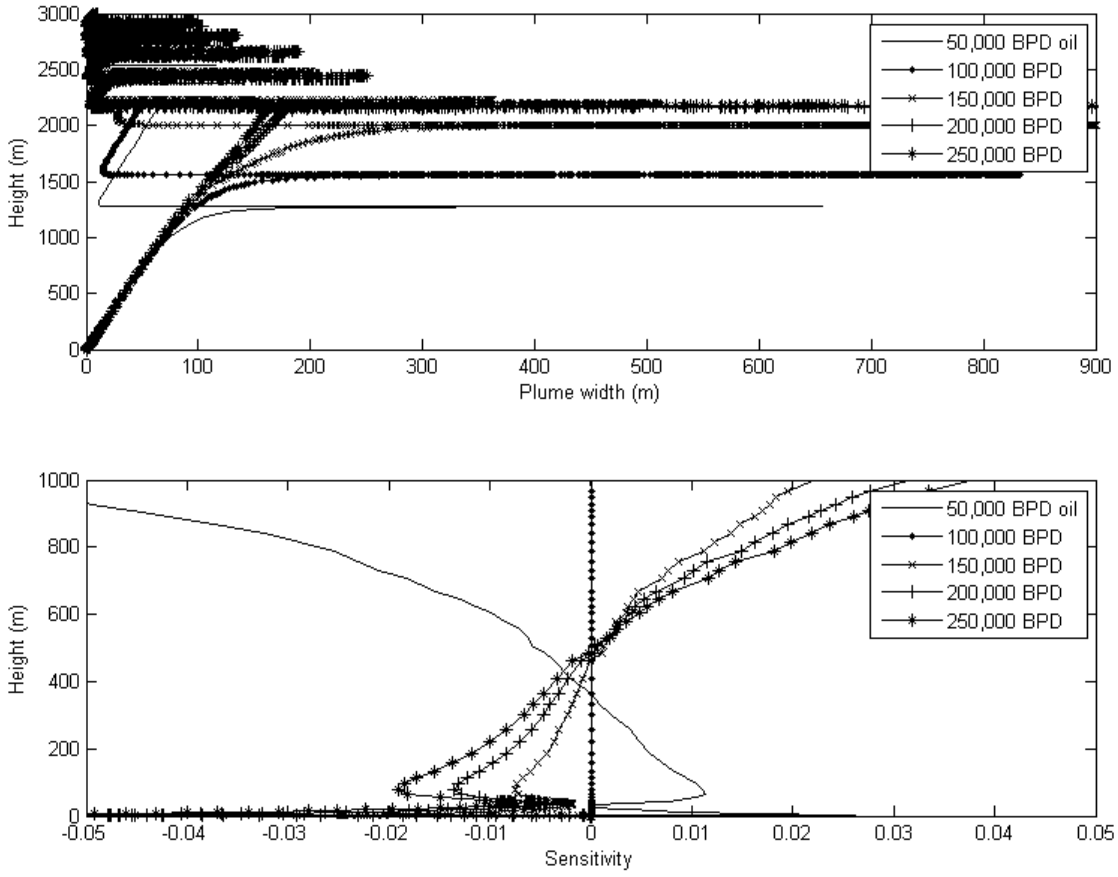

Figure A.8: Top: Raw data for inner plume width at a series of flow rates. Bottom: Sensitivity analysis of the width at the same flow rates. 100,000 BPD is used as the reference.

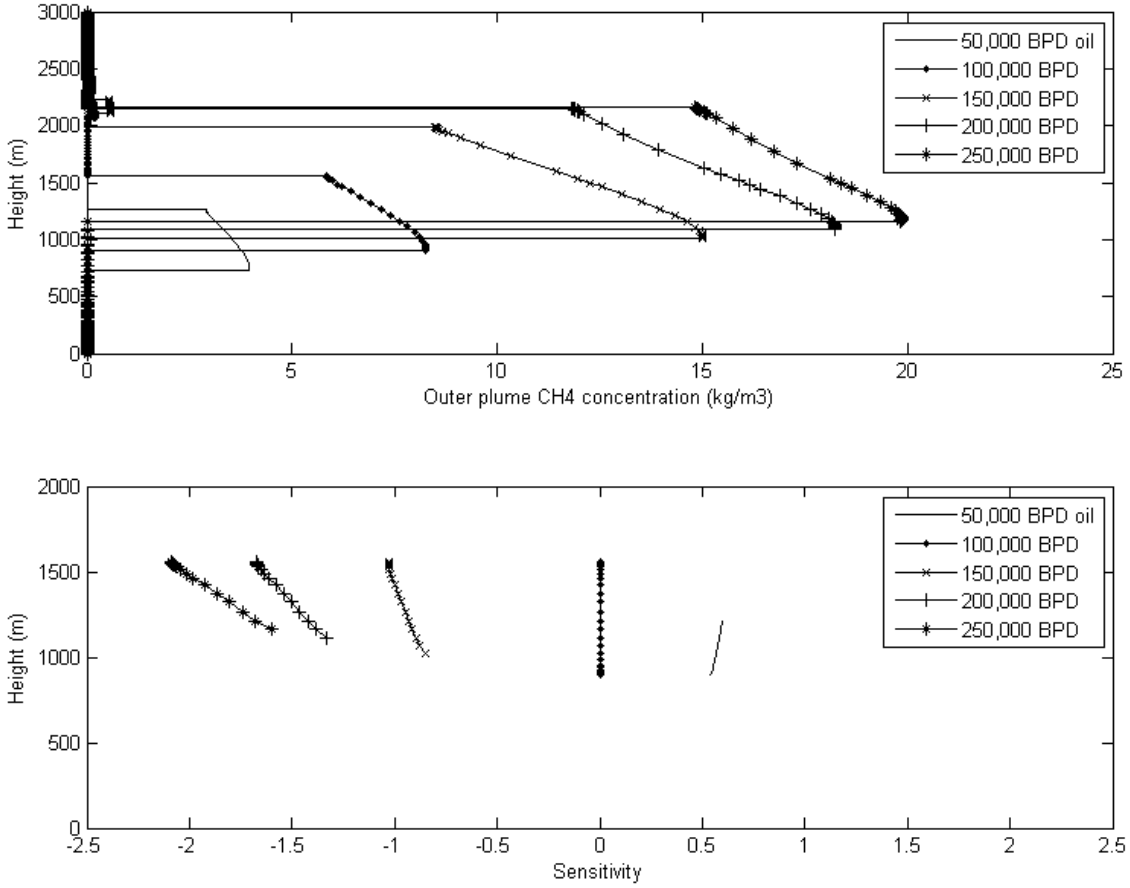

Figure A.9: Top: Raw data for outer plume CH4 concentration at a series of flow rates. Bottom: Sensitivity analysis of the CH4 at the same flow rates. 100,000 BPD is used as the reference.

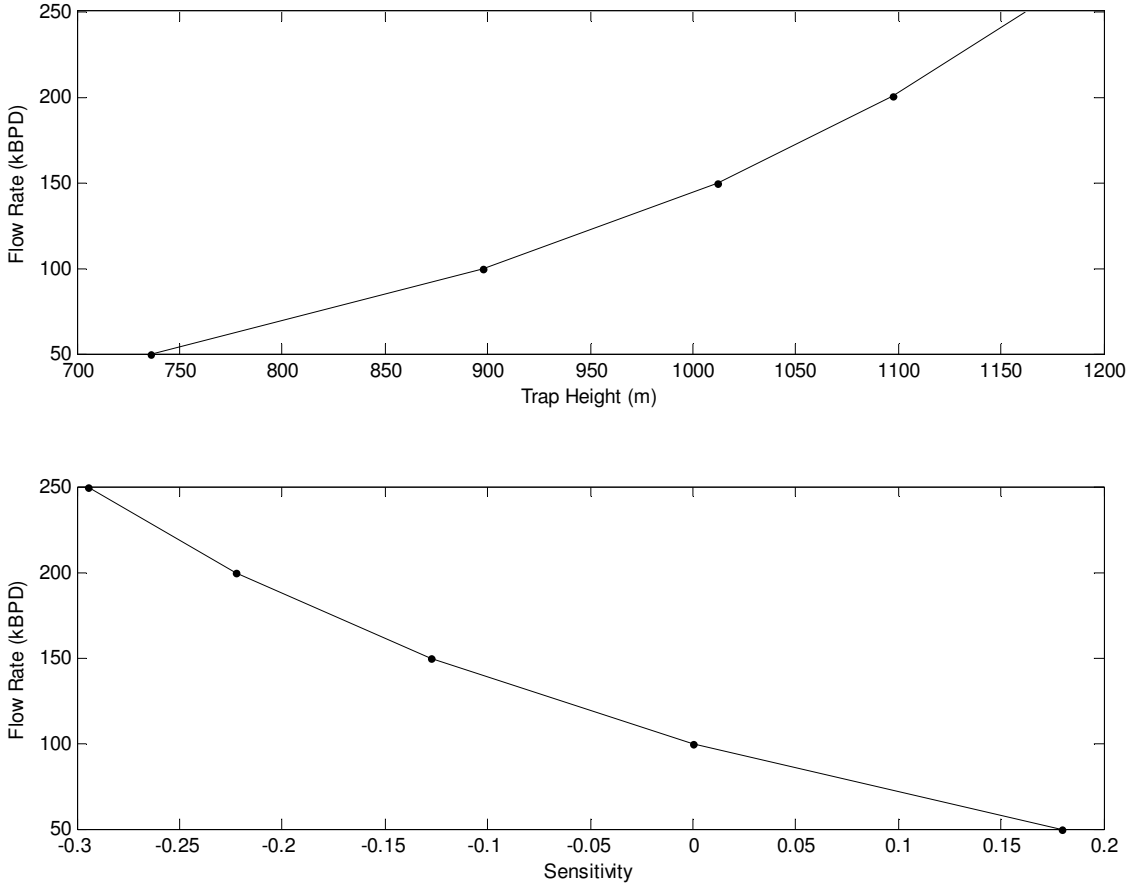

Figure A.10: Top: Trap height for the outer plume with respect to flow rate. Bottom: Sensitivity in relation to flow rate with 100,000 BPD used as the reference value.

A.2.3 Case 3, Depth: 914 m, Bubble Diameter: 0.4 mm

This case applies to Figure A.11 through Figure A.15.

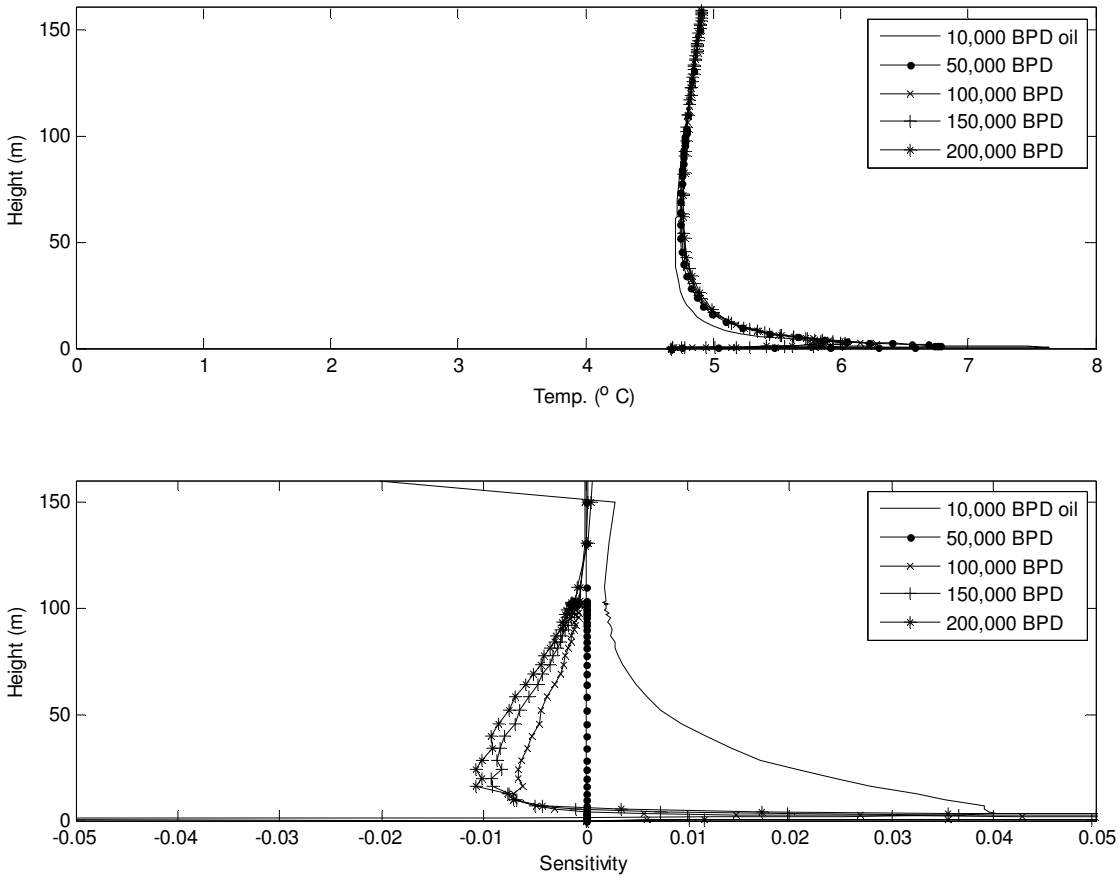

Figure A.11: Top: Raw data for inner plume temperature at a series of flow rates. Bottom: Sensitivity analysis of the temperature at the same flow rates. 50,000 BPD is used as the reference.

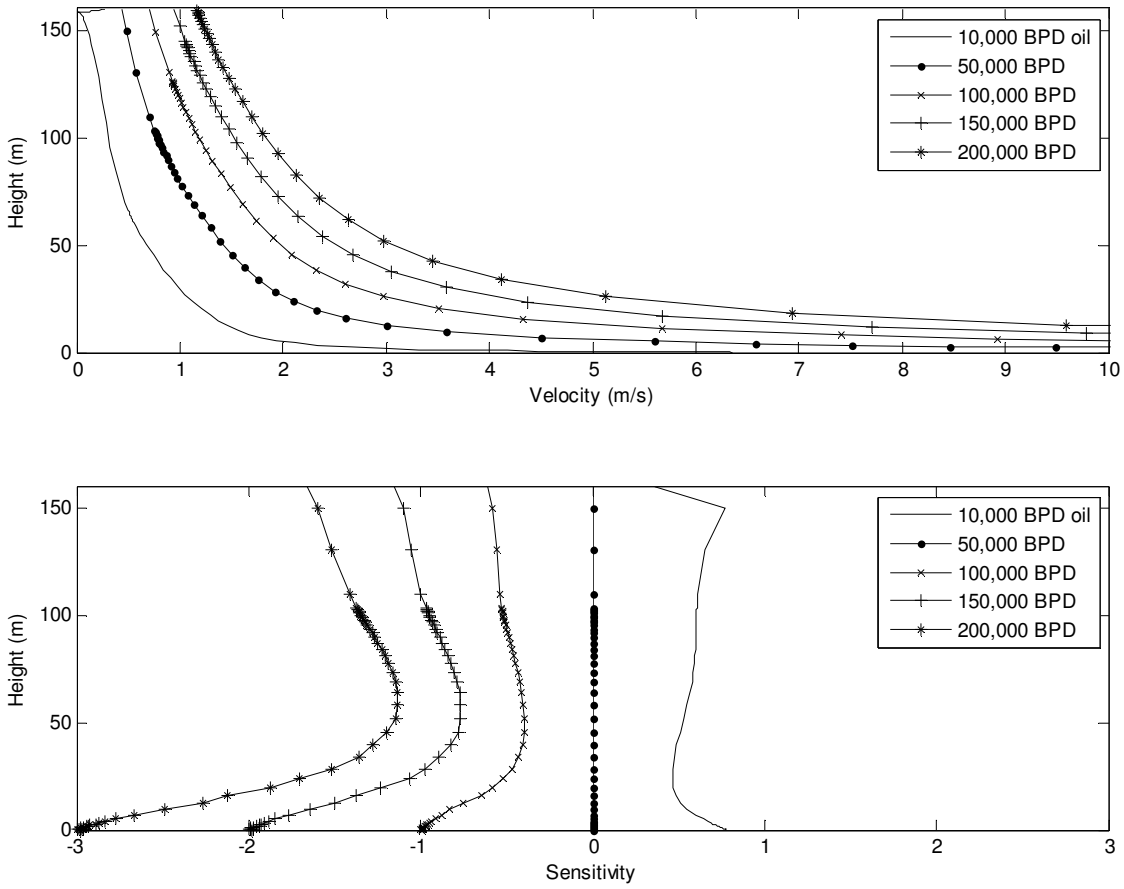

Figure A.12: Top: Raw data for inner plume mean velocity at a series of flow rates. Bottom: Sensitivity analysis of the mean velocity at the same flow rates. 50,000 BPD is used as the reference.

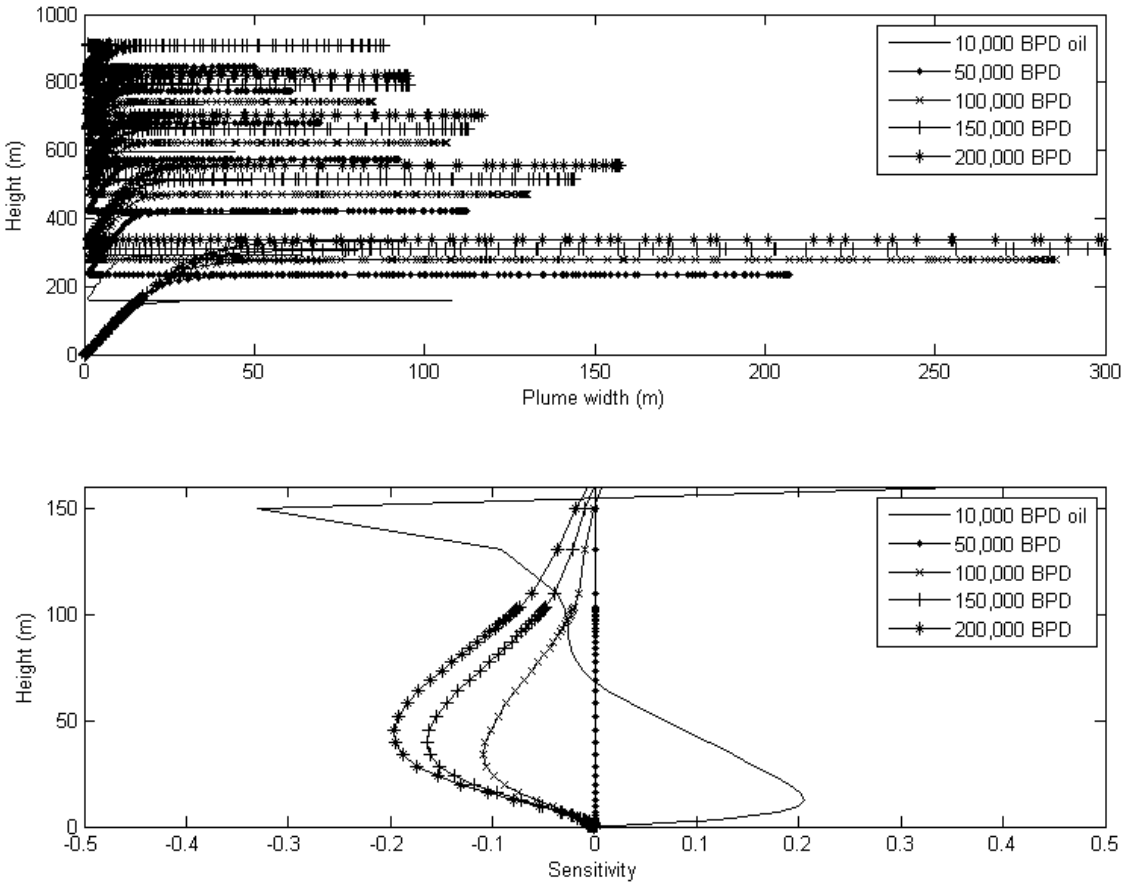

Figure A.13: Top: Raw data for inner plume width at a series of flow rates. Bottom: Sensitivity analysis of the width at the same flow rates. 50,000 BPD is used as the reference.

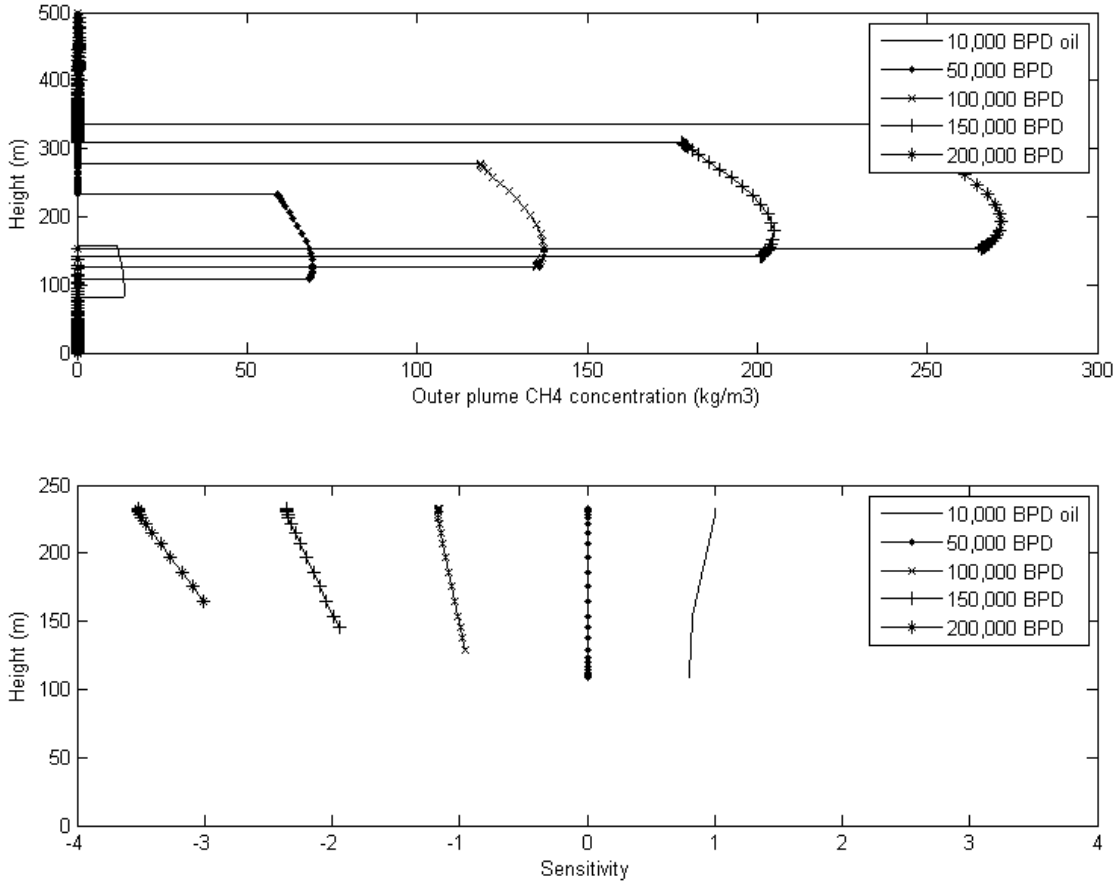

Figure A.14: Top: Raw data for outer plume CH4 concentration at a series of flow rates. Bottom: Sensitivity analysis of the CH4 at the same flow rates. 50,000 BPD is used as the reference.

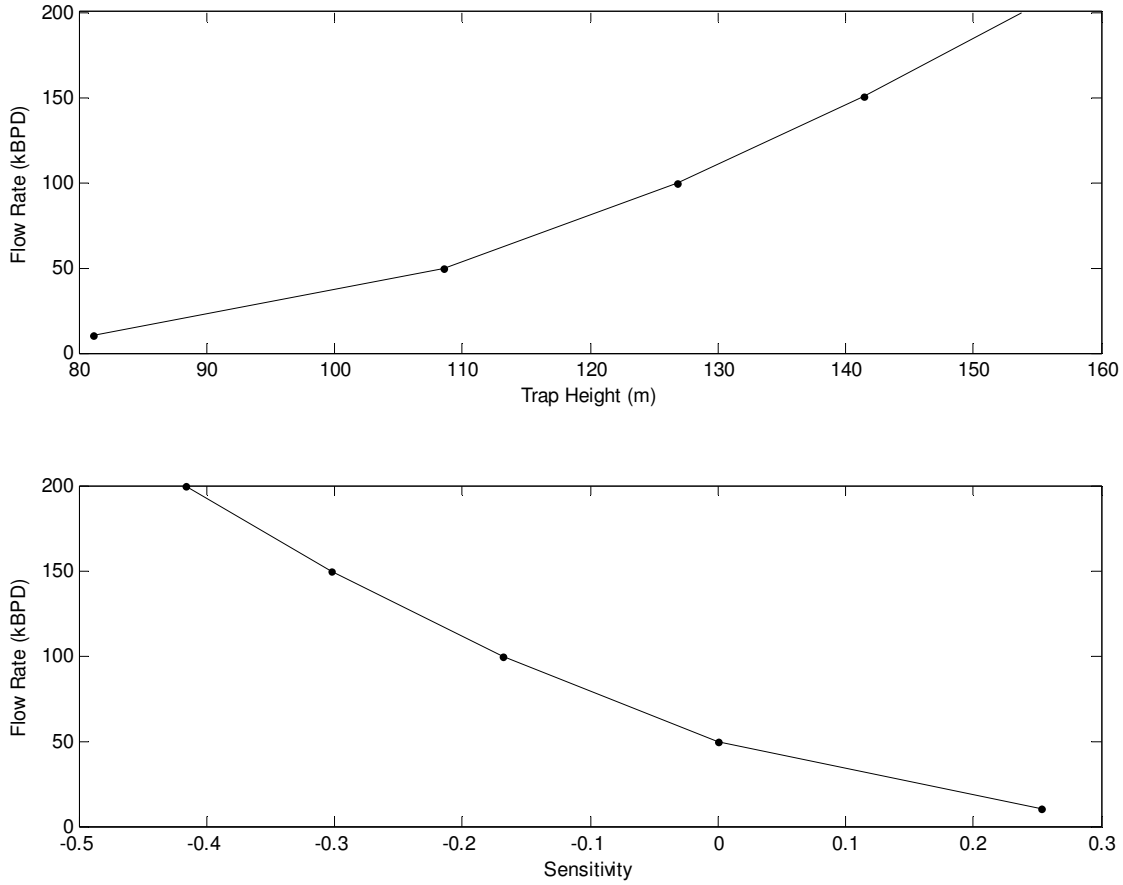

Figure A.15: Top: Trap height for the outer plume with respect to flow rate. Bottom: Sensitivity in relation to flow rate with 50,000 BPD used as the reference value.

A.2.4 Case 1, Depth: 1829 m, Bubble Diameter: 2 mm

This case applies to Figure A.16 through Figure A.20.

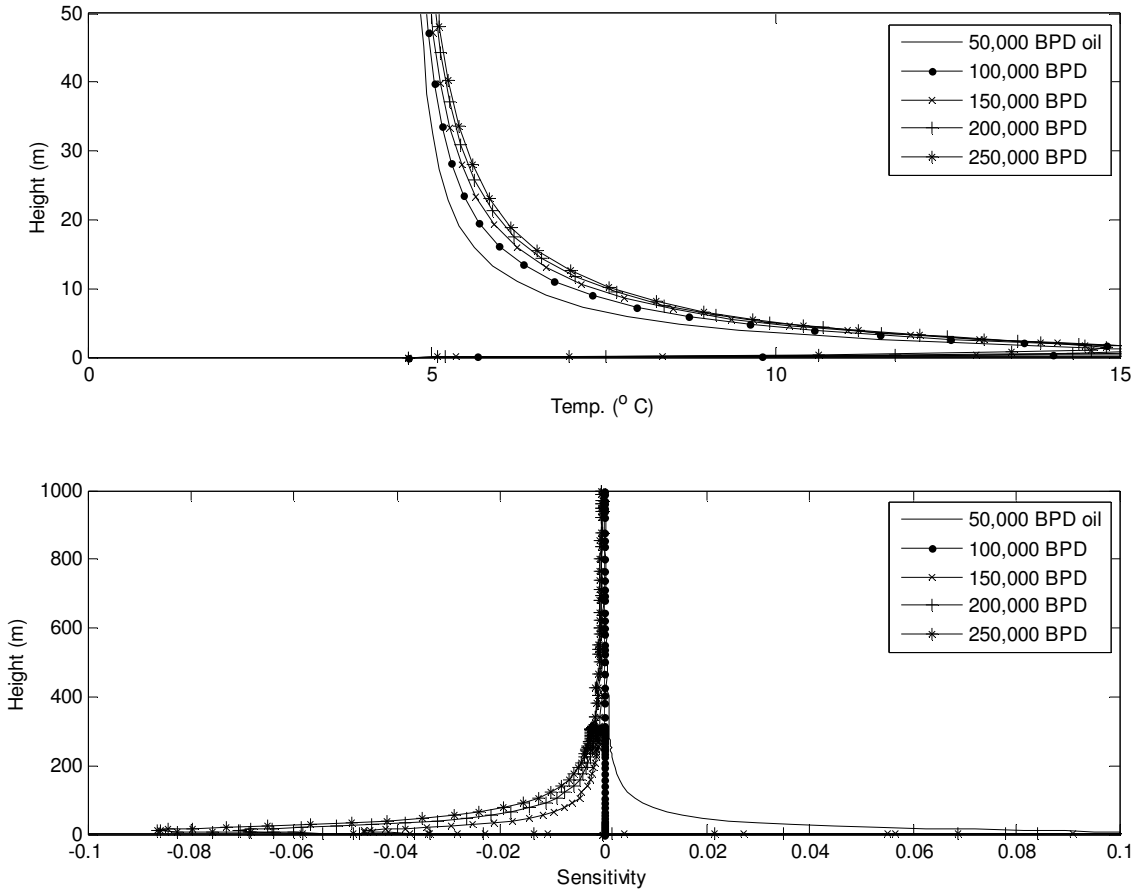

Figure A.16: Top: Raw data for inner plume temperature at a series of flow rates. Bottom: Sensitivity analysis of the temperature at the same flow rates. 100,000 BPD is used as the reference.

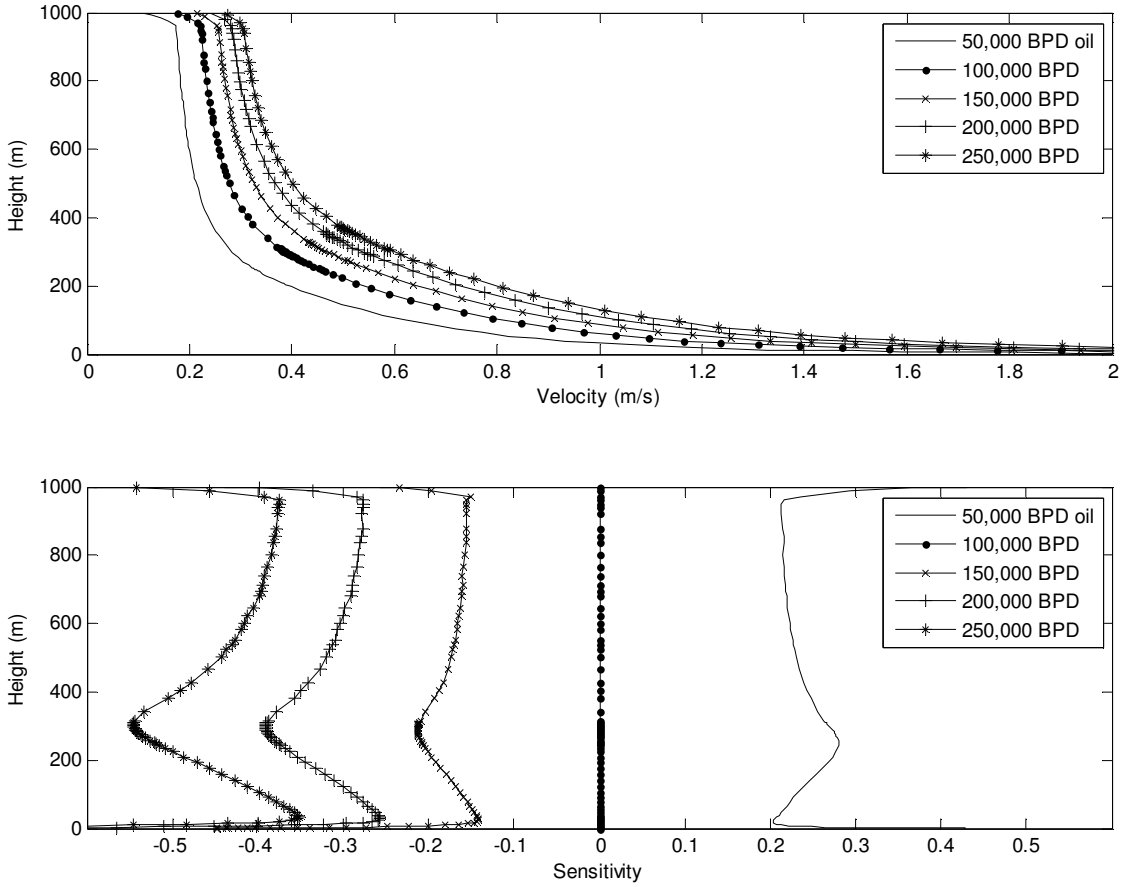

Figure A.17: Top: Raw data for inner plume mean velocity at a series of flow rates. Bottom: Sensitivity analysis of the mean velocity at the same flow rates. 100,000 BPD is used as the reference.

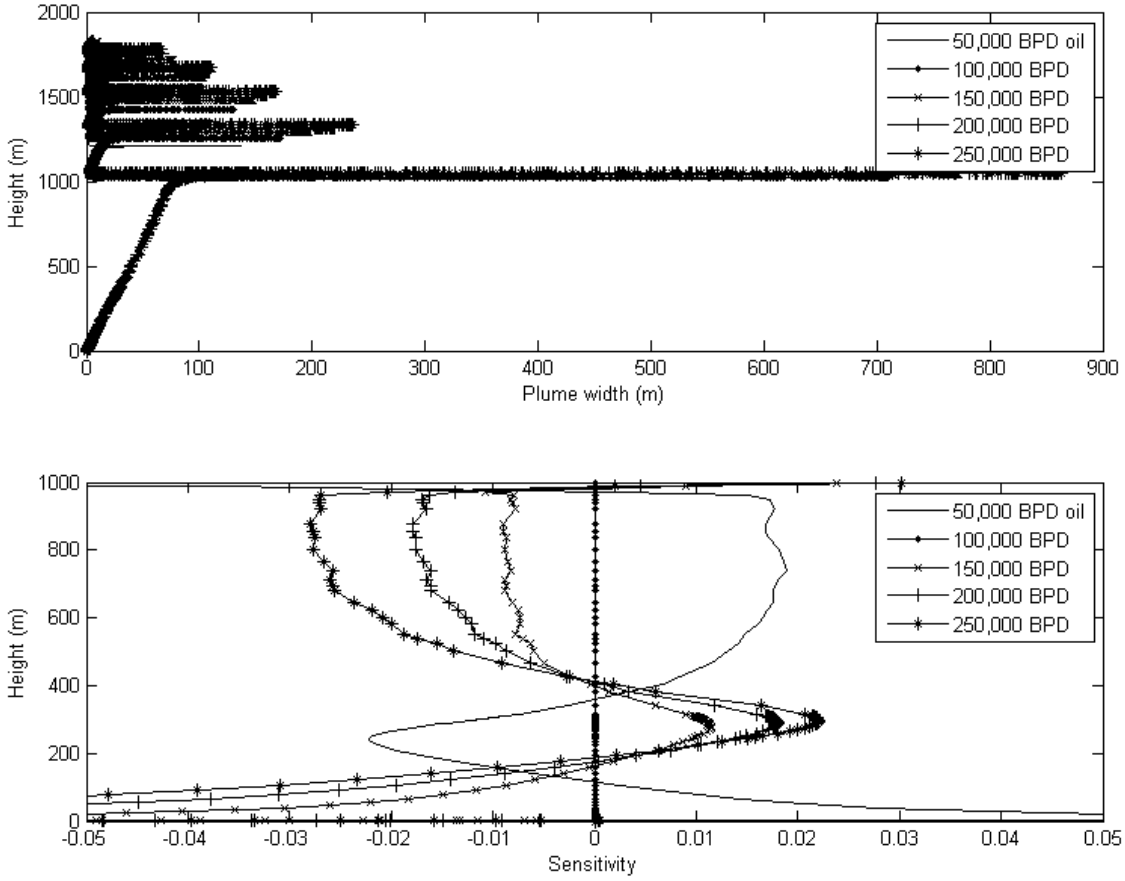

Figure A.18: Top: Raw data for inner plume width at a series of flow rates. Bottom: Sensitivity analysis of the width at the same flow rates. 100,000 BPD is used as the reference.

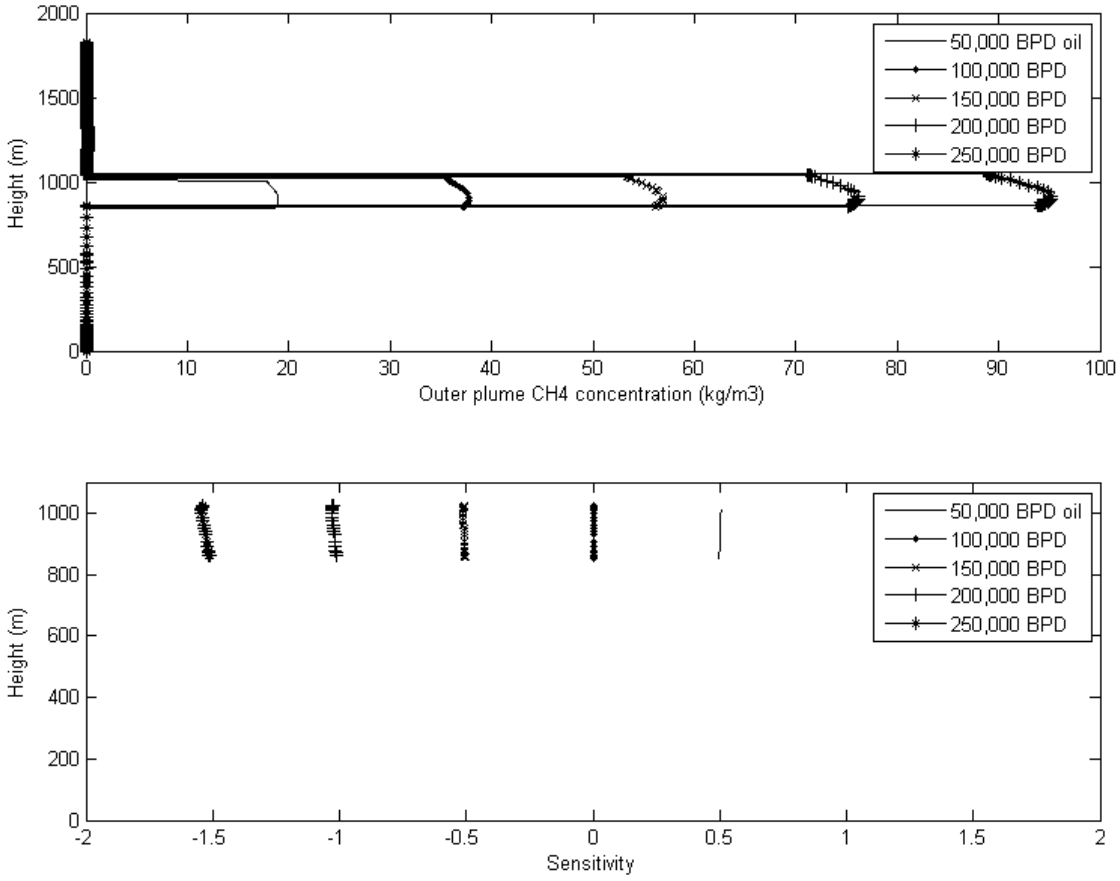

Figure A.19: Top: Raw data for outer plume CH4 concentration at a series of flow rates. Bottom: Sensitivity analysis of the CH4 at the same flow rates. 100,000 BPD is used as the reference.

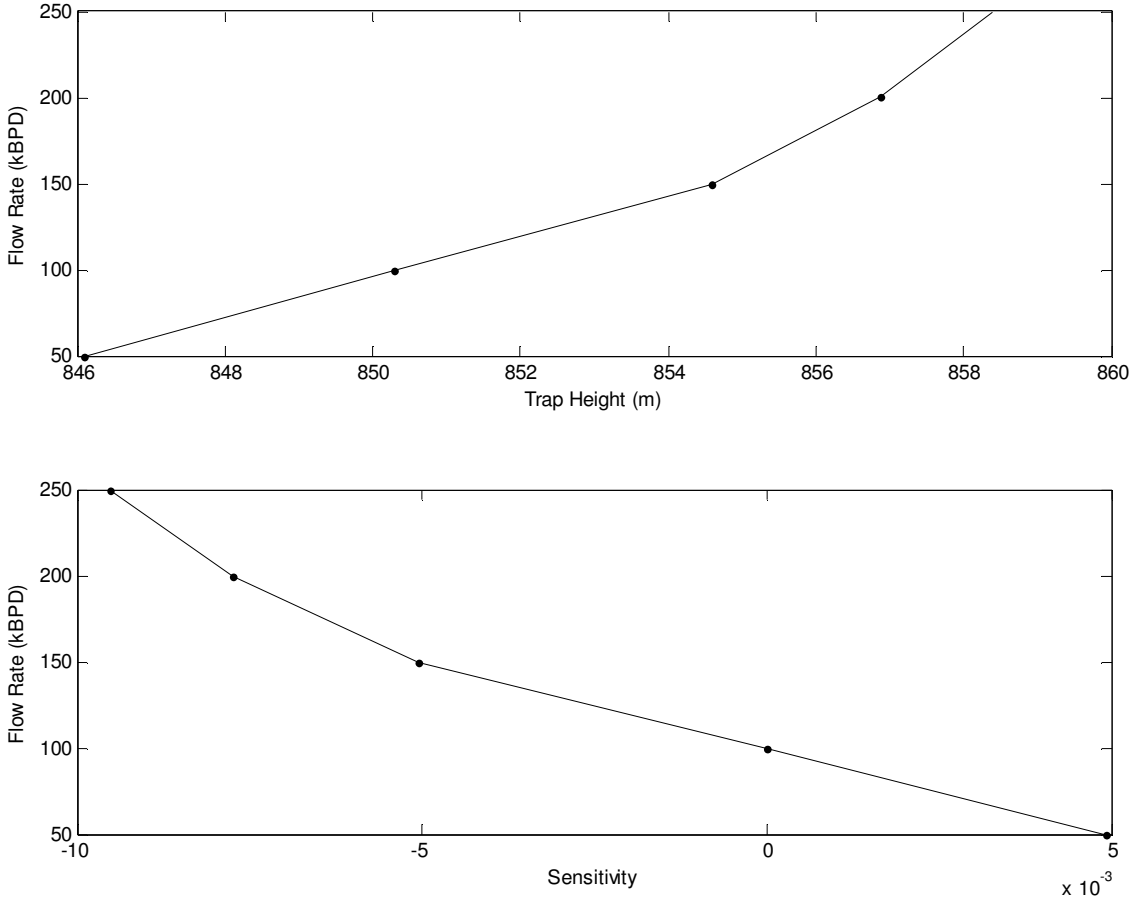

Figure A.20: Top: Trap height for the outer plume with respect to flow rate. Bottom: Sensitivity in relation to flow rate with 100,000 BPD used as the reference value.

A.2.5 Case 2, Depth: 3000 m, Bubble Diameter: 2 mm

This case applies to Figure A.21 through Figure A.25.

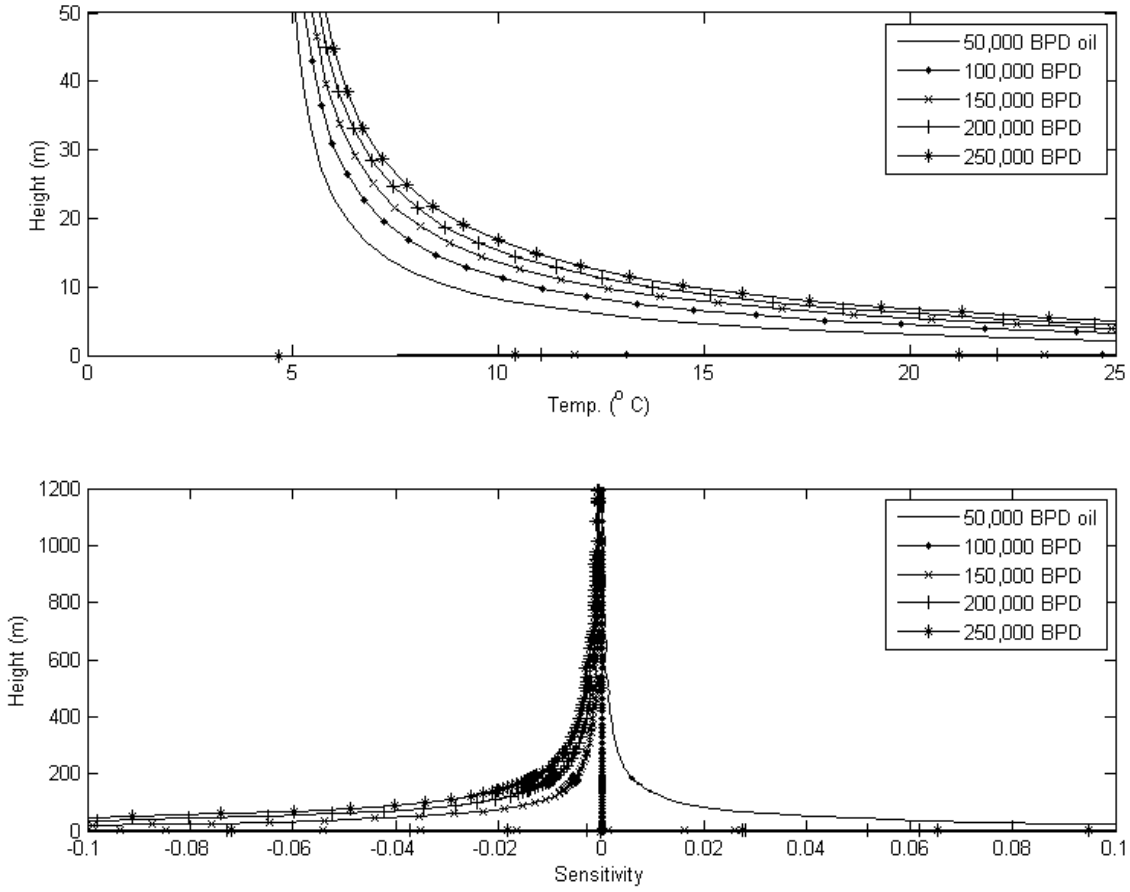

Figure A.21: Top: Raw data for inner plume temperature at a series of flow rates. Bottom: Sensitivity analysis of the temperature at the same flow rates. 100,000 BPD is used as the reference.

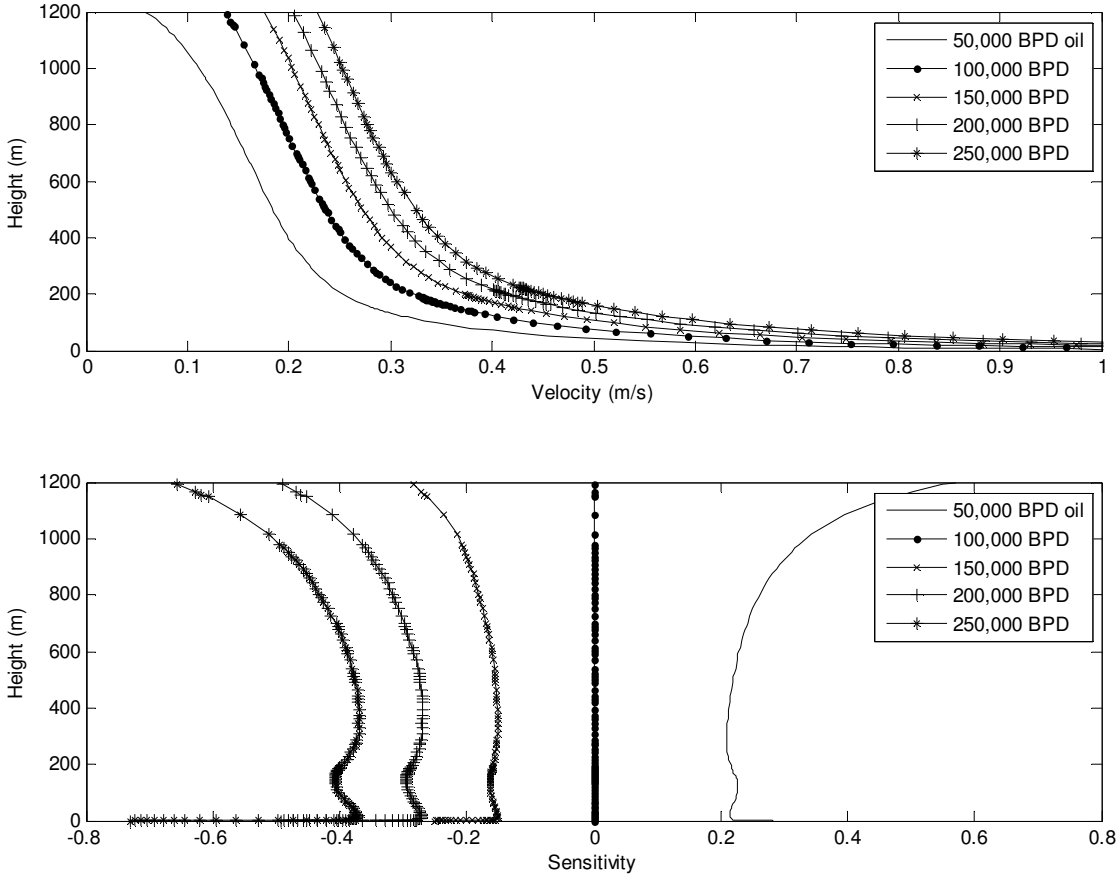

Figure A.22: Top: Raw data for inner plume mean velocity at a series of flow rates. Bottom: Sensitivity analysis of the mean velocity at the same flow rates. 100,000 BPD is used as the reference.

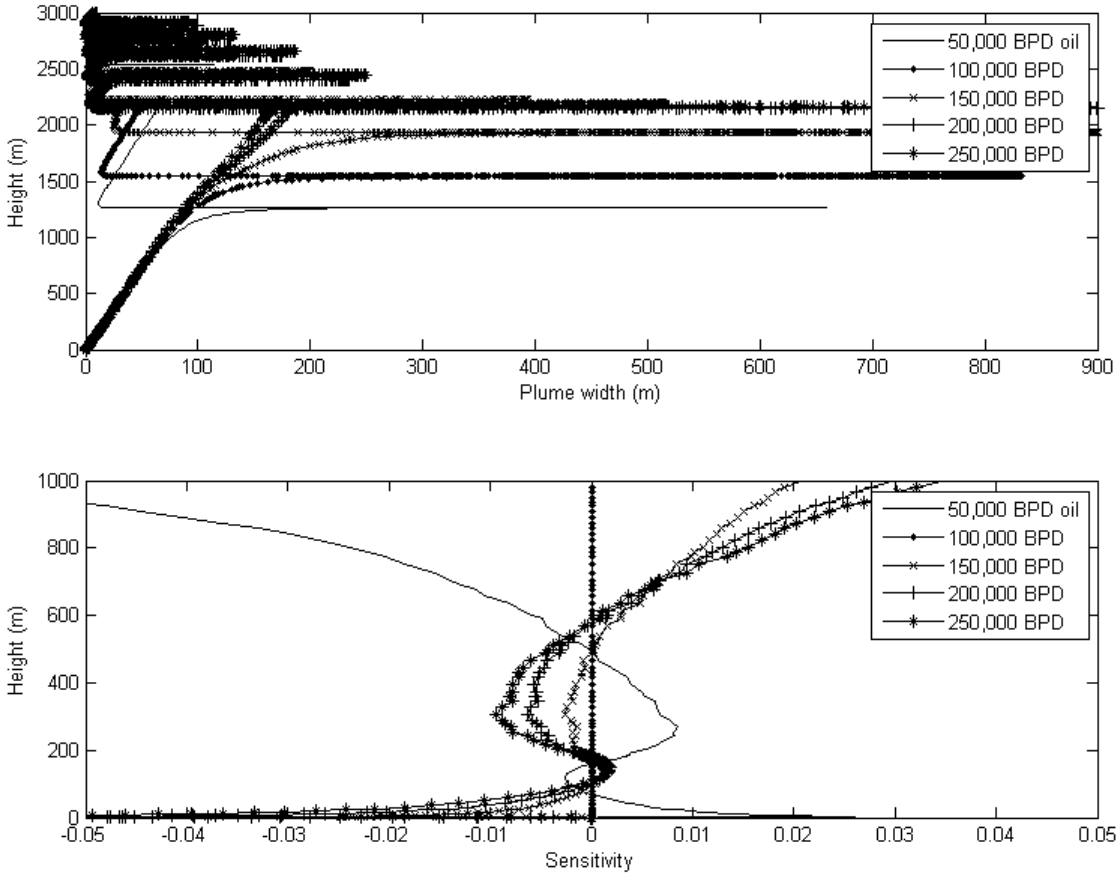

Figure A.23: Top: Raw data for inner plume width at a series of flow rates. Bottom: Sensitivity analysis of the width at the same flow rates. 100,000 BPD is used as the reference.

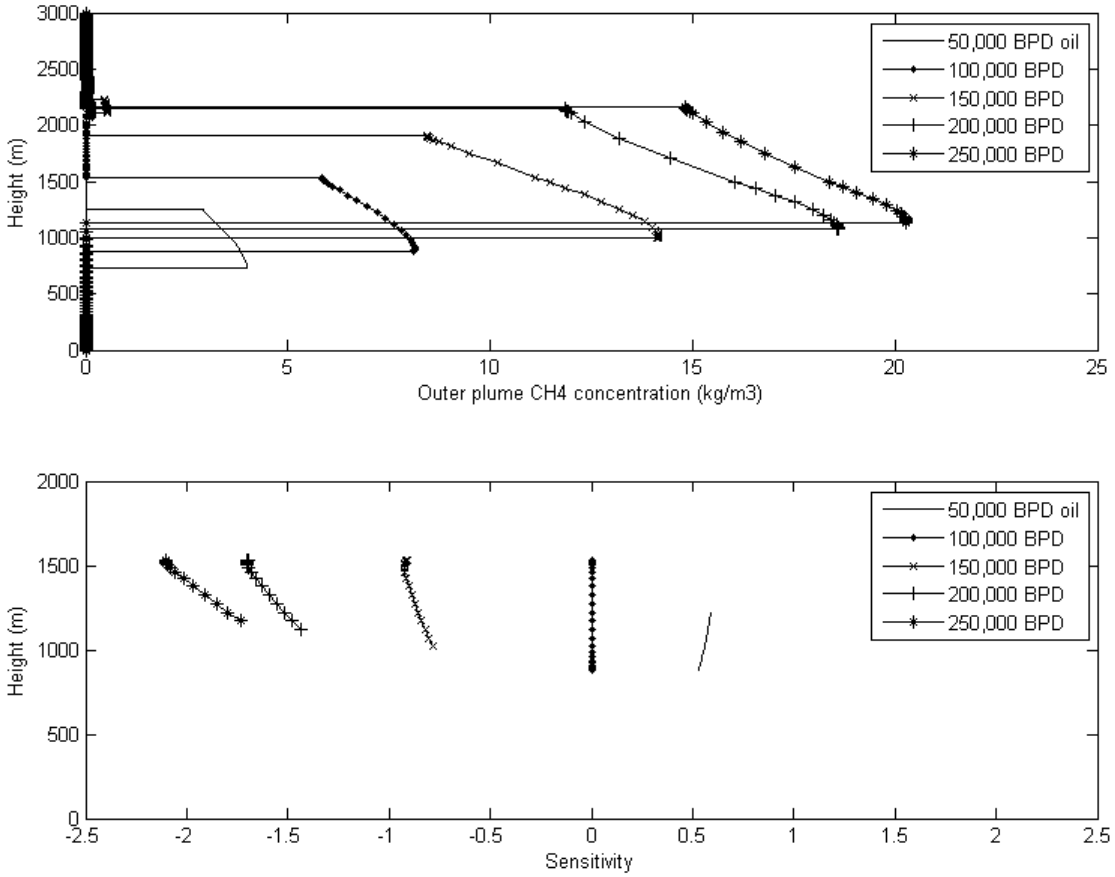

Figure A.24: Top: Raw data for outer plume CH4 concentration at a series of flow rates. Bottom: Sensitivity analysis of the CH4 at the same flow rates. 100,000 BPD is used as the reference.

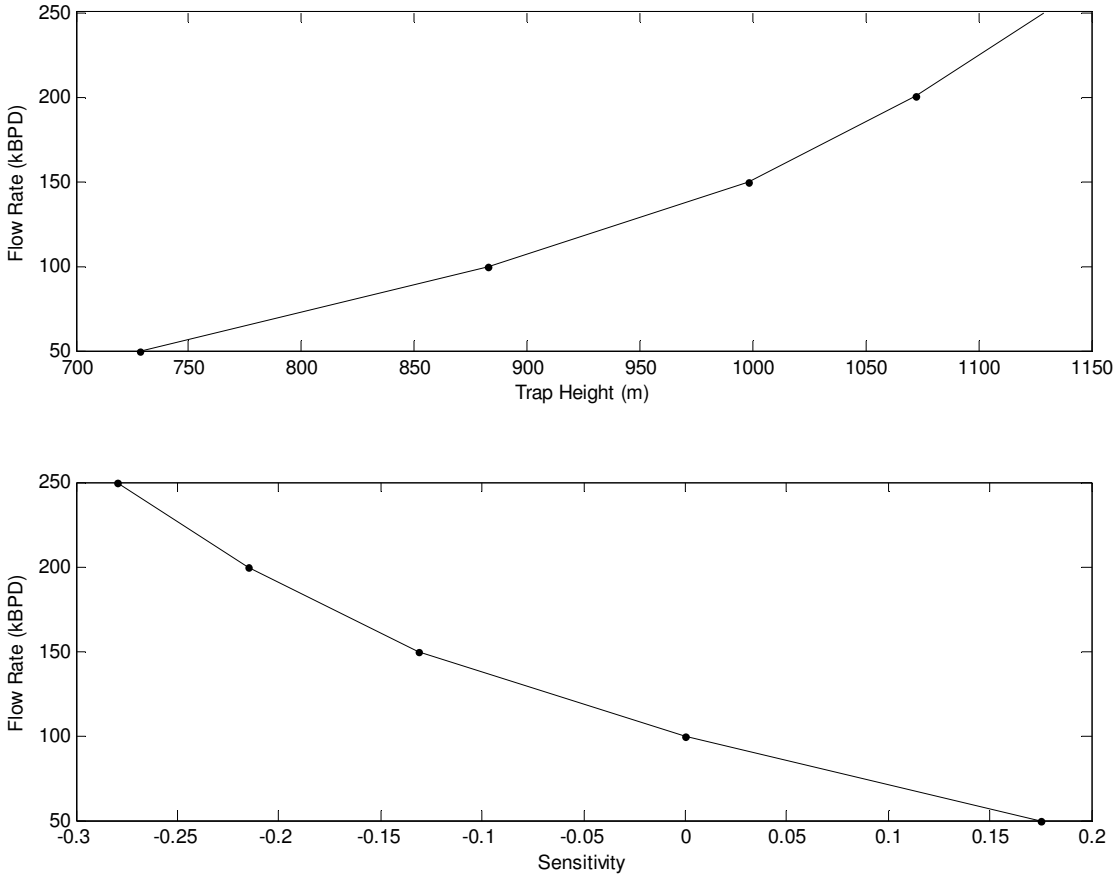

Figure A.25: Top: Trap height for the outer plume with respect to flow rate. Bottom: Sensitivity in relation to flow rate with 100,000 BPD used as the reference value.

A.2.6 Case 3, Depth: 914 m, Bubble Diameter: 2 mm

This case applies to Figure A.26 through Figure A.30.

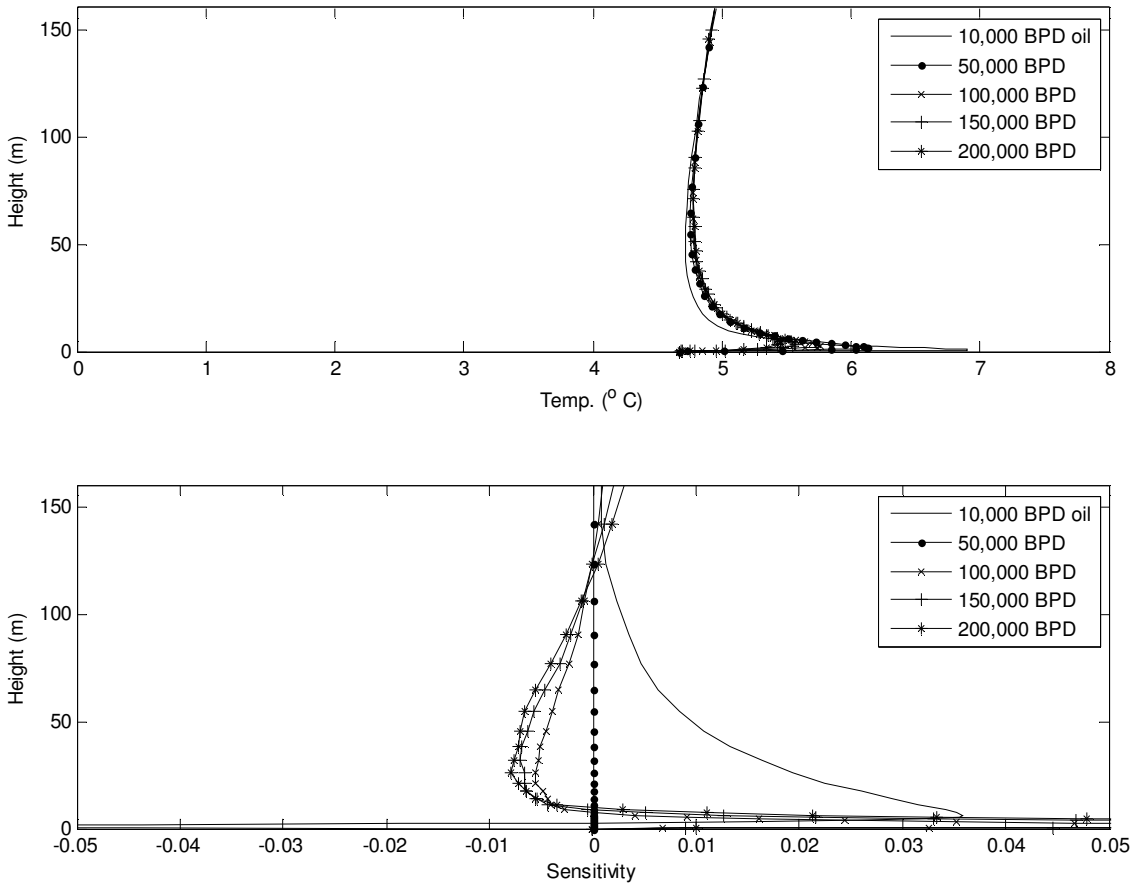

Figure A.26: Top: Raw data for inner plume temperature at a series of flow rates. Bottom: Sensitivity analysis of the temperature at the same flow rates. 50,000 BPD is used as the reference.

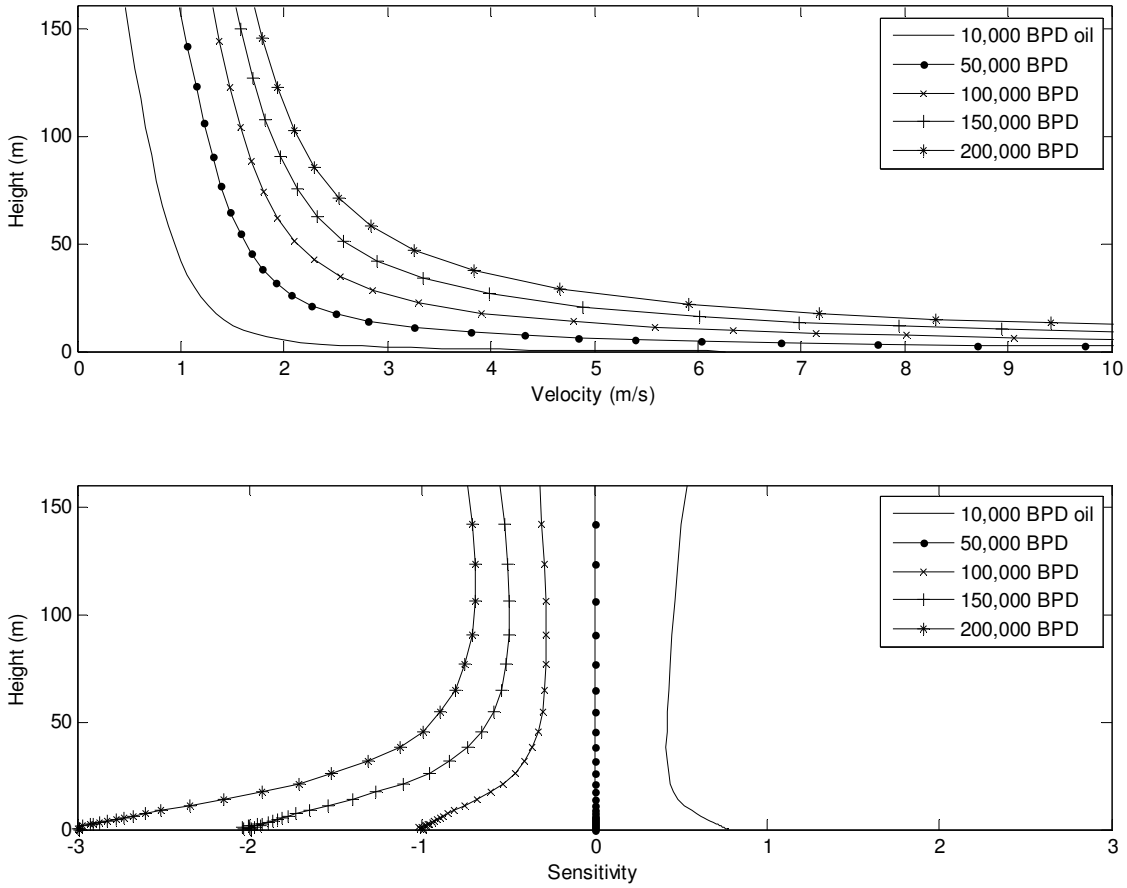

Figure A.27: Top: Raw data for inner plume mean velocity at a series of flow rates. Bottom: Sensitivity analysis of the mean velocity at the same flow rates. 50,000 BPD is used as the reference.

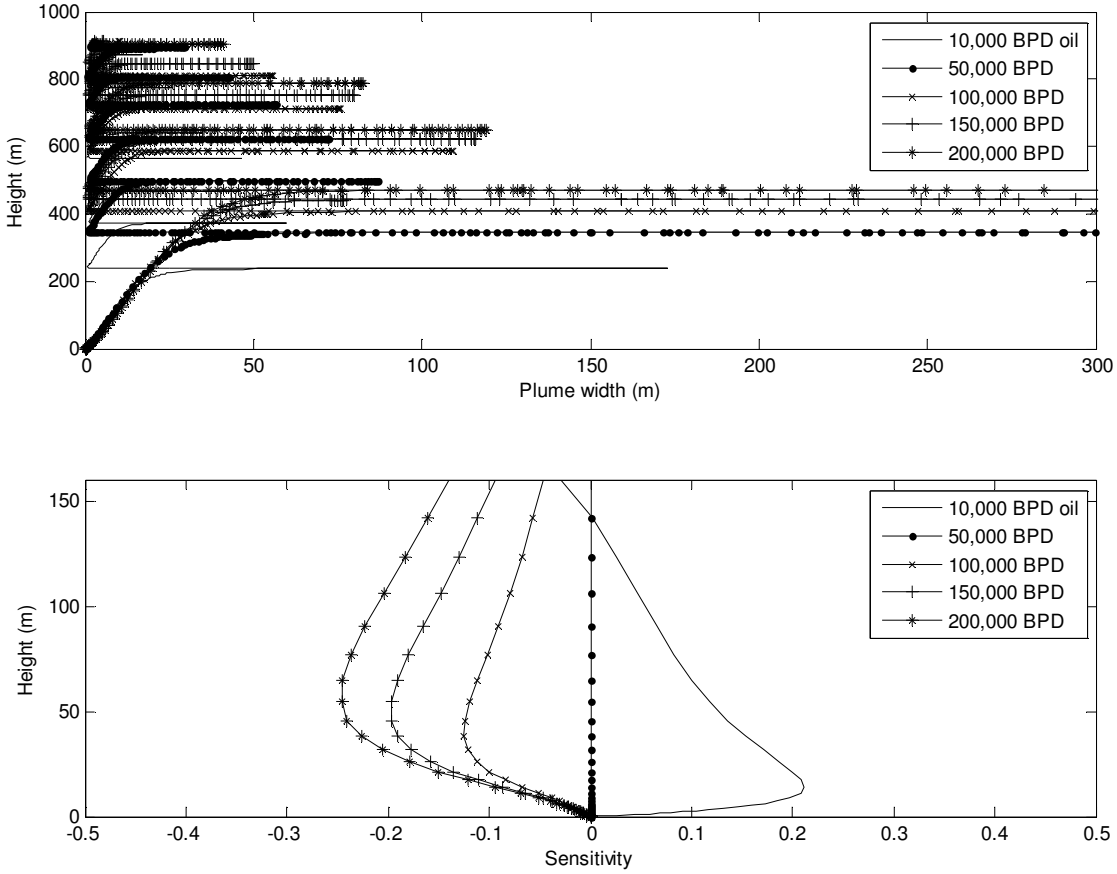

Figure A.28: Top: Raw data for inner plume width at a series of flow rates. Bottom: Sensitivity analysis of the width at the same flow rates. 50,000 BPD is used as the reference.

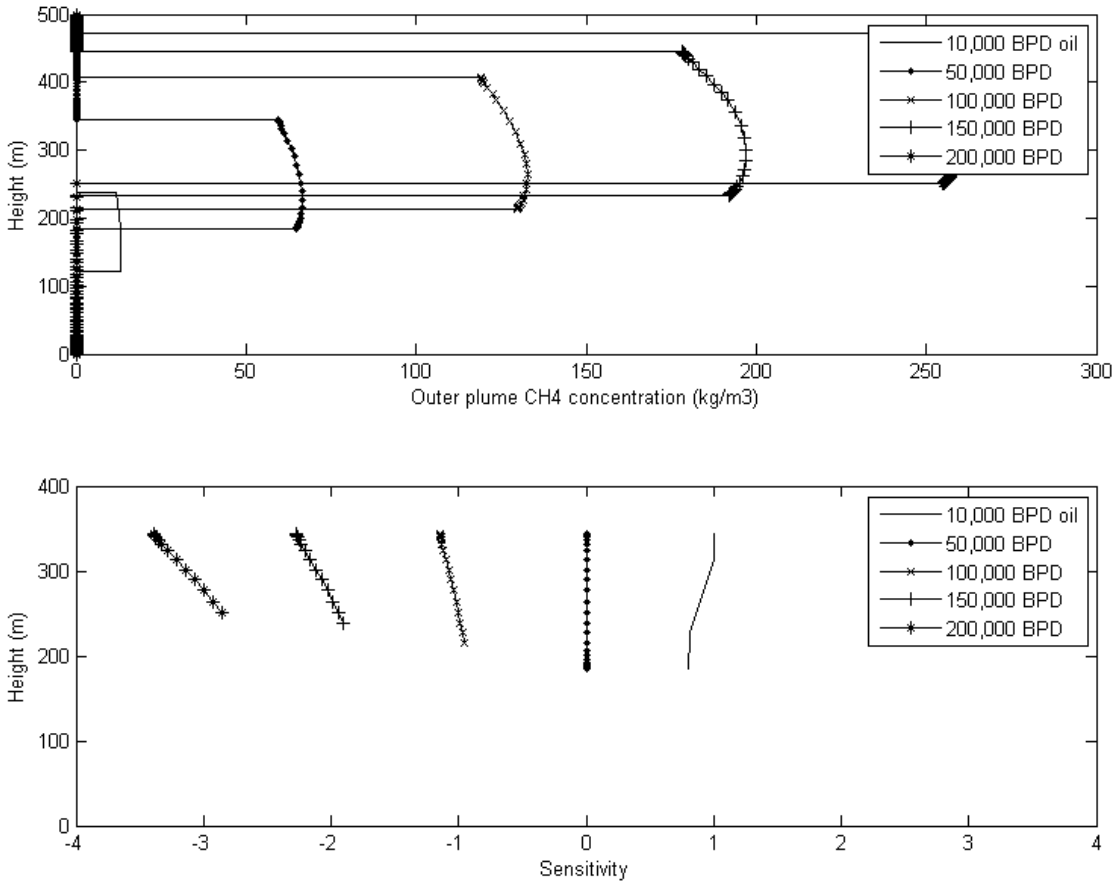

Figure A.29: Top: Raw data for outer plume CH4 concentration at a series of flow rates. Bottom: Sensitivity analysis of the CH4 at the same flow rates. 50,000 BPD is used as the reference.

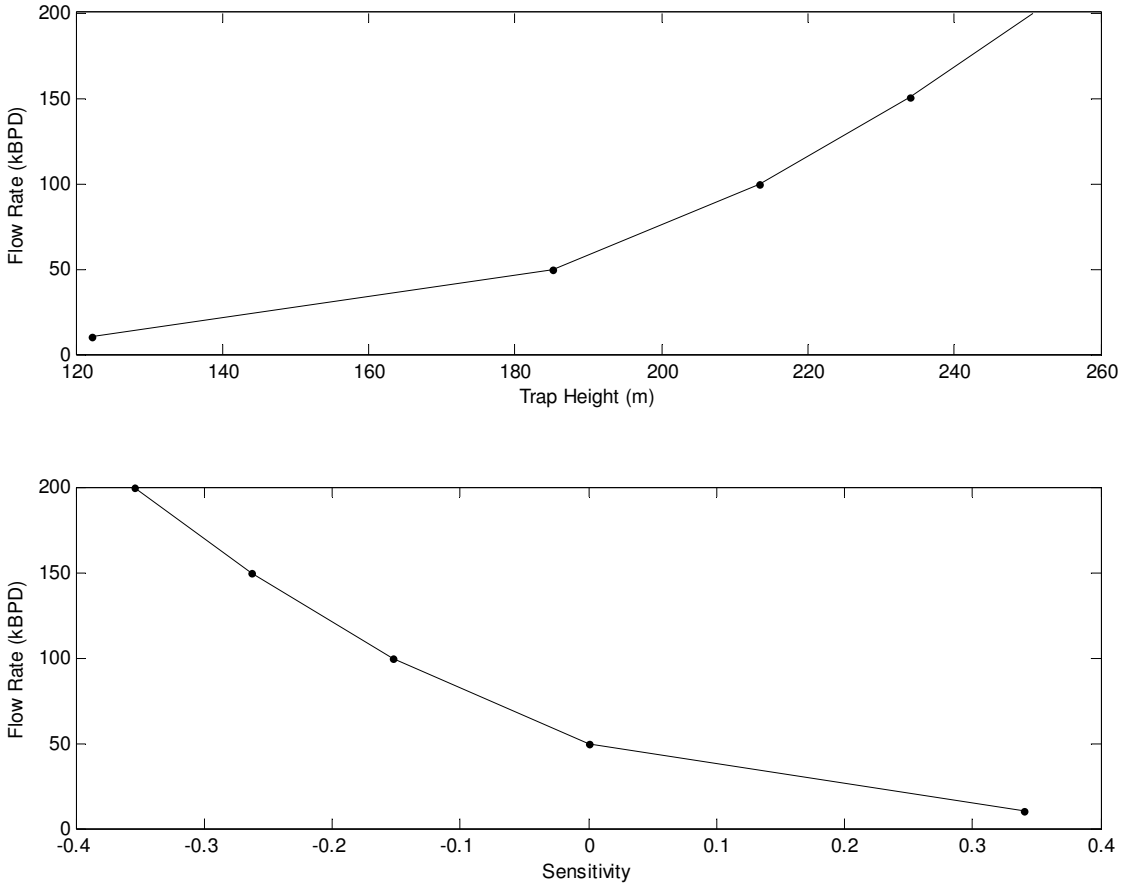

Figure A.30: Top: Trap height for the outer plume with respect to flow rate. Bottom: Sensitivity in relation to flow rate with 50,000 BPD used as the reference value.

A.2.7 Case 1, Depth: 1829 m, Bubble Diameter: 4 mm

This case applies to Figure A.31 through Figure A.35.

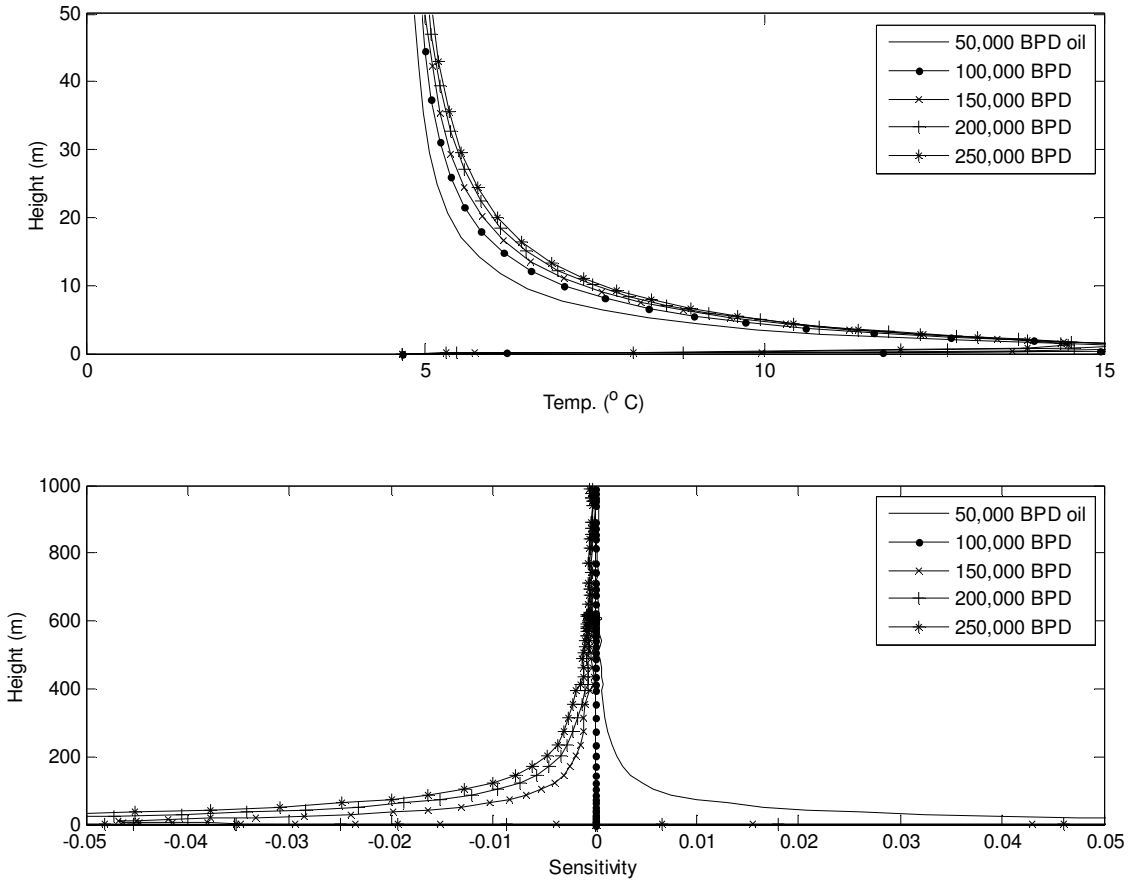

Figure A.31: Top: Raw data for inner plume temperature at a series of flow rates. Bottom: Sensitivity analysis of the temperature at the same flow rates. 100,000 BPD is used as the reference.

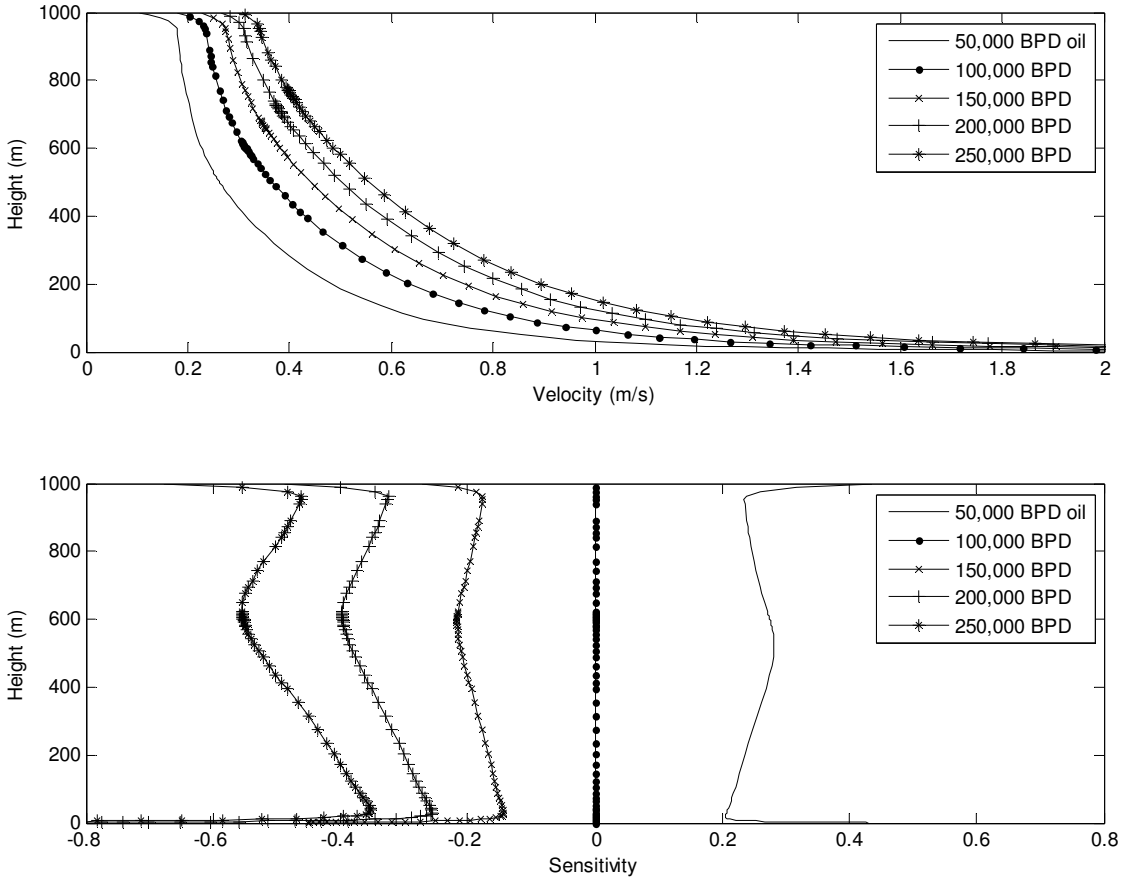

Figure A.32: Top: Raw data for inner plume mean velocity at a series of flow rates. Bottom: Sensitivity analysis of the mean velocity at the same flow rates. 100,000 BPD is used as the reference.

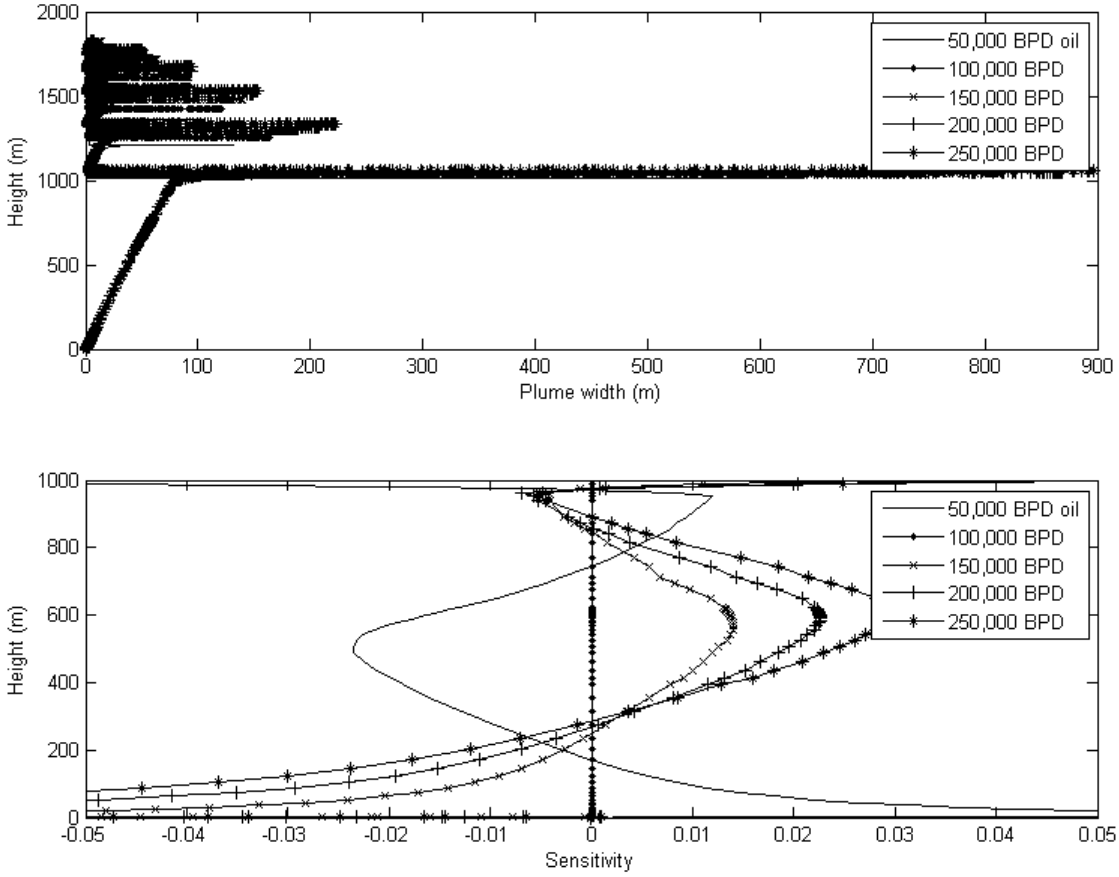

Figure A.33: Top: Raw data for inner plume width at a series of flow rates. Bottom: Sensitivity analysis of the width at the same flow rates. 100,000 BPD is used as the reference.

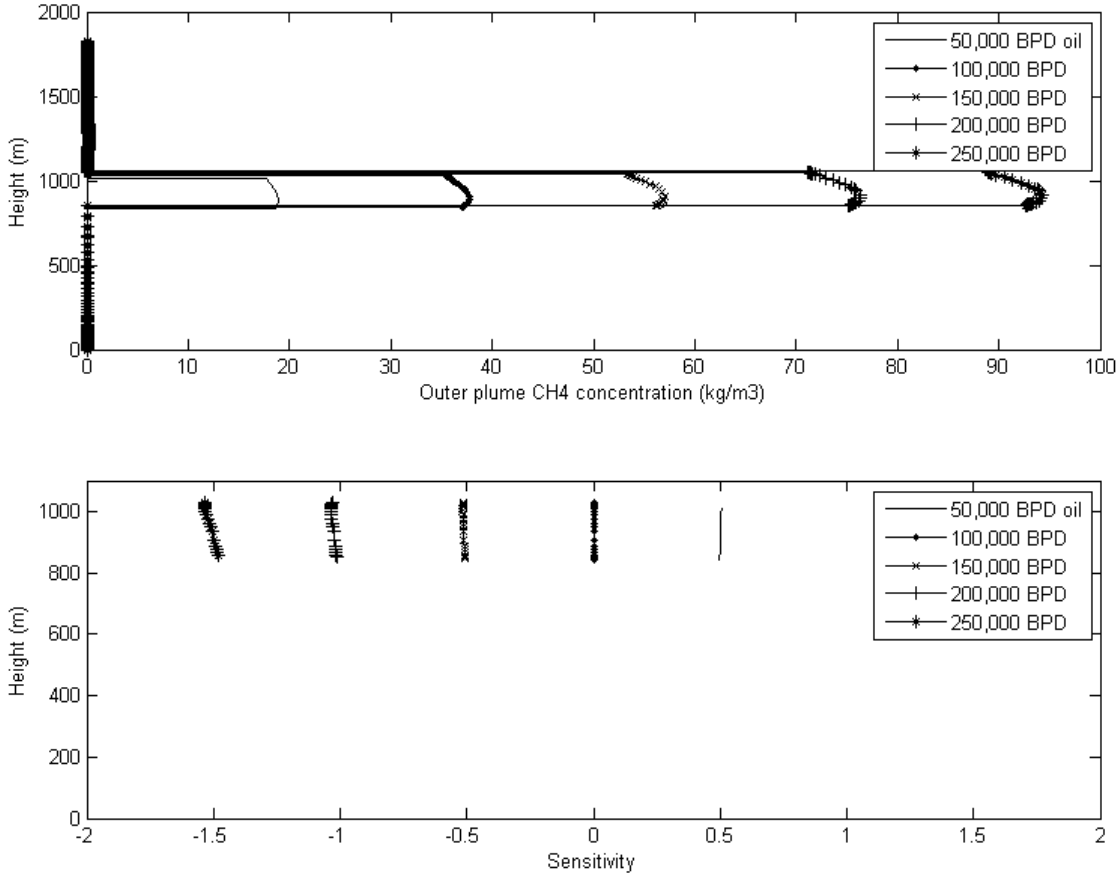

Figure A.34: Top: Raw data for outer plume CH4 concentration at a series of flow rates. Bottom: Sensitivity analysis of the CH4 at the same flow rates. 100,000 BPD is used as the reference.

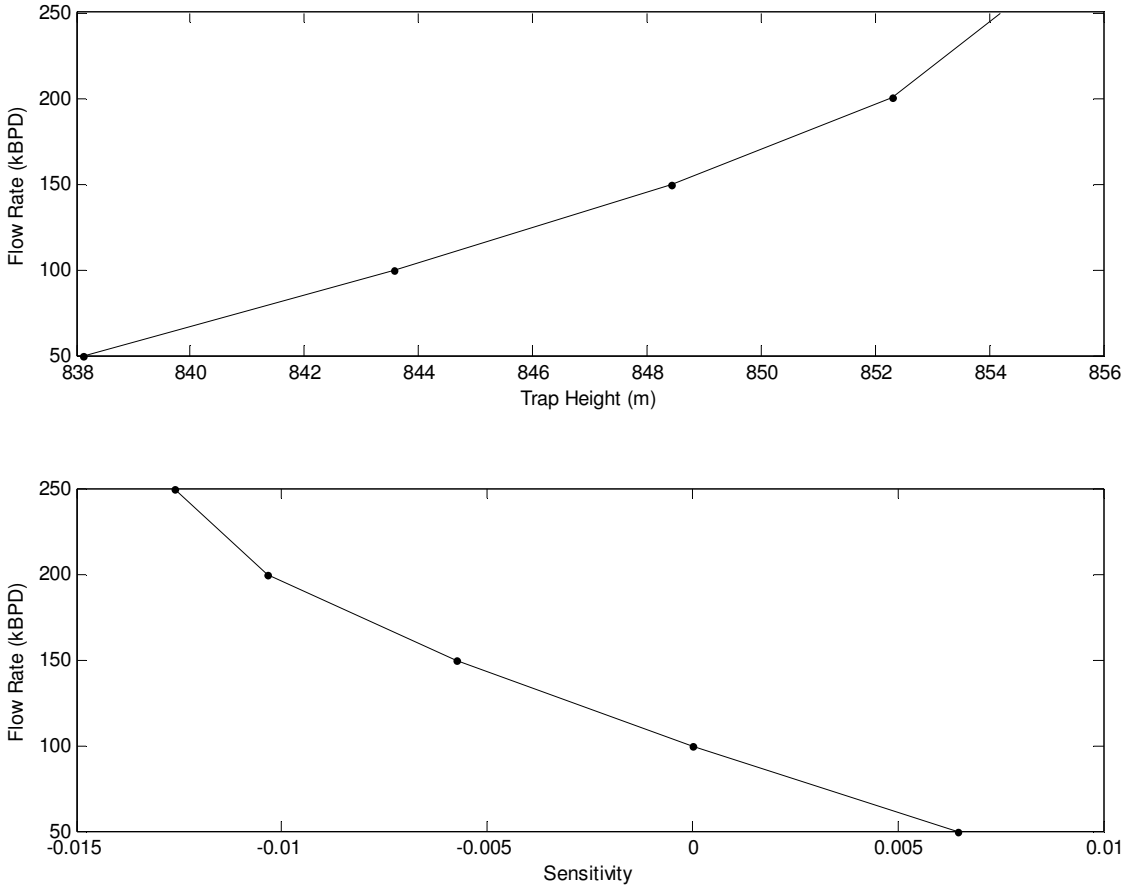

Figure A.35: Top: Trap height for the outer plume with respect to flow rate. Bottom: Sensitivity in relation to flow rate with 100,000 BPD used as the reference value.

A.2.8 Case 2, Depth: 3000 m, Bubble Diameter: 4 mm

This case applies to Figure A.36 through Figure A.40.

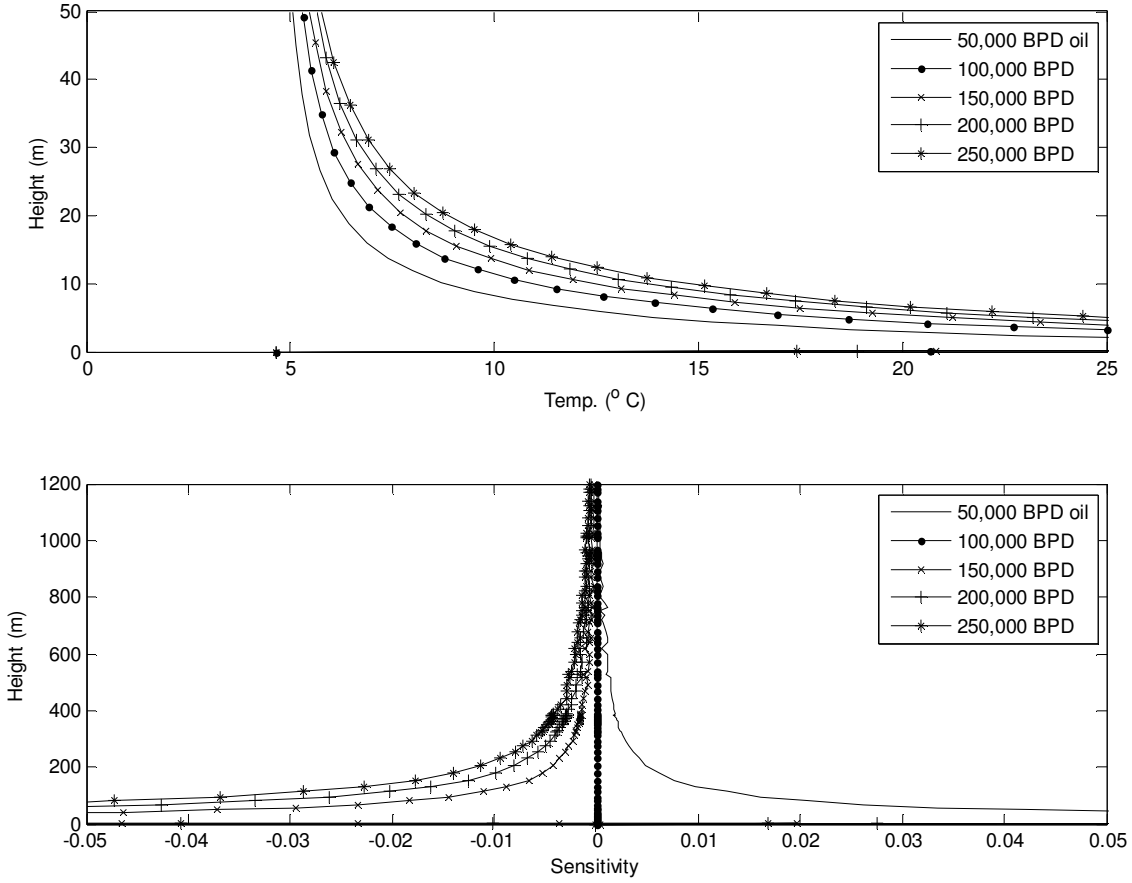

Figure A.36: Top: Raw data for inner plume temperature at a series of flow rates. Bottom: Sensitivity analysis of the temperature at the same flow rates. 100,000 BPD is used as the reference.

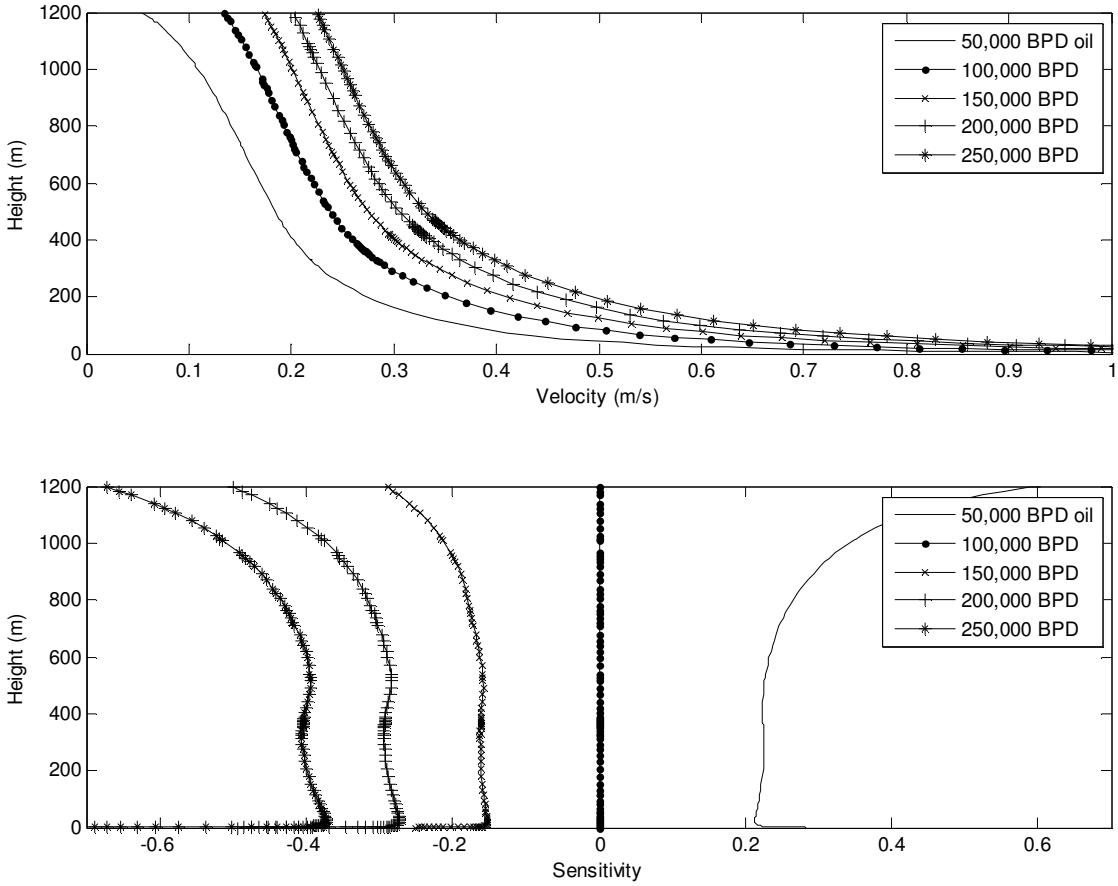

Figure A.37: Top: Raw data for inner plume mean velocity at a series of flow rates. Bottom: Sensitivity analysis of the mean velocity at the same flow rates. 100,000 BPD is used as the reference.

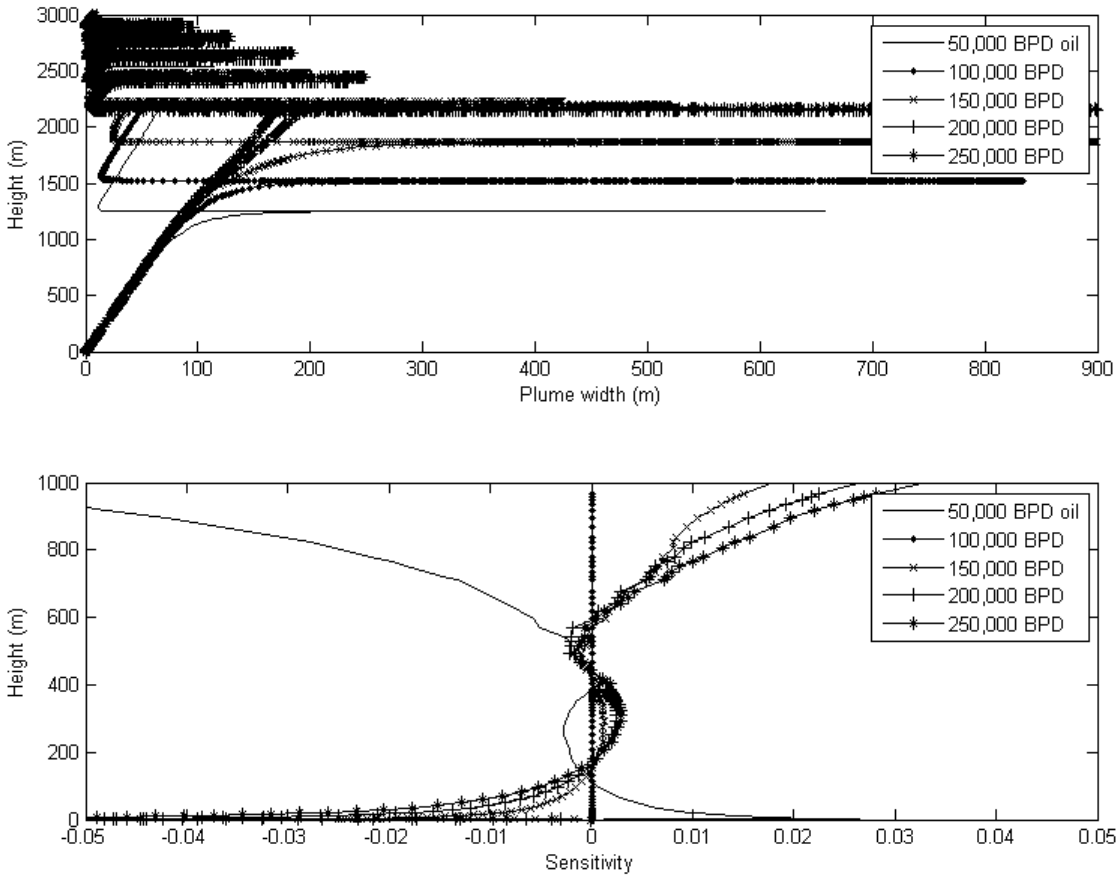

Figure A.38: Top: Raw data for inner plume width at a series of flow rates. Bottom: Sensitivity analysis of the width at the same flow rates. 100,000 BPD is used as the reference.

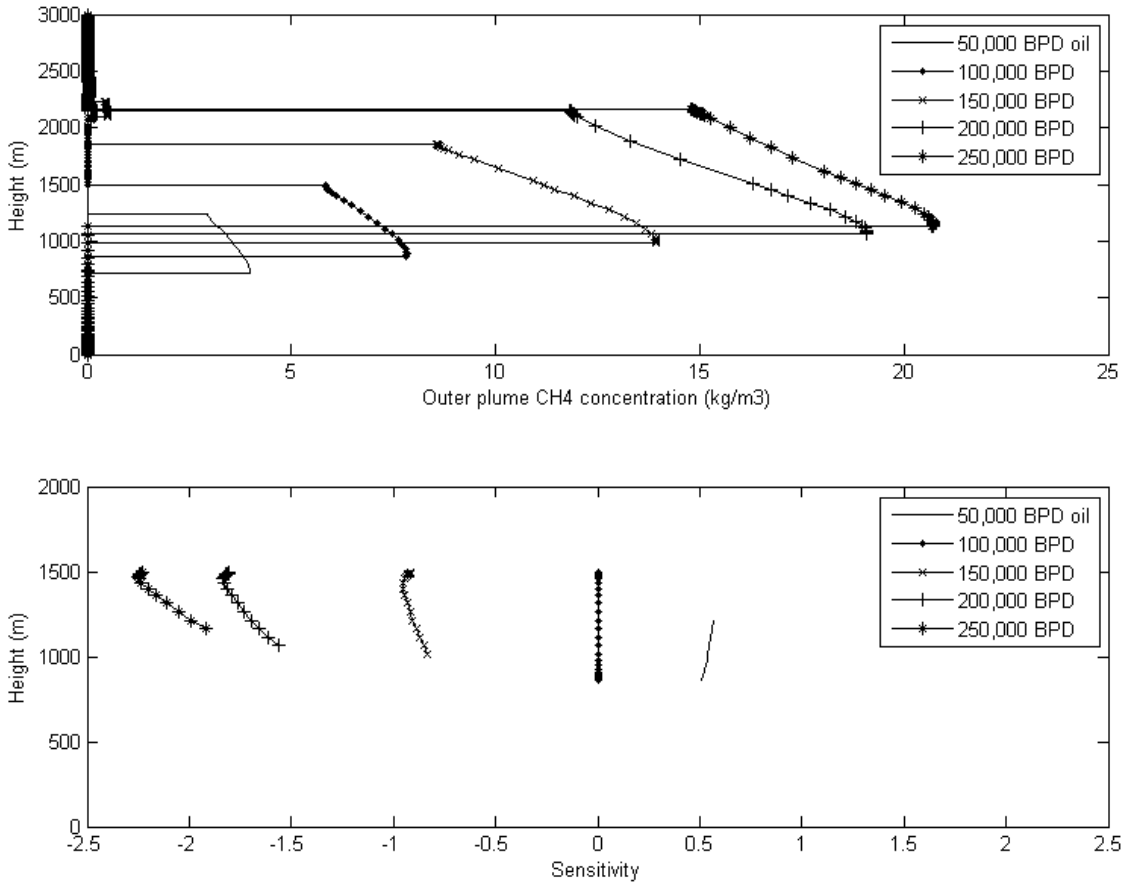

Figure A.39: Top: Raw data for outer plume CH4 concentration at a series of flow rates. Bottom: Sensitivity analysis of the CH4 at the same flow rates. 100,000 BPD is used as the reference.

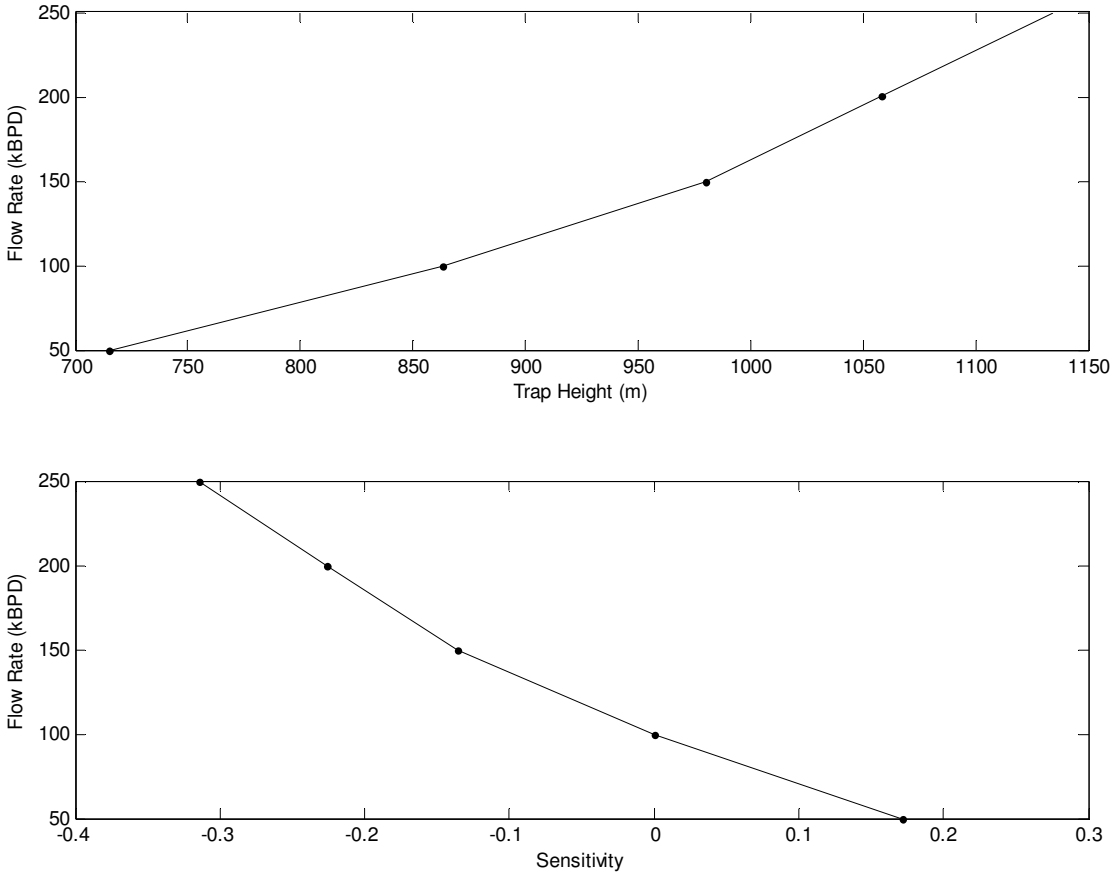

Figure A.40: Top: Trap height for the outer plume with respect to flow rate. Bottom: Sensitivity in relation to flow rate with 100,000 BPD used as the reference value.

A.2.9 Case 3, Depth: 914 m, Bubble Diameter: 4 mm

This case applies to Figure A.41 through Figure A.45.

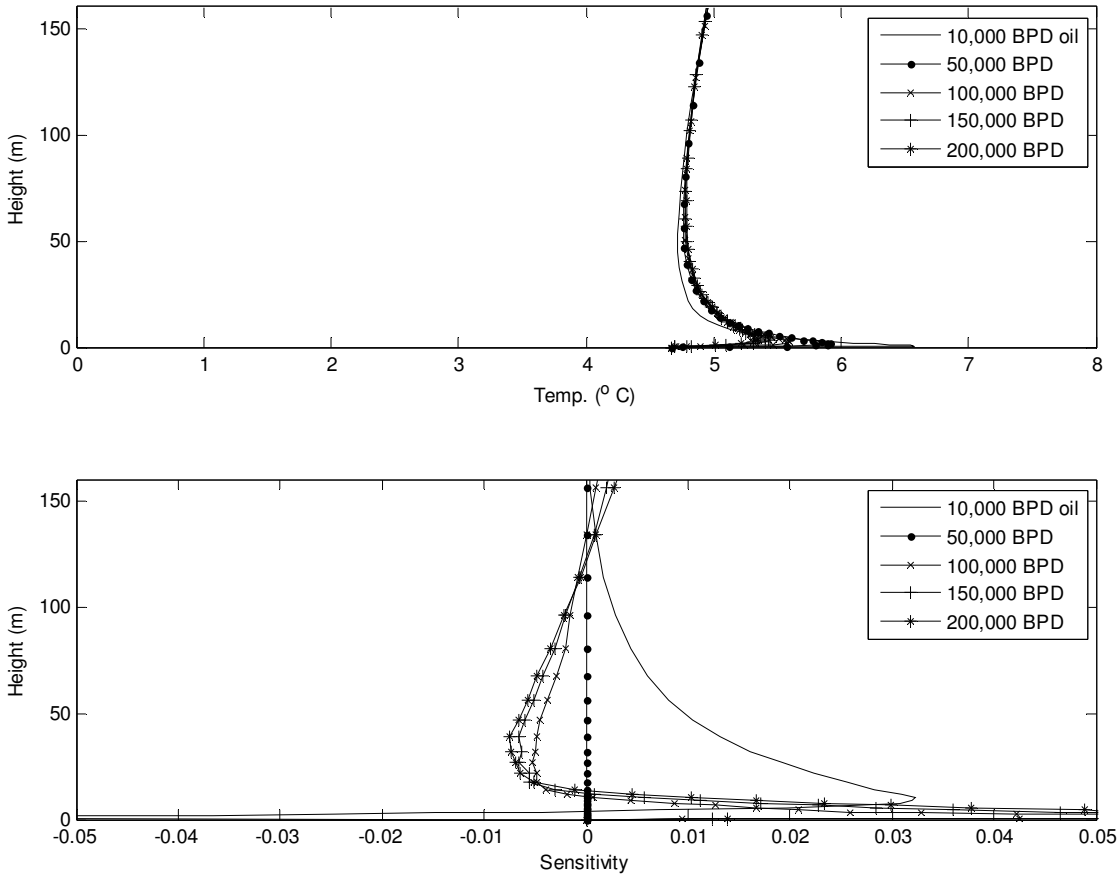

Figure A.41: Top: Raw data for inner plume temperature at a series of flow rates. Bottom: Sensitivity analysis of the temperature at the same flow rates. 50,000 BPD is used as the reference.

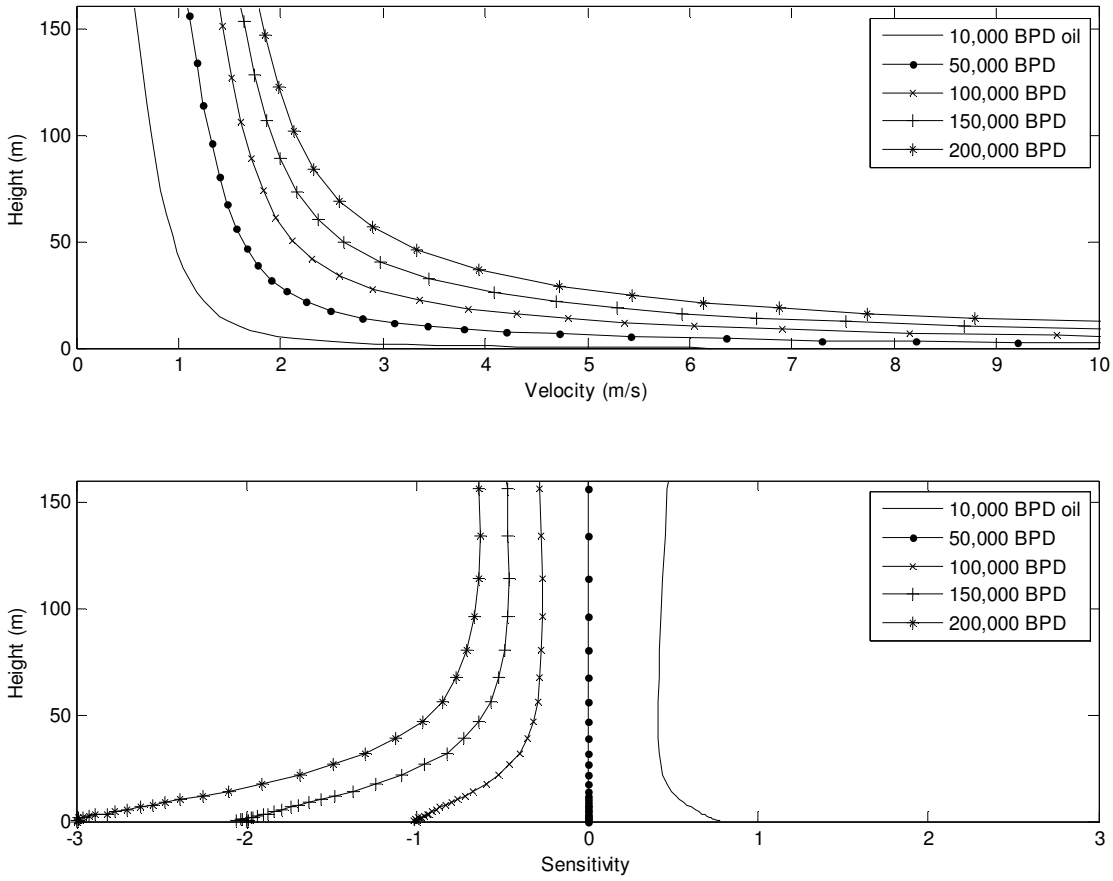

Figure A.42: Top: Raw data for inner plume mean velocity at a series of flow rates. Bottom: Sensitivity analysis of the mean velocity at the same flow rates. 50,000 BPD is used as the reference.

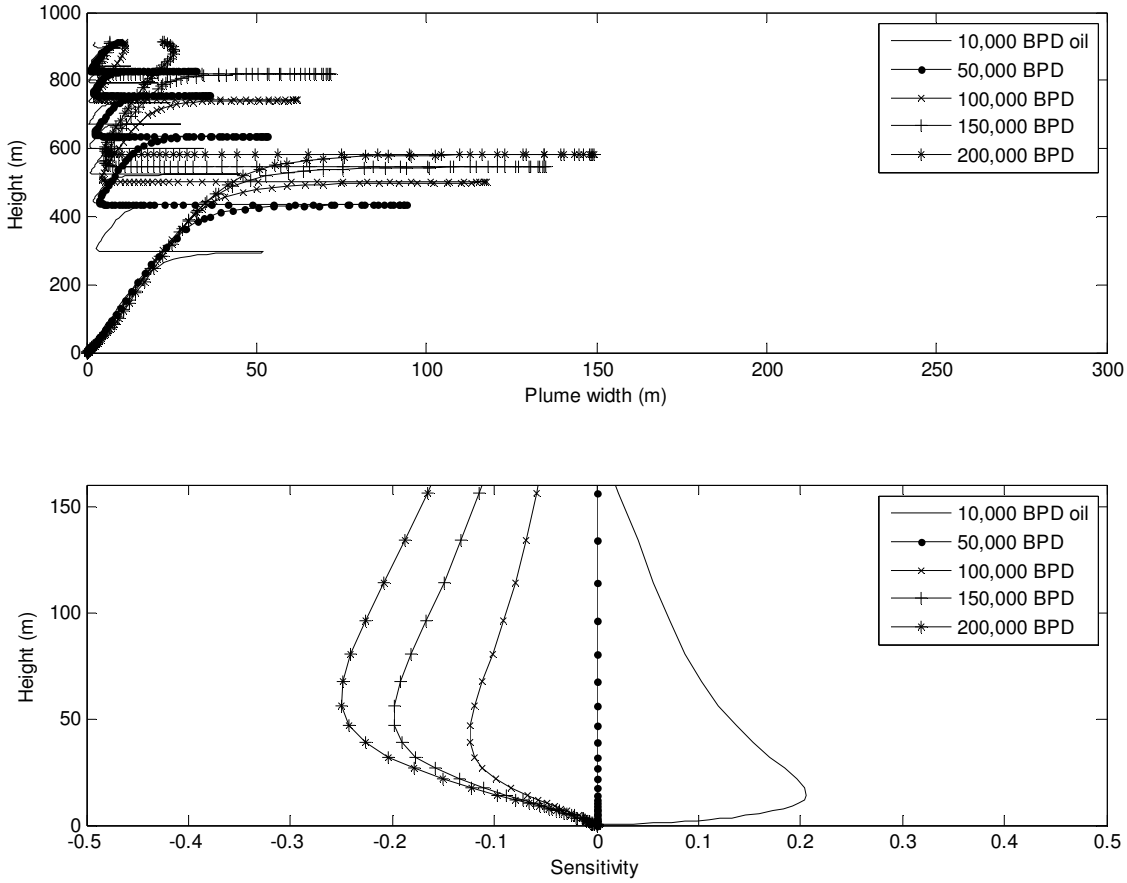

Figure A.43: Top: Raw data for inner plume width at a series of flow rates. Bottom: Sensitivity analysis of the width at the same flow rates. 50,000 BPD is used as the reference.

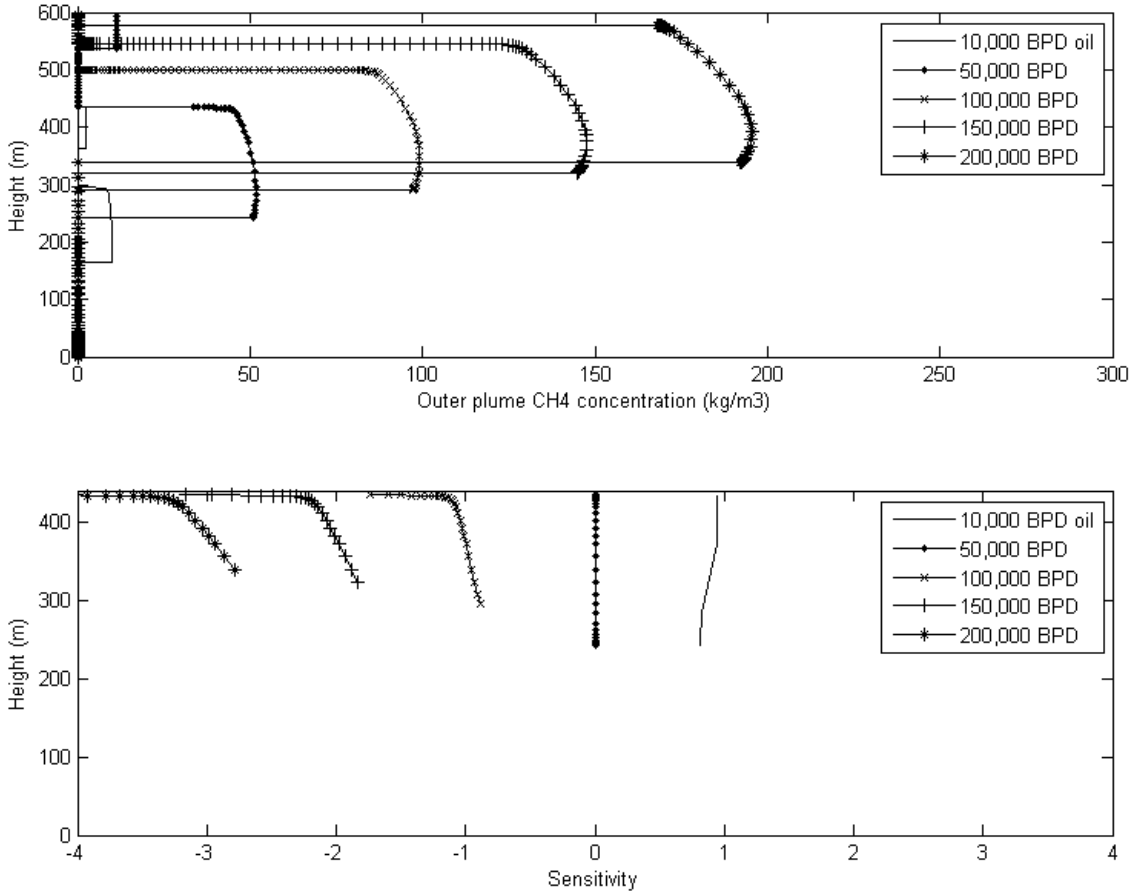

Figure A.44: Top: Raw data for outer plume CH4 concentration at a series of flow rates. Bottom: Sensitivity analysis of the CH4 at the same flow rates. 50,000 BPD is used as the reference.

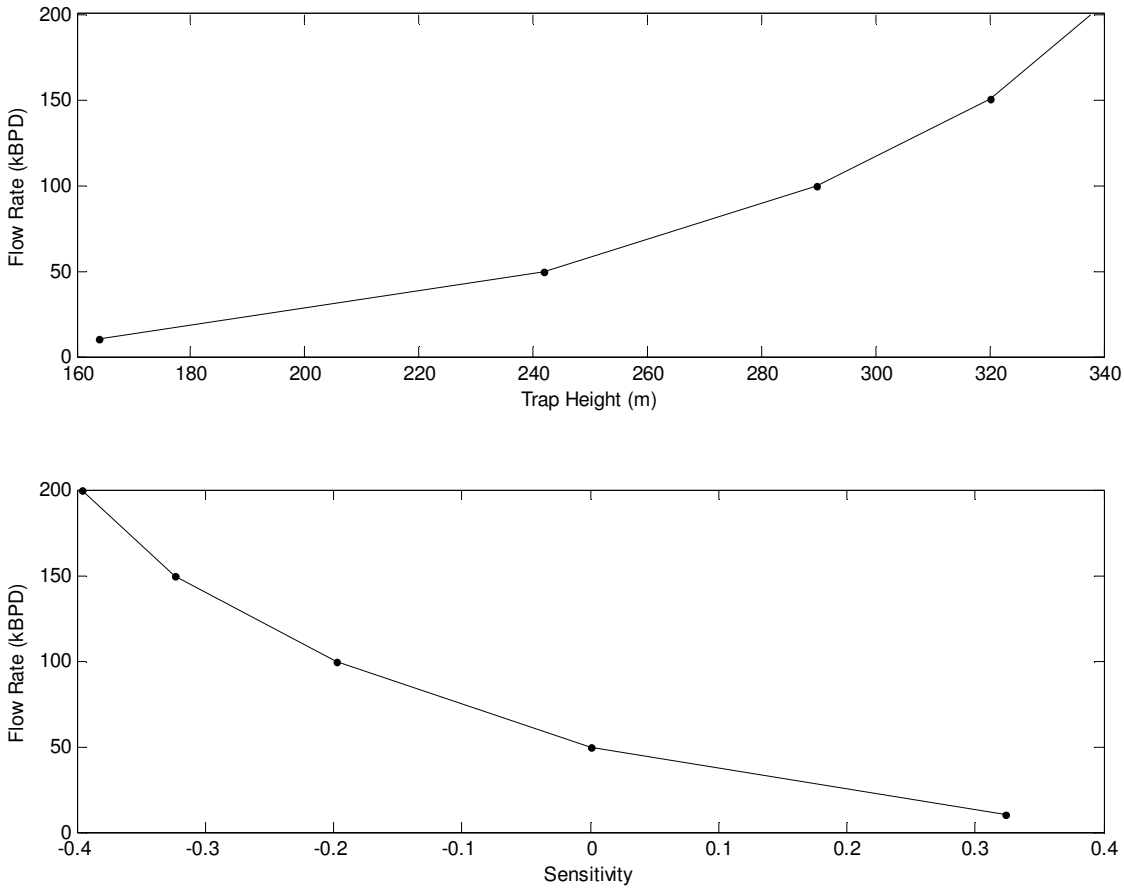

Figure A.45: Top: Trap height for the outer plume with respect to flow rate. Bottom: Sensitivity in relation to flow rate with 50,000 BPD used as the reference value.

A.3 Nomenclature

A_M	Area of model source
A_P	Area of real source
b	Plume radius
$\hat{B}_b$	Buoyancy force of the bubbles
$\hat{B}_i$	Buoyancy force of the inner plume
$\hat{B}_o$	Buoyancy force of the outer plume
B	Kinematic buoyancy flux
B	Non-dimensional plume width
b_i	Inner plume width
B_i	Buoyancy of the inner plume
b_o	Outer plume width
c_a	Concentration in the ambient
C_b	Void fraction occupied by bubbles
c_i	Inner plume concentration
C_i	Inner plume concentration flux
c_o	Inner plume concentration
C_o	Inner plume concentration flux
c_p	Heat capacity
C_S	Saturation concentration

d	Diameter of source
d_b	Effective bubble diameter
E_a	Volume transfer from the ambient to the outer plume
E_i	Volume flux into the inner plume from the outer plume if present or from the ambient fluid
E_o	Volume flux from the inner plume to the outer plume
E_p	Volume flux peeling from the inner plume into the outer plume
F_0	Buoyancy flux
Fr	Froude number
g	Acceleration due to gravity
g_M	Gravity in model
g_P	Gravity in prototype
H	Water depth
J_i	Inner plume heat flux
J_o	Outer plume heat flux
K	Mass transfer coefficient
L	Characteristic length
l_c	Characteristic length for trap height
L_M	Length in model
L_P	Length in the prototype
M	Relative importance of the volume flow of gas and the total water depth
M_g	Molar mass of gas

M_H Velocity ratio

M_i Momentum flux of the inner plume

M_o Momentum flux of the outer plume

N Buoyancy frequency

N_1 Value to be compared to base case in sensitivity analysis

N_b Number of bubbles

N_B Base case in sensitivity analysis

P_g Pressure of gas

P_N Plume number

Q_0 Volume flux at the source

Q_g Gase flow rate at the source

Q_i Flow rate in the inner plume

Q_l Liquid volume flow rate at the source

Q_M Flow rate for model

Q_o Flow rate in the outer plume

Q_P Flow rate for prototype

Q_S Volume flux at the surface

R_g Universal gas constant

s_a Salinity in the ambient

s_i Inner plume salinity

S_i Inner plume salinity flux

s_o Outer plume salinity

S_o Outer plume salinity flux

T_a Ambient temperature

T_g Temperature of gas

T_i Inner plume temperature

T_o Inner plume temperature

T_p Plume temperature

u Centerline velocity

U Non-dimensional plume velocity

u_0 Vertical velocity at source

u_B Bubble velocity

u_c Characteristic velocity scale

u_i Inner plume average velocity

U_M Model velocity

U_N Ratio of slip velocity and characteristic fluid velocity

u_o Outer plume average velocity

U_P Prototype velocity

u_s Slip velocity

V Plume radius times centerline velocity, bu

W Plume radius squared times the centerline velocity, b^2u

W_b Droplet mass flux

x	Non-dimensional height above the plume source
z	Distance above source
z_e	Length of zone of flow establishment
α	Entrainment coefficient
α_i	Entrainment coefficient for the inner plume
α_o	Entrainment coefficient for the outer plume
ε	Peeling factor
λ	Ratio of plume width to another parameter
ξ	Milgram amplification factor
ρ	Plume density
ρ_a	Ambient density
ρ_b	Density of dispersed phase
ρ_g	Density of gas
ρ_i	Inner plume density
ρ_l	Density of liquid
ρ_o	Outer plume density
ρ_r	Reference density